The Electrochemistry of

Supported Metal Multilayers:

In-situ Surface X-ray Scattering Studies

Thesis submitted in accordance with the requirements of the University of Liverpool for the degree of Doctor in Philosophy

by

Naomi Katie Sisson

UNIVERSITY OF LIVERPOOL

Department of Physics

April 2014

Abstract

A combination of in-situ surface x-ray scattering (SXS) and cyclic voltammetry (CV) measurements have been performed to develop an increased understanding of supported metal multilayers on single crystal metal substrates. The formation of ordered metal structures and metal oxides are investigated together with the effect of the surface modification on processes such as OH adsorption and hydrogen evolution.

A detailed in-situ study of the structure and behaviour of underpotentially deposited (UPD) monolayer and bilayer of Ag on the Au(111) surface is given both before and after transfer of the electrode to alkaline electrolyte. Analysis of the SXS data shows that while the bilayer is stable upon transfer, the Ag monolayer re-orders to a partial bilayer. Sulphate anions in the UPD electrolyte stabilise the monolayer as it is formed, however upon transfer to the alkaline electrolyte these are replaced by more specifically adsorbed OH^- ions causing the Ag to restructure to the more stable partial bilayer. The Ag modified electrodes show potential response for OH^- adsorption similar to that of Ag single crystals. Detailed modelling of the SXS data at the positive potential limit in alkaline electrolyte shows evidence of an ordered OH^- layer in the electrochemical double layer. Sub-surface OH indicated in the CV is confirmed in the SXS by a roughening of the topmost Ag layer.

The atomic structure and properties of Co thin films electrodeposited onto Au(111) electrode is investigated using STM and SXS. Measurements confirm that the Co initially grows on the surface as a bilayer. Detailed characterisation of the thin film structure was obtained by analysis of the specular CTR. Results show a small outward expansion in the Co film which may be caused by the presence of adsorbed hydrogen on the Co surface. Changes induced by the presence of CO were investigated and it was found that CO has a dramatic effect on the magnetisation but only cause very small changes in the atomic structure of the Co

film. The measurements indicate the changes in magnetic behaviour are driven by subtle changes in the electrolyte double layer region adjacent to the Co surface.

Thin films of Co were deposited on a Au(111) electrode prior to transfer of the electrode to alkaline electrolyte. Ex-situ AFM imaging revealed that the Co is present on the Au(111) surface in the form of large islands which cover approximately 2.2% of the surface and are located at step edges. Their presence gives rise to a modified reconstruction of the topmost Au layer which was also investigated. Resonant SXS measurements revealed that Co is present both in its metallic state and charged state, most likely in the form $Co(OH)_2$. The Co-modified Au(111) surface shifts the potential for hydrogen evolution positively by ~ 0.1 V compared with that of clean gold.

Acknowledgements

First and foremost I would like to thank my supervisor, Prof. Chris Lucas, for all his support, advice and enthusiasm throughout my PhD and especially for his attitude of always being happy to discuss science! I would like to thank the research group, Alex Brownrigg, Mike Darlington, David Hesp, Gary Harlow and Elizabeth Cocklin, for all their help with the experiments and entertainment during long night shifts. Many thanks go to Dr. Yvonne Grunder for teaching me so much about chemistry and surface science.

Thanks must also go to thank Prof. Richard Nichols and his Chemistry Group, especially Sam and Sarah for all their electrochemistry advice and silliness over the years. I would also like to thank Marion Leibl for keeping me sane in the office and always being happy to have a chat.

I would like to thank all the beamline scientists involved in the experiments, but a special thank you goes to Paul Thompson for all his help in setting up and running the experiments, for staying up on night shifts with us and for showing me Grenoble's night life.

I would like to thank my friends and family. I would like to thank Dr Liz Barritt without whom I would not have made it through my PhD and Miffy Borland for always having time for a chat and continually inspiring me to do more. A special thank you goes to my mum and Chloe for all their love and encouragement. Thank you to my Nana Lan, who always there for a good Sunday Lunch and who is continually supportive and proud of me. Finally, a huge thank you goes to my Husband Daniel for your endless love, support and encouragement.

Table of Contents

List of Figures

List of Acronyms

AFM – Atomic Force Microscopy

Ag/AgCl – Silver / Silver Chloride Electrode

COM – Centre of Mass

CTR – Crystal Truncation Rod

CV – Cyclic Voltammetry

DW – Debye-Waller Factor

FCC – Face Centred Cubic

HCP – Hexagonal Close Packed

HER – Hydrogen Evolution Reaction

IHP – Inner Helmholtz Plane

LEED – Low Energy Electron Diffraction

MBE – Molecular Beam Epitaxy

MCA – Multi Channel Analyzer

ML – Monolayer

MSE – Mercury Sulphate Electrode

MOKE – Magneto Optical Kerr Effect

NEXAFS – Near Edge X-ray Absorption Fine Structure

OHP – Outer Helmholtz Plane

ORR – Oxygen Reduction Reaction

PMA – Perpendicular Magnetization Anisotropy

PZC – Potential of Zero Charge

RHE – Reversible Hydrogen Electrode

SCE – Saturated Calomel Electrode

SRT – Spin Reorientation Transition

STM – Scanning Tunnelling Microscopy

SXS – Surface X-ray Scattering

UHV – Ultra High Vacuum

UPD – Underpotential Deposition

XPS – X-ray Photoelectron Spectroscopy

XRV – X-ray Voltammetry

Chapter 1:

Introduction

An atomic-level understanding of the surface structure and reactivity of catalysts is of paramount importance to the development of innovative materials for a number of energy related technological applications. Key to this is experimental research into the processes occurring at the electrochemical interface. The study of the electrochemical interface and charge transfer across it is of importance to clean energy production and storage [1-3], corrosion [4] and the functioning of biological membranes [5]. The development of fundamental knowledge of the processes occurring at the surface can also be constructive in the targeted development of better systems [3, 6]. Tailoring of the interface structure, for example by adsorption of reactive and spectator species, surface reordering or deposition of metal multilayers, can enhance the reactivity and stability of a catalyst [6, 7]. At the 13th International Conference on Electrified Interfaces, N. Markovic pointed out that unfortunately there is often a trade off between stability and activity; however this knowledge may open up new avenues for the development of ideal catalysts.

Supported metal multilayers provide ideal systems for tailoring the electrocatalytic activity of electrodes [8]. Reactions such as the hydrogen evolution reaction (HER):

$$2H_2O+2e^-\leftrightarrow H_2+2OH^-$$

and oxygen reduction reaction (ORR):

$$\frac{1}{2}O_2 + 2H^+ + 2e^- \rightarrow H_2O$$

involve reaction intermediates, such as OH and OOH, via several stages. The electrocatalyst needs to activate the reaction intermediates, after which the intermediates should be able to diffuse along the surface, react with other intermediates and then the reaction products need to be able to desorb from the surface. These processes lead to conflicting requirements of the surface properties. If the chemical bond is too weak then the catalyst is ineffective but if it is too strong the intermediates do not leave the surface and poison active sites. This is known as the Sabatier principle from which Sabatier type volcano-shaped plots have been developed to represent the 'best catalysts' for a particular reaction [8, 9]. Two examples of such plots are show in Figure 1.1 [10] and Figure 1.2 [11] for the HER and ORR respectively. These show that Pt is the best elemental cathode material for both reactions, however better catalysts have been developed by tailoring the surface properties via the formation bimetallic catalysts. An example of this is Pt3Ni(111) which is 10 fold more active for the ORR than the Pt(111) surface [1, 2]. Another is bimetallic Ag-Au(111) systems, which have recently been found to enhance the reactivity for the electrochemical reduction of nitrate [12] and the catalytic reduction of 4-nitrophenol by $NaBH_4$ (sodium borohydride) in water [13]. The concept that bimetallic surfaces such as supported metal multilayers can enhance surface properties, such as electrochemical reactivity, provides the motivation for the work contained within this thesis. Electrochemical deposition is an ideal method for forming such structures, as it allows well defines surfaces to be produced with atomic precision. The experiments contained within this thesis use

electrochemical methods to deposit monolayer(s) of Ag and Co onto the Au(111) electrode surface, prior to studying the structural and chemical properties of the new supported metal multilayers.

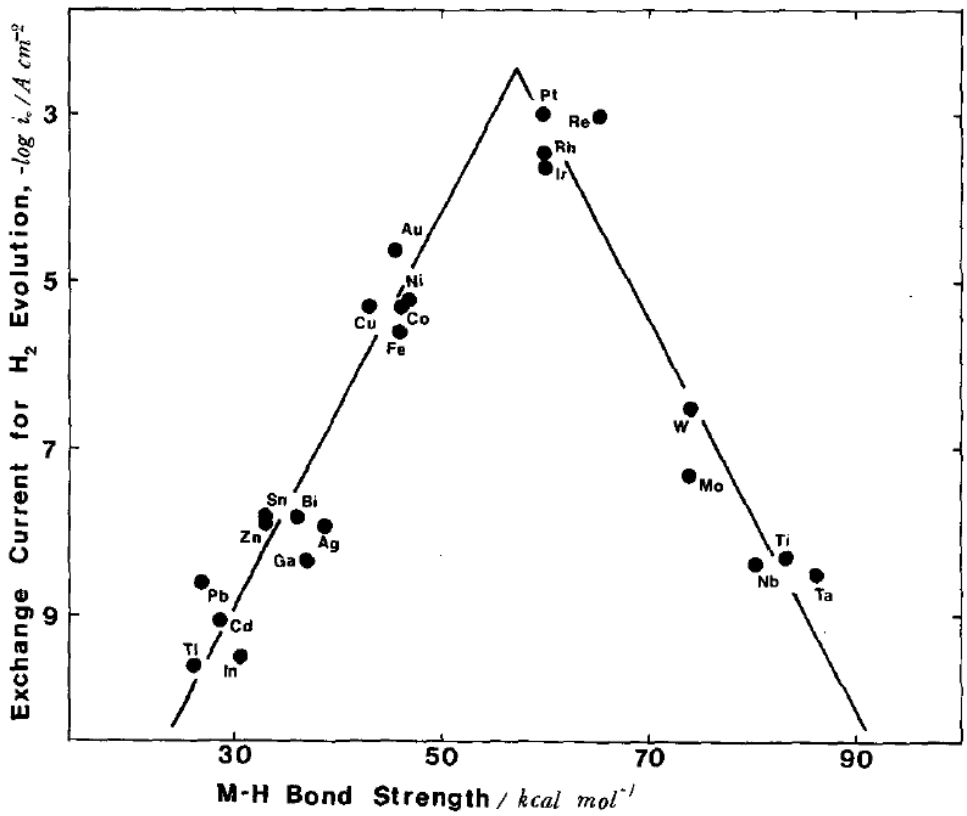

Figure 1.1 Exchange currents for electrolytic hydrogen evolution vs strength of intermediate metal-hydrogen bond formed during electrochemical reaction itself. Reprinted from Journal of Electroanalytical Chemistry, 39, Trasatti S., Work function, electronegativity, and electrochemical behaviour of metals: III. Electrolytic hydrogen evolution in acid solutions, 163-184, Copyright (1972), with permission from Elsevier. [10]

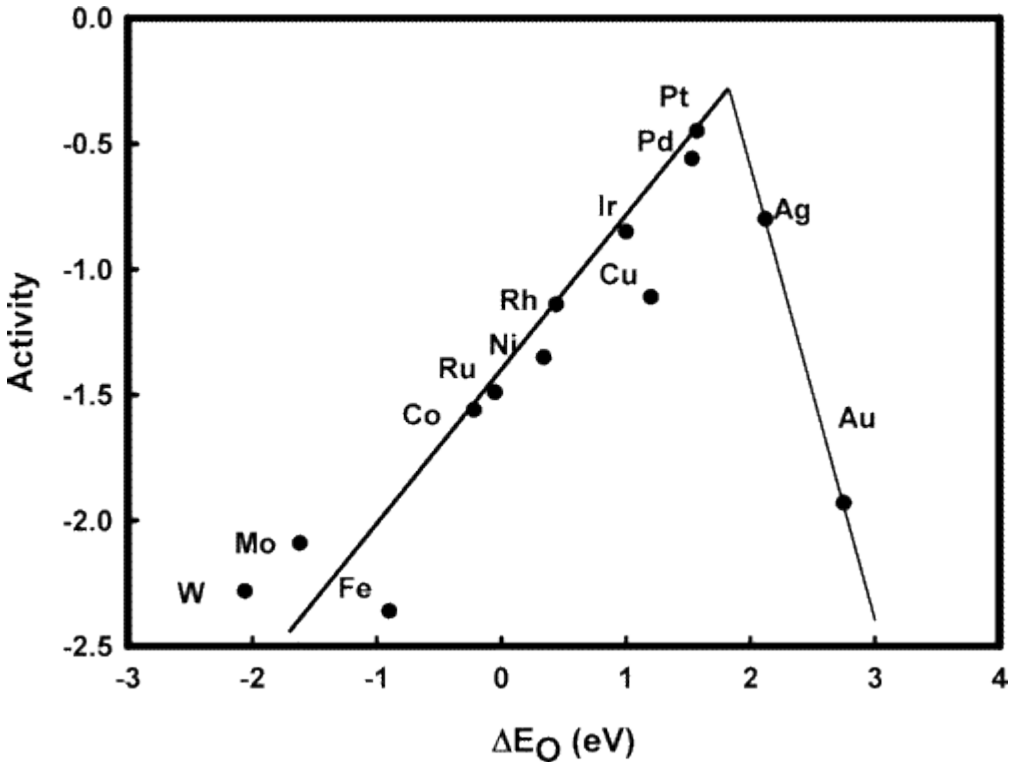

Figure 1.2 Trends in oxygen reduction activity plotted as a function of the oxygen binding energy. Reprinted with permission from The Journal of Physical Chemistry B, 108, Nørskov, J. N. et al., 17886-17892, Origin of the Overpotential for Oxygen Reduction at a Fuel-Cell Cathode. Copyright (2004) American Chemical Society. [11]

The formation, stability and reactivity of surface oxides is also of fundamental importance in both electrochemical and gaseous environments as it is the oxide surface that plays the key role in many catalytic applications. For example Subbaraman *et al.* recently studied the development of bifunctional catalysts for the electrochemical reduction of water, by combining metals which are effective catalysts for the hydrogen evolution reaction, such as Pt, with metal oxides which are effective for water dissociation, in this case $Ni(OH)_2$, they improved the kinetics for the electrochemical reduction of water [6]. The Ag surface oxide is of interest due to the role that the oxide plays in the catalytic gas-phase reactions of ethylene epoxidation and methanol oxidation [14]. Co is reactive in terms of surface oxidation processes, however its magnetic properties provided the motivation for the work in Chapter 6, as monolayer(s) of Co on Au(111) poses perpendicular

magnetization anisotropy (PMA), a phenomenon of strong interest for high density data storage [15].

In recent decades the field of surface science has emerged which utilises UHV environments to study gas-solid interfaces, with techniques such as low energy electron diffraction (LEED), x-ray photoelectron spectroscopy (XPS) and scanning tunnelling microscopy (STM). Electrochemically prepared samples have been transferred from the liquid environment into UHV to examine the surface properties following electrochemical measurements. This, however, is not ideal as there is concern regarding alterations to the surface due to exposure to atmosphere during transfer. The development of in-situ surface science techniques (where the sample is in the electrochemical environment) has enabled research into these systems under realistic conditions. In-situ techniques such as surface x-ray scattering (SXS) and scanning tunnelling microscopy (STM) may be used alongside traditional electrochemistry techniques such as cyclic voltammetry (CV) [12]. From these techniques information regarding structure at surfaces and buried interfaces, elemental composition, electrochemical reactions and the effect of these on the surface ordering can be obtained. Advances in these and other in-situ techniques have enabled structural characterisation of the electrolyte side of the interface [16-18] and even of the liquid/liquid interface [19]. The use of surface x-ray scattering as an in-situ technique is well established, the first synchrotron experiment having taken place in 1988 [20]. SXS is a versatile technique, ideal for probing the surface atomic structure under electrochemical conditions and can be used to obtain a wide range of information, including:

- Characterisation of structures – lattice strain, orientation and surface relaxation.
- Potential dependant studies of the lattice relaxation, for example during the adsorption of atomic hydrogen and the adsorption/oxidation of carbon monoxide.

- Changes to the reconstruction, for example caused by the presence adlayers
- Adsorption of hydroxyl adlayers.
- Structure and kinetics of surface oxide formation and reduction.
- Spectroscopic structural information via resonant SXS
- Kinetic of surface reactions and restructuring

The main aim of the research contained within this thesis is to develop the capabilities for forming supported metal multilayers on single crystal metal substrates by electrochemical methods and the *in-situ* study of these structures in the electrochemical environment using surface x-ray scattering (SXS). The experiments contained within this thesis concern the formation of metal multilayers on single crystal substrates and their behaviour in alkaline and acidic electrolytes. The formation of ordered metal structures and metal oxides are investigated together with the effect of the surface modification on processes such as OH adsorption and hydrogen evolution.

Chapter 2 describes the theoretical principles behind the work contained within this thesis. The theory of x-ray diffraction is briefly introduced building from the case of elastic scattering from an individual electron through to the diffraction from a large 3D crystal. The scattered intensity due to the surface, the crystal truncation rods (CTR's), is described together with the changes to this by the presence of commensurate and incommensurate structures at the surface. The devised model for the solid-liquid interface termed the "electrochemical double layer" is described together with a short introduction to the technique of cyclic voltammetry (CV). Finally details of the technique of x-ray voltammetry (XRV) which combines (SXS) and (CV) are given.

Chapter 3 contains details of the experimental considerations required for an in-situ SXS experiment. The sample preparation, electrochemical cells and experimental setup are described. A description of the data acquisition procedure

together with some discussion of the necessary correction factors and fitting procedures is given. The thin-layer electrochemical cell described in Section 3.3.2 of this chapter was redesigned by the author of this thesis in order to improve its electrochemical cleanliness, speed of assembly and stability over the course of an experiment.

Chapter 4 outlines current knowledge regarding the Au(111) single crystal surface, as the Au(111) surface is used as the substrate for the experiments contained within chapters 5, 6 and 7. The nature of the Au(111) reconstruction in both UHV and electrochemical environments is described. The CV of Au(111) in 0.1 M KOH is briefly discussed together with in situ SXS measurements made at on beamline BM28 (XMaS), the UK-CRG beamline at the ESRF, Grenoble. This chapter provides a useful experimental background for the following studies on supported metal multilayers.

Chapter 5 presents an in-situ study of the structure and behaviour of underpotentially deposited (UPD) Ag layers on Au(111) following transfer of the crystal to 0.1 M KOH. UPD of Ag from 0.05 M H_2SO_4 + 1 mM Ag_2SO_4 electrolyte has been used to form a monolayer and bilayer of Ag on Au(111) and the Ag modified electrode studied in 0.1 M KOH over the potential range 0 V to -1 V. Analysis of the SXS data shows that while the bilayer is stable upon transfer to the silver free alkaline electrolyte, the Ag monolayer re-orders to a partial bilayer. Sulphate anions in the UPD electrolyte stabilise the monolayer as it is formed, however upon transfer to the alkaline electrolyte these are replaced by more specifically adsorbed OH^- ions causing the Ag to restructure to the more stable partial bilayer. The Ag modified electrodes show potential response for OH^- adsorption similar to that of Ag single crystals. Detailed modelling of the SXS data at the positive potential limit in alkaline electrolyte shows evidence of an ordered OH^- layer in the electrochemical double layer. Sub-surface OH indicated in the CV is confirmed in the SXS by a roughening of the topmost Ag layer. SXS experiments were performed at beamline I07, at Diamond Light Source and beamline ID32, at the ESRF. The

author of this thesis took a lead role in performing the SXS and CV experiments and analysis contained within this Chapter and a first author paper based on the Chapter is in progress.

Chapter 6 probes the atomic structure and properties of Co thin films electrodeposited onto Au(111) electrode. STM and SXS measurement confirm that the first layer of Co grows on the surface as a bilayer; i.e. a 2 ML (monolayer) thick. The in-plane strain of the film was found to vary as a function of film thickness. Detailed characterisation of the thin film structure was obtained by analysis of the specular CTR. Results show a small outward expansion in the Co film which may be caused by the presence of adsorbed hydrogen on the Co surface. Changes induced by the presence of CO (carbon monoxide) were also investigated. The CO has a dramatic effect on the magnetisation but only cause very small changes in the atomic structure of the Co film. The measurements indicate the changes in magnetic behaviour are driven by subtle changes in the electrolyte double layer region adjacent to the Co surface. SXS experiments were performed at on beamline BM28 (XMaS), the UK-CRG beamline at the ESRF, Grenoble and beamline ID32, at the ESRF. The work contained within this thesis was done in collaboration with Dr. Philippe Allongue and Dr. Fouad Maroun, from the Laboratoire de Physique de la Matière Condensée, Ecole Polytechnique, Paris, France, who produced the CV, STM and magnetic curve measurements contained within this chapter. A first author paper based on this Chapter is in progress.

Chapter 7 studies the bifunctional electrode created by transferring the Co-modified Au(111) crystal in to alkaline electrolyte. Thin films of Co were deposited on a Au(111) electrode, using a method similar to that in chapter 6, prior to transfer of the electrode to 0.1 M KOH. Ex-situ AFM imaging revealed that the Co is present on the Au(111) surface in the form of large islands which cover approximately 2.2% of the surface and are located at step edges. Their presence gives rise to a modified reconstruction of the topmost Au layer which was also investigated. Resonant SXS measurements revealed that Co is present both in its

metallic state and charged state, most likely in the form $Co(OH)_2$. The Co-modified Au(111) surface shifts the potential for hydrogen evolution positively by ~ 0.1 V compared with that of clean gold. SXS experiments were performed at on beamline BM28 (XMaS), the UK-CRG beamline at the ESRF, Grenoble and at beamline I07, at Diamond Light Source. STM images and subsequent analysis was performed by Elizabeth Cocklin, PhD student at the University of Liverpool. Dr. Philippe Allongue and Dr. Fouad Maroun, from the Laboratoire de Physique de la Matière Condensée, Ecole Polytechnique, Paris, France, also contributed ideas regarding the Co deposition techniques. The author of this thesis took a lead role in performing the SXS and CV experiments and analysis contained within this Chapter.

Chapter 8 summarises the results from the experimental chapters. Finally it provides suggestions for how these results could be developed and suggests opportunities for future research.

References

[1] V.R. Stamenkovic, B.S. Mun, M. Arenz, K.J.J. Mayrhofer, C.A. Lucas, G.F. Wang, P.N. Ross, N.M. Markovic, Nat Mater, 6 (2007) 241-247.
[2] V.R. Stamenkovic, B. Fowler, B.S. Mun, G.F. Wang, P.N. Ross, C.A. Lucas, N.M. Markovic, Science, 315 (2007) 493-497.
[3] R. Subbaraman, D. Tripkovic, K.C. Chang, D. Strmcnik, A.P. Paulikas, P. Hirunsit, M. Chan, J. Greeley, V. Stamenkovic, N.M. Markovic, Nat Mater, 11 (2012) 550-557.
[4] F.U. Renner, A. Stierle, H. Dosch, D.M. Kolb, T.L. Lee, J. Zegenhagen, Nature, 439 (2006) 707-710.
[5] J.T. Hynes, Nature, 446 (2007) 270-273.
[6] R. Subbaraman, D. Tripkovic, D. Strmcnik, K.C. Chang, M. Uchimura, A.P. Paulikas, V. Stamenkovic, N.M. Markovic, Science, 334 (2011) 1256-1260.
[7] W.C. Sheng, M. Myint, J.G.G. Chen, Y.S. Yan, Energ Environ Sci, 6 (2013) 1509-1512.
[8] F. Calle-Vallejo, M.T.M. Koper, A.S. Bandarenka, Chem Soc Rev, 42 (2013) 5210-5230.
[9] A.S. Bandarenka, M.T.M. Koper, J Catal, 308 (2013) 11-24.
[10] S. Trasatti, J Electroanal Chem, 39 (1972) 163-&.
[11] J.K. Norskov, J. Rossmeisl, A. Logadottir, L. Lindqvist, J.R. Kitchin, T. Bligaard, H. Jonsson, J Phys Chem B, 108 (2004) 17886-17892.
[12] F. Calle-Vallejo, M.H. Huang, J.B. Henry, M.T.M. Koper, A.S. Bandarenka, Phys Chem Chem Phys, 15 (2013) 3196-3202.
[13] H.L. Jiang, T. Akita, T. Ishida, M. Haruta, Q. Xu, J Am Chem Soc, 133 (2011) 1304-1306.
[14] C.I. Carlisle, D.A. King, M.L. Bocquet, J. Cerda, P. Sautet, Phys Rev Lett, 84 (2000) 3899-3902.
[15] P. Allongue, F. Maroun, H.F. Jurca, N. Tournerie, G. Savidand, R. Cortes, Surf Sci, 603 (2009) 1831-1840.
[16] C.A. Lucas, P. Thompson, Y. Grunder, N.M. Markovic, Electrochem Commun, 13 (2011) 1205-1208.
[17] M. Nakamura, N. Sato, N. Hoshi, O. Sakata, Chemphyschem, 12 (2011) 1430-1434.
[18] M.F. Toney, J.N. Howard, J. Richer, G.L. Borges, J.G. Gordon, O.R. Melroy, D.G. Wiesler, D. Yee, L.B. Sorensen, Surf Sci, 335 (1995) 326-332.
[19] Y. Grunder, J.F.W. Mosselmans, S.L.M. Schroeder, R.A.W. Dryfe, J Phys Chem C, 117 (2013) 5765-5773.
[20] M.G. Samant, M.F. Toney, G.L. Borges, L. Blum, O.R. Melroy, J Phys Chem-Us, 92 (1988) 220-225.

Chapter 2:

Theoretical Principles

2.1 Introduction

The experiments detailed within this thesis probe the relationships between the electrochemical reactions and structural changes occurring at the electrode/electrolyte interface. Since the mid-19th century models have been developed to describe the solid-liquid interface and electrochemical techniques such as cyclic voltammetry (CV) have been used to investigate the processes occurring. However CV measures the charge transfer across the interface and therefore does not give direct information about the chemical or structural changes. The development of in-situ techniques such as surface x-ray scattering (SXS) and scanning tunnelling microscopy (STM) have enabled the study of structural changes during electrochemical reactions such as anion adsorption, metal deposition and electrocatalysis. In this chapter the general theory of x-ray diffraction from a crystal is described, following which specific details of surface x-ray scattering is discussed together with the effects on this of commensurate and

incommensurate layers. The currently accepted model of the electrode/electrolyte interface will be described together with the basic principles of CV. Finally, the technique of x-ray voltammetry will be explained, which combines the both SXS and CV in order to perform potentiodynamic x-ray diffraction experiments.

2.2 Crystallographic Definitions

A crystal is defined as a periodic array of atoms with long range order and can be fully described by a space lattice together with a group of atoms called a basis attached to each lattice point. The space lattice is defined by three lattice vectors **a**, **b** and **c** such that any integer multiple of the vectors from any point on the lattice will locate a similar lattice point. The unit cell is the parallelepiped defined by the lattice vectors **a**, **b** and **c** with angles α, β and γ between them. The face-centered cubic (fcc) lattice is the crystal structure of many of the transition metals including Au, Ag, Pt, Ni, Pd and Cu and so is particularly relevant to this thesis. The fcc lattice shown in Figure 2.1 is a cubic lattice where the vectors **a**, **b** and **c** are all equal and the angles between them α, β and γ equal 90°. The basis consists of four atoms located at (0,0,0), (1/2,0,1/2), (0,1/2,1/2) and (1/2,1/2,0) in terms of the lattice vectors (**a**,**b**,**c**) [1, 2].

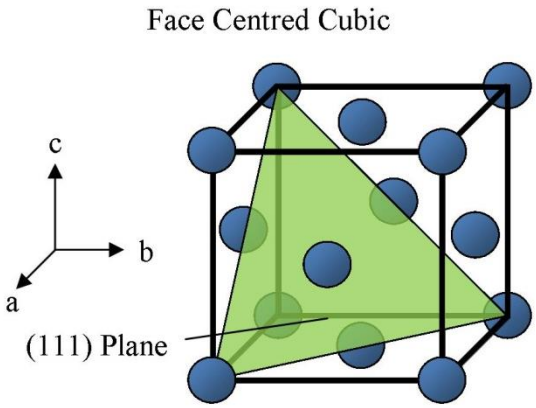

Figure 2.1 A schematic representation of the face centred cubic (fcc) crystal structure with the low index plane fcc(111) indicated in green. For fcc crystals **a** = **b** = **c** and the angle between them α = β = γ = 90°.

There is an infinite number of 2D planes associated with a 3D lattice which are defined by the Miller indices (hkl). Each set of parallel planes have a specific arrangement and density of atoms within the plane, and interplanar spacing. The miller indices are derived by finding the intercepts of the plane with the 3 axis in terms of the lattice vectors **a**, **b** and **c**, then taking the reciprocals of these intercepts and multiplying by the lowest common factor. The directions in cubic crystals are denoted [hkl] and are perpendicular to the corresponding plane (hkl). The three low index planes for an fcc lattice are (100), (110) and (111) the latter being shown schematically in Figure 2.1. The interplanar lattice spacing d_{hkl} for parallel planes can be calculated from the miller indices as follows:

$$d_{hkl} = \frac{a_0}{\sqrt{h^2 + k^2 + l^2}} \qquad (2.1)$$

where a_0 is the lattice constant.

2.3 X-ray Diffraction Theory

2.3.1 X-ray Interactions with Matter

When an x-ray photon is incident on an atom it may interact with it in two ways: (1) the photon may be scattered or (2) the photon may be adsorbed. For the scattering process we consider the classical description in which the electric field of the incident x-ray photon exerts a force on an electron of the atom, which then oscillates and radiates the scattered wave in all directions. Classically this interaction is elastic, the scattered wave having the same energy as the incident one. In the quantum mechanical description it is possible for inelastic scattering to occur, a process known as the Compton effect. However this scattering (from different electrons) is in its nature incoherent, due to the change in wavelength, and hence produces only a diffuse background. It is the elastic scattering of x-rays that is exploited for x-ray diffraction.

2.3.2 Kinematical Diffraction

In the kinematical approximation the amplitude scattered by a crystal is taken to be the sum of independent contributions from all the individual electrons. To calculate the x-ray scattering from a crystal we start by considering the scattering from a single electron. From this, using the kinematic approximation, we can simply sum the scattering from all the electrons associated with an atom, then from the atoms in one unit cell of the crystal and finally a crystal containing N unit cells to fully describe the scattering from the entire crystal. Figure 2.2 defines the real-space vectors which are used in the derivation of the scattered intensity. The derivations given in Chapter 2.3 closely follow the comprehensive treatment provided in references [2-6].

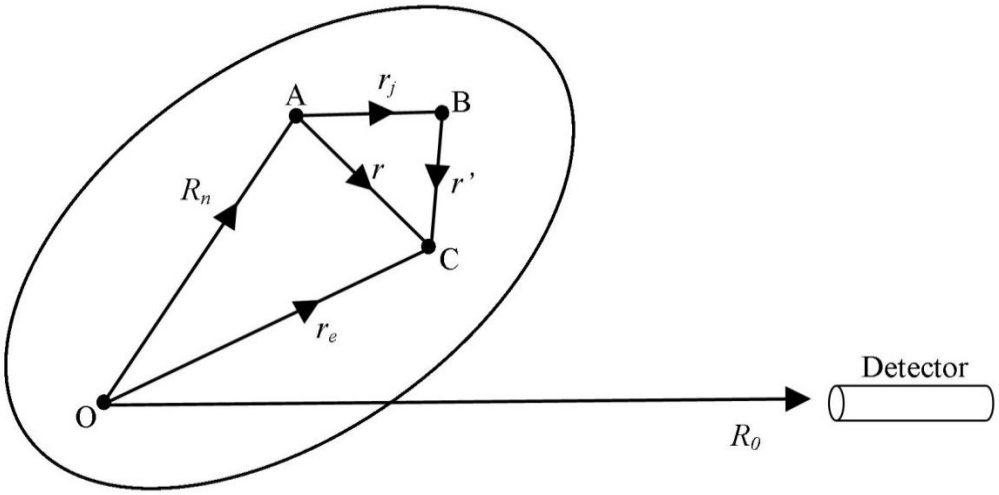

Figure 2.2 Real-space vectors defining the position of an electron (C) belonging to the jth atom (B) of the nth unit cell (A) with respect to the origin of the crystal (O). The origin of the nth unit cell is a distance R_n from the origin of the crystal and the scattering is observed at a distance of R_0.

2.3.3 Momentum Transfer

In an elastic scattering event momentum can be transferred and for scattering experiments the momentum transfer, $\boldsymbol{q}$, is the experimental variable. It is useful to define the momentum transfer as, $\boldsymbol{q} = \boldsymbol{k_f} - \boldsymbol{k_i}$, which is the difference between the incident wave-vector, $\boldsymbol{k_i}$, and scattered wave-vector, $\boldsymbol{k_f}$, as shown in Figure 2.3.

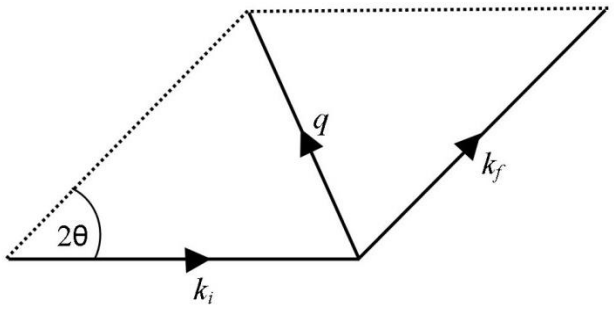

Figure 2.3 Momentum transfer, q, illustrated in terms of the reciprocal space incident and scattered wave-vectors, k_i and k_f.

For elastic scattering $|\boldsymbol{k_i}| = |\boldsymbol{k_f}| = |\boldsymbol{k}| = \frac{2\pi}{\lambda}$ where λ is the x-ray wavelength. Using this relationship, and some simple trigonometry, Bragg's law can be expressed in terms of the momentum transfer and reciprocal space wave-vector:

$$|\boldsymbol{q}| = 2|\boldsymbol{k}| \sin\left(\frac{2\theta}{2}\right) = \frac{4\pi}{\lambda} \sin\left(\frac{2\theta}{2}\right) \qquad (2.2)$$

2.3.4 Scattering from a Single Electron

To derive the scattering from a crystal lattice, first we start with a single electron and build to a complete crystal. The incident photon has an associated electric field, which exerts a force on the electron setting it into oscillation. The electron subsequently radiates a spherical wave with identical wavelength to the incident photon. The real and reciprocal space vectors defined in Figure 2.2 and Figure 2.3 are used in deriving the Thompson formula, which describes the amplitude of a scattered wave A_e from an electron at $\boldsymbol{r_e}$ as a function of the incident wave amplitude A_i:

$$A_e e^{(-\mathrm{i}\,\boldsymbol{k_f}\cdot\boldsymbol{r_e})} = A_i \frac{e^2}{mc^2} \frac{1}{R_0} e^{(-\mathrm{i}\,\boldsymbol{k_i}\cdot\boldsymbol{r_e})} \qquad (2.3)$$

where e and m are the electrons charge and mass and R_0 is the distance to the observer. The $1/R_0$ factor arises due to the spherical nature of the radiation emitted by an oscillating electron.

Using the previous definition of the momentum transfer, $\boldsymbol{q} = \boldsymbol{k_f} - \boldsymbol{k_i}$, the Thompson formula can be rearranged to:

$$A_e = A_i \frac{e^2}{mc^2} \frac{1}{R_0} e^{\mathrm{i}(\boldsymbol{q}\cdot\boldsymbol{r_e})} \qquad (2.4)$$

It is worth noting at this point that the incident wave is polarised in the horizontal plane and hence, depending on the geometry of the scattering plane, corrections to the observed intensity may need to be applied.

2.3.5 Scattering from an Atom

The scattering amplitude from an atom, A_a, is the summation of the scattering amplitudes from each electron contained within the atom. Since classically the electron has a density distribution, $\rho(r')$, where r' is the position of the electron with respect to the atom as shown in Figure 2.2, the summation becomes an integration:

$$A_a = A_i \frac{e^2}{mc^2} \frac{1}{R_0} \int_{-\infty}^{+\infty} \rho(\boldsymbol{r'})\, e^{\mathrm{i}\,\boldsymbol{q}\cdot(\boldsymbol{R_n}+\boldsymbol{r_j}+\boldsymbol{r'})}\, \boldsymbol{d^3 r'} \qquad (2.5)$$

where the electron position vector, r_e, has been substituted by $\left(\boldsymbol{R_n} + \boldsymbol{r_j} + \boldsymbol{r'}\right)$. This can be rewritten as:

$$A_a = A_i \frac{e^2}{mc^2} \frac{1}{R_0} f(\boldsymbol{q}) e^{\mathrm{i}\,\boldsymbol{q}\cdot(\boldsymbol{R_n}+\boldsymbol{r_j})} \qquad (2.6)$$

where $f(\boldsymbol{q})$ is the atomic form factor which is defined as the Fourier transform of the electron density of a single atom.

$$f(\boldsymbol{q}) = \int_{-\infty}^{+\infty} \rho(\boldsymbol{r'})\, e^{\mathrm{i}\,\boldsymbol{q}\cdot\boldsymbol{r'}}\, \boldsymbol{d^3 r'} \qquad (2.7)$$

At $\boldsymbol{q} = 0$ all the electrons scatter in phase so $f(\boldsymbol{q}) = Z$. As $\boldsymbol{q}$ increases the electrons start to scatter out of phase and $f(\boldsymbol{q})$ decreases. Tabulated values for $f(\boldsymbol{q})$ for each element can be found in the International Tables for Crystallography [7].

Modifications to the atomic form factor need to be made if the energy of the incident photons is close to an adsorption edge of the atom. The atomic form factor is modified by the dispersion corrections f' and f'' which are energy dependant. The corrected form factor is then given by:

$$f(\boldsymbol{q}, E) = f(\boldsymbol{q}) + f'(E) + \mathrm{i}\, f''(E) \qquad (2.8)$$

For the experiments reported in this thesis the energy was usually kept away from the adsorption edges of the atoms, so the dispersion corrections are not needed. However this effect can be used to an advantage in Resonance experiments [8, 9] which shall be discussed in more detail in Chapter 7. A full list of electron binding energies (adsorption edges) for elements from Hydrogen to Uranium may be found in the X-ray Data Booklet [10].

2.3.6 Scattering from a Unit Cell

The scattering amplitude from one unit cell, A_u, is the summation of contributions from all the atoms contained within it. The atoms may not necessarily be of the same chemical element, so separate form factors are used for each atom denoted by $f_j(\boldsymbol{q})$. For N_c atoms in the unit cell, the unit cell scattering amplitude is given by:

$$A_u = A_i \frac{e^2}{mc^2} \frac{1}{R_0} \sum_{j=1}^{N_c} f_j(\boldsymbol{q})\, e^{\mathrm{i}\, \boldsymbol{q}\cdot(\boldsymbol{R_n}+\boldsymbol{r_j})}$$

$$= A_i \frac{e^2}{mc^2} \frac{1}{R_0} F(\boldsymbol{q}) e^{\mathrm{i}\, \boldsymbol{q}\cdot\boldsymbol{R_n}} \qquad (2.9)$$

Where $F(\boldsymbol{q})$ is the structure factor:

$$F(\boldsymbol{q}) = \sum_{j=1}^{N_c} f_j(\boldsymbol{q})\, e^{\mathrm{i}\, \boldsymbol{q}\cdot\boldsymbol{r_j}} \qquad (2.10)$$

The structure factor is dependent on both the direction and magnitude of $\boldsymbol{q}$, as the relative positions of the atoms within the unit cell are important. However the atoms are never residing at fixed lattice sites, they are thermally vibrating around an average position. To account for this a Debye-Waller factor, DW, is included in the structure factor as follows:

$$F(\boldsymbol{q}) = \sum_{j=1}^{N_c} f_j(\boldsymbol{q})\, DW\, e^{\mathrm{i}\,\boldsymbol{q}\cdot\boldsymbol{r_j}} \qquad (2.11)$$

The Debye-Waller factor will be fully addressed in Section 2.4.2.

2.3.7 Scattering from a Crystal

The scattering amplitude from the entire crystal, A_c, is the summation of the scattering amplitudes from each unit cell. The crystal is defined as consisting of N_1, N_2, N_3, unit cells along the three crystal axes defined by the vectors, $\boldsymbol{a}$, $\boldsymbol{b}$ and $\boldsymbol{c}$. The position of each unit cell relative to the origin is given by the vector:

$$\boldsymbol{R}_n = n_1\boldsymbol{a} + n_2\boldsymbol{b} + n_3\boldsymbol{c} \qquad (2.12)$$

where n_1, n_2 and n_3 are intergers. The scattering amplitude for the entire crystal is written as:

$$A_c = A_i \frac{e^2}{mc^2}\frac{1}{R_0} F(\boldsymbol{q}) \sum_{n_1=0}^{N_1-1}\sum_{n_2=0}^{N_2-1}\sum_{n_3=0}^{N_3-1} e^{\mathrm{i}\,\boldsymbol{q}\cdot(n_1\boldsymbol{a}+n_2\boldsymbol{b}+n_3\boldsymbol{c})} \qquad (2.13)$$

where the terms of interest are the structure factor, which contains all the chemical information, and the three independent summation terms.

2.3.8 Scattered Intensity from a Crystal

So far we have only considered the scattered amplitude, however experimentally we measure the scattered intensity, $I(\boldsymbol{q})$, so the next step is to take the square modulus of A_c as $I(\boldsymbol{q}) \propto |A_c|^2$. To do this lets first consider one of the summation terms.

$$S_{N_1}(\boldsymbol{q}\cdot\boldsymbol{a}) = \sum_{n_1=0}^{N_1-1} e^{\mathrm{i}\,\boldsymbol{q}\cdot(n_1\boldsymbol{a})} \qquad (2.14)$$

This is a geometrical series and may be written:

$$S_{N_1}(\boldsymbol{q}\cdot\boldsymbol{a}) = \frac{1-e^{\mathrm{i}\,N_1\boldsymbol{q}\cdot\boldsymbol{a}}}{1-e^{\mathrm{i}\,\boldsymbol{q}\cdot\boldsymbol{a}}} \qquad (2.15)$$

which may be rearranged to:

$$S_{N_1}(\boldsymbol{q}\cdot\boldsymbol{a}) = \frac{e^{\mathrm{i}\,N_1\boldsymbol{q}\cdot\boldsymbol{a}/2}\left(e^{-\mathrm{i}\,N_1\boldsymbol{q}\cdot\boldsymbol{a}/2}-e^{\mathrm{i}\,N_1\boldsymbol{q}\cdot\boldsymbol{a}/2}\right)}{e^{\mathrm{i}\,\boldsymbol{q}\cdot\boldsymbol{a}/2}\left(e^{-\mathrm{i}\,\boldsymbol{q}\cdot\boldsymbol{a}/2}-e^{\mathrm{i}\,\boldsymbol{q}\cdot\boldsymbol{a}/2}\right)} \qquad (2.16)$$

To calculate the square modulus of $S_{N_1}(\boldsymbol{q}\cdot\boldsymbol{a})$ we apply Euler's formula, $e^{\mathrm{i}\,\theta} = \cos\theta + \mathrm{i}\sin\theta$, and multiply the equation by its complex conjugate. The pre-factor becomes unity and we are left with:

$$\left|S_{N_1}(\boldsymbol{q}\cdot\boldsymbol{a})\right|^2 = \frac{sin^2(N_1\boldsymbol{q}\cdot\boldsymbol{a}/2)}{sin^2(\boldsymbol{q}\cdot\boldsymbol{a}/2)} \qquad (2.17)$$

The above function, termed the 'N-slit interference function' for its use in optics, rises to a maximum of ${N_1}^2$ when $\boldsymbol{q}\cdot\boldsymbol{a} = 2\pi m$ where m is an integer. For the case of an average crystal, N_1 is very large and the resulting N-slit interference function is essentially zero everywhere except in the immediate vicinity of $\boldsymbol{q}\cdot\boldsymbol{a} = 2\pi m$

where it rises to a very sharp peak. The same treatment can be applied to the other two summation terms.

The scattered intensity, $I(\boldsymbol{q})$, can now be defined as:

$$I(\boldsymbol{q}) = I_i \left(\frac{e^2}{mc^2}\frac{1}{R_0}\right)^2 |F(\boldsymbol{q})|^2 \frac{sin^2(N_1\boldsymbol{q}\cdot\boldsymbol{a}/2)}{sin^2(\boldsymbol{q}\cdot\boldsymbol{a}/2)}\frac{sin^2(N_2\boldsymbol{q}\cdot\boldsymbol{b}/2)}{sin^2(\boldsymbol{q}\cdot\boldsymbol{b}/2)}\frac{sin^2(N_3\boldsymbol{q}\cdot\boldsymbol{c}/2)}{sin^2(\boldsymbol{q}\cdot\boldsymbol{c}/2)} \qquad (2.18)$$

where I_i is the intensity of the incident photon beam. It is now clear that unless the three independent N-slit interference functions are simultaneously close to their maximum values then the scattered intensity will be negligible. This leads to the definition of the Laue conditions for diffraction:

$$\begin{aligned} \boldsymbol{q}\cdot\boldsymbol{a} &= 2\pi h \\ \boldsymbol{q}\cdot\boldsymbol{b} &= 2\pi k \\ \boldsymbol{q}\cdot\boldsymbol{c} &= 2\pi l \end{aligned} \qquad (2.19)$$

in which the Miller indices h, k and l take integer values. For diffraction to take place all three Laue conditions must be satisfied. The three conditions can be simultaneously satisfied by the vector:

$$\boldsymbol{q} = h\boldsymbol{a}^* + k\boldsymbol{b}^* + l\boldsymbol{c}^* \qquad (2.20)$$

where $\boldsymbol{a}^*$, $\boldsymbol{b}^*$ and $\boldsymbol{c}^*$ are related to the real-space vectors by:

$$\boldsymbol{a}^* = 2\pi\frac{\boldsymbol{b}\times\boldsymbol{c}}{\boldsymbol{a}\cdot(\boldsymbol{b}\times\boldsymbol{c})}, \qquad \boldsymbol{b}^* = 2\pi\frac{\boldsymbol{c}\times\boldsymbol{a}}{\boldsymbol{a}\cdot(\boldsymbol{b}\times\boldsymbol{c})} \text{ and } \boldsymbol{c}^* = 2\pi\frac{\boldsymbol{a}\times\boldsymbol{b}}{\boldsymbol{a}\cdot(\boldsymbol{b}\times\boldsymbol{c})} \qquad (2.21)$$

A 3D lattice of points is formed by the sets of integer values h, k and l which give a $\boldsymbol{q}$ that satisfies the Laue conditions. This is known as the *reciprocal lattice* and is

defined by the *reciprocal lattice basis vectors* $\boldsymbol{a}^*$, $\boldsymbol{b}^*$ and $\boldsymbol{c}^*$ which are orthogonal to the *real-space basis vectors*. Since the *real-space basis vectors* have units of length Å, *the reciprocal lattice basis vectors* have units of inverse length $Å^{-1}$.

Now we can define the diffraction pattern from a 3D crystal, in which the diffracted intensity is zero except for discrete values of q that lie on the reciprocal lattice. The intensity measured at such a point is given by:

$$I_{hkl} = I_i \left(\frac{e^2}{mc^2}\frac{1}{R_0}\right)^2 |F(h\boldsymbol{a}^* + k\boldsymbol{b}^* + l\boldsymbol{c}^*)|^2 \, {N_1}^2 {N_2}^2 {N_3}^2 \qquad (2.22)$$

2.4 Surface X-ray Diffraction

2.4.1 Diffraction from a 2D Monolayer and Perfectly Terminated Crystal

So far we have discussed the scattering from a bulk crystal, infinite in all directions. But in this thesis we are interested in what happens at the surface. To start we will consider the two-dimensional case of an isolated monolayer [3-5], where vectors $\boldsymbol{a}$ and $\boldsymbol{b}$ lie in the plane of the surface and $\boldsymbol{c}$ is the vector along the surface normal. Since $N_3 = 1$ the N-slit interference function is independent of $\boldsymbol{q} \cdot \boldsymbol{c}$ and equation (2.18) becomes:

$$I(\boldsymbol{q})_{2D} = I_i \left(\frac{e^2}{mc^2}\frac{1}{R_0}\right)^2 |F(\boldsymbol{q})|^2 \, {N_1}^2 {N_2}^2 \qquad (2.23)$$

In reciprocal space this results in rods of scattering sharp in both directions parallel to the surface but diffuse in the direction normal to the surface. The real and reciprocal space representations of the isolated monolayer are shown in Figure 2.4.

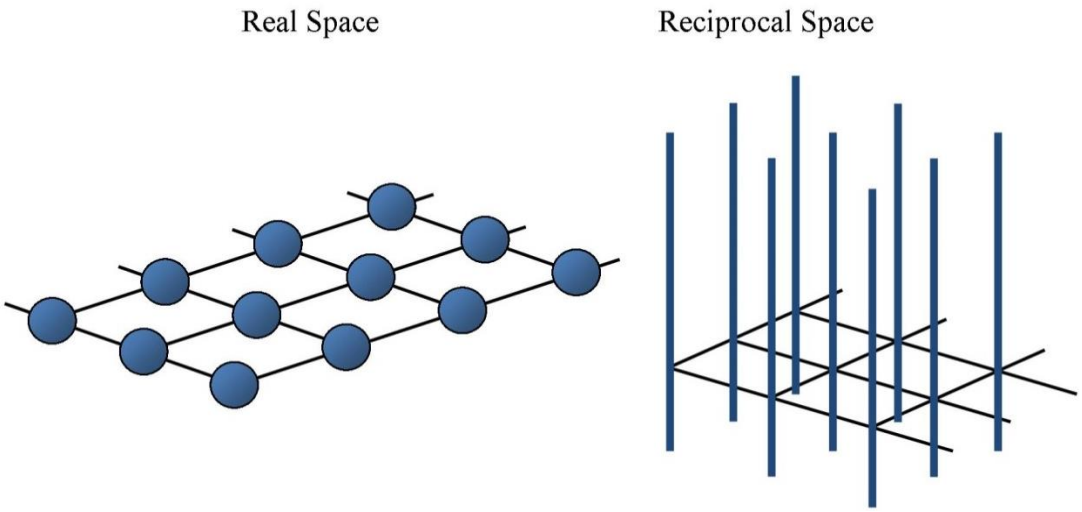

Figure 2.4 Real-space structure and reciprocal space diffraction pattern for an isolated two dimensional monolayer.

For the case of a perfectly terminated crystal surface the diffraction pattern can be thought of as a superposition of the diffraction spots from an infinite 3D crystal and the diffraction rods from the 2D layer which forms the crystal surface, this idea is illustrated in Figure 2.5.

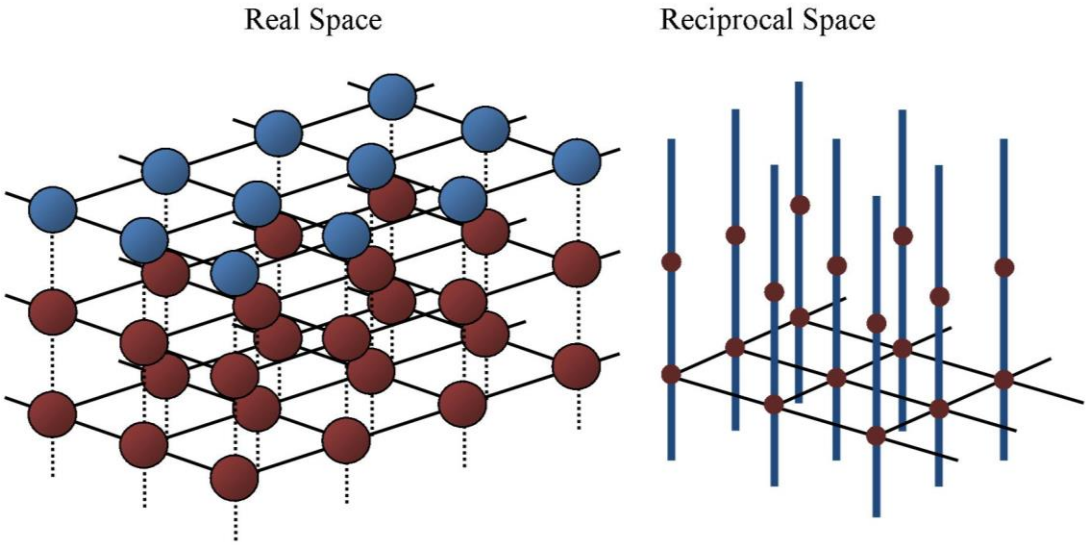

Figure 2.5 Real-space structure and superimposed reciprocal space diffraction patterns for the surface of a three dimensional crystal.

In reality the diffraction rods are not uniform as in the 2D case as the scattering from surface is influenced by all the layers of the crystal. The diffraction actually

looks like Figure 2.6 and are termed crystal truncation rods as they arise from the crystal being terminated or truncated [11].

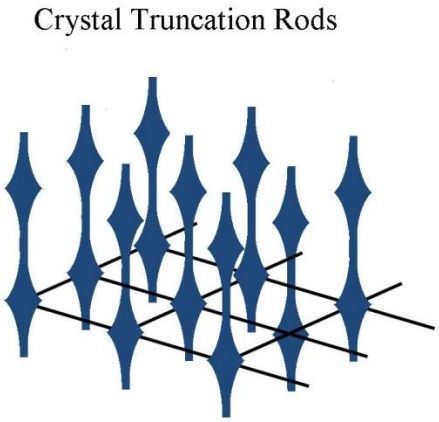

Figure 2.6 Realistic representation of diffraction from the surface of a three dimensional crystal, showing a changing intensity profile along the crystal truncation rods.

To calculate the intensity of scattering of a crystal truncation rod it is first assumed that the Laue conditions $\boldsymbol{q}\cdot\boldsymbol{a}=2\pi h$ and $\boldsymbol{q}\cdot\boldsymbol{b}=2\pi k$ are met so that equation (2.18) becomes:

$$I(\boldsymbol{q})_{CTR}=I_i\left(\frac{e^2}{mc^2}\frac{1}{R_0}\right)^2|F(\boldsymbol{q})|^2\,{N_1}^2{N_2}^2\,\frac{sin^2(N_3\boldsymbol{q}\cdot\boldsymbol{c}/2)}{sin^2(\boldsymbol{q}\cdot\boldsymbol{c}/2)} \qquad (2.24)$$

For the remaining N-slit function in the above equation N_3 is large, therefore $sin^2(N_3\boldsymbol{q}\cdot\boldsymbol{c}/2)$ is a rapidly varying function of $\boldsymbol{q}$ and is taken to be its average value of $1/2$.

$$I(\boldsymbol{q})_{CTR}=I_i\left(\frac{e^2}{mc^2}\frac{1}{R_0}\right)^2|F(\boldsymbol{q})|^2\,{N_1}^2{N_2}^2\,\frac{1}{2\,sin^2(\boldsymbol{q}\cdot\boldsymbol{c}/2)} \qquad (2.25)$$

The above equation breaks down when $\boldsymbol{q}\cdot\boldsymbol{c}=2\pi l$, as it gives an infinite intensity, however it produces sharp peaks in intensity around these values called Bragg peaks and non-zero intensity between them. So far we have assumed the surface is

perfectly terminated and defect free. However real surfaces can have a structure different to the bulk and may be expanded, have a different occupation, have a surface roughness, contained different atoms to the bulk etc. These differences change the profile of the CTR between Bragg peaks and are mainly taken into account by the structure factor. In the final section of the CTR theory we will describe the structure factor for the case of a fcc (111) crystal and then look at the variations which can be found in the CTR profile.

2.4.2 The FCC (111) Reciprocal Lattice and Structure Factor

The Au(111) crystal is used as the substrate for the experiments concerned within this thesis and therefore we will discuss the fcc (111) reciprocal lattice and structure factor [12-14]. The (111) surface is a hexagonally close packed surface structure with ABC stacking in the surface normal direction as shown in Figure 2.7(a). The coordinate system is redefined such that L lies along the surface normal. The vectors $\boldsymbol{a}$ and $\boldsymbol{b}$ lie in the plane of the surface and subtend an angle of $120°$ and vector $\boldsymbol{c}$, which is along the surface normal, consists of three atomic layers due to the ABC stacking. The hexagonal surface unit cell is defined such that $\boldsymbol{a} = \boldsymbol{b} = \frac{a_0}{\sqrt{2}} = a_{NN}$ and $\boldsymbol{c} = a_0\sqrt{3}$ where the Au lattice constant $a_0 = 4.08\text{Å}$ and a_{NN} is the nearest neighbour spacing.

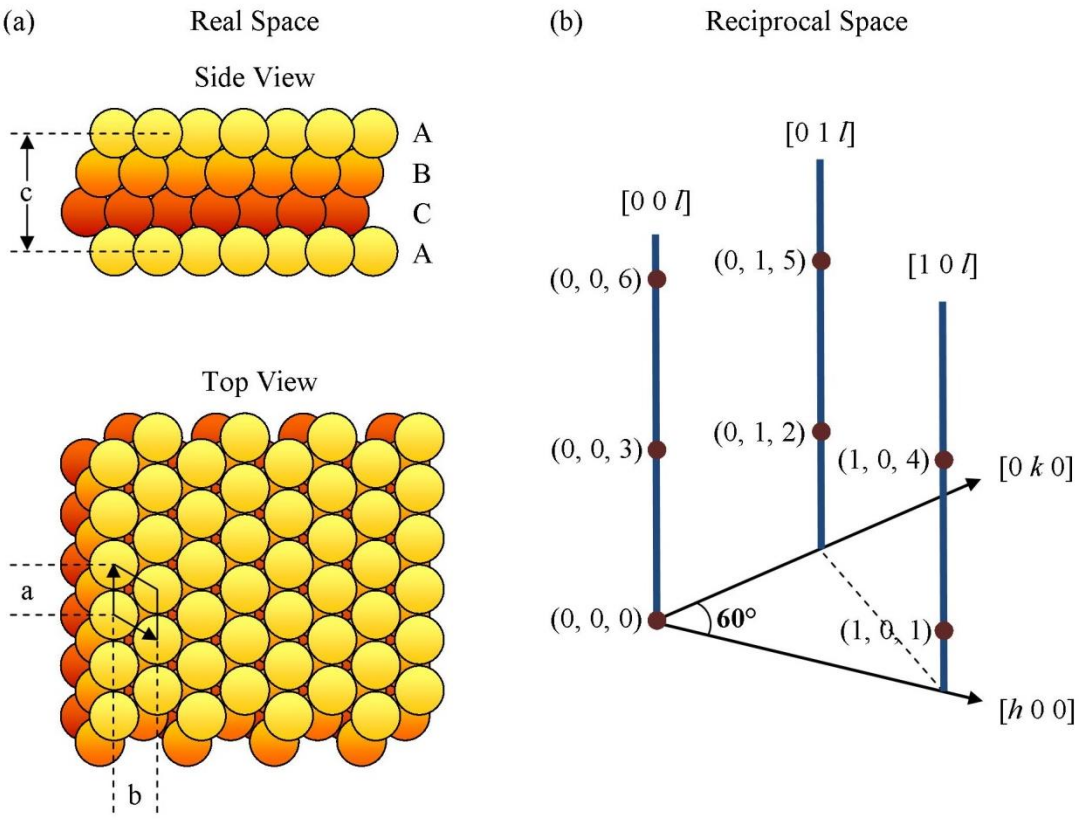

Figure 2.7 Schematic showing (a) the real-space surface structure for fcc(111) and (b) the corresponding reciprocal space lattice showing the Bragg reflections (solid circles) and CTR's (vertical lines).

The resultant reciprocal lattice is shown in Figure 2.7(b) where the $[h, 0, 0]$ and $[0, k, 0]$ directions are in the plane of the surface subtending an angle of $60°$ and the $[0, 0, l]$ direction is along the surface normal. The units of h, k and l are defined as:

$$\boldsymbol{a}^* = \boldsymbol{b}^* = \frac{4\pi}{\sqrt{3}a_{NN}} \quad \text{and} \quad \boldsymbol{c}^* = \frac{2\pi}{\sqrt{6}a_{NN}} \qquad (2.26)$$

The hexagonal surface notation, (h, k, l), is related to the conventional cubic notation, $(h, k, l)_{cubic}$, as follows:

$$h_{cubic} = \frac{2}{3}h - \frac{2}{3}k + \frac{1}{3}l$$

$$k_{cubic} = \frac{2}{3}h + \frac{4}{3}k + \frac{1}{3}l$$

$$l_{cubic} = -\frac{4}{3}h - \frac{2}{3}k + \frac{1}{3}l \qquad (2.27)$$

Using this notation the $(1,1,1)_{cubic} = (0,0,3)$, $(0,2,0)_{cubic} = (0,1,2)$ and $(1,1,\bar{1})_{cubic} = (1,0,1)$ etc. The hexagonal notation will be used throughout this thesis. The Bragg peaks in Figure 2.7(b) (represented by circles) are given this notation and are separated by 3 units of l due to the ABC stacking along the surface normal direction. The vertical lines through them represent the CTR's.

The total scattered intensity is due to interference effects between the x-rays scattered from the bulk crystal and those scattered from the surface layers. The corresponding structure factors for fcc (111) are defined below using the hexagonal notation.

The phase difference between consecutive atomic layers is given by $e^{2\pi i\left(-\frac{h}{3}+\frac{k}{3}+\frac{l}{3}\right)}$, and from this the Bulk structure factor may be written as:

$$F_{Bulk} = f(\boldsymbol{q})\, DW_{Bulk} \sum_{n=0}^{-\infty} e^{i\, n\left[2\pi\left(-\frac{h}{3}+\frac{k}{3}+\frac{l}{3}\right)\right]}$$

$$= \frac{f(\boldsymbol{q})\, DW_{Bulk}}{1 - e^{-2\pi i\left(-\frac{h}{3}+\frac{k}{3}+\frac{l}{3}\right)}} \qquad (2.28)$$

where $f(\boldsymbol{q})$ is the atomic form factor and DW_{Bulk} is the bulk Debye-Waller factor. The bulk Debye-Waller factor accounts for the thermal disorder of bulk atoms and is related to the root-mean-squared (rms) displacement of atoms about their average positions, σ. The bulk Debye-Waller factor is defined:

$$DW_{Bulk} = e^{-\frac{1}{2}\boldsymbol{q}^2\langle\sigma_{\boldsymbol{q}}{}^2\rangle} \quad (2.29)$$

where $\langle\sigma_{\boldsymbol{q}}{}^2\rangle$ is the thermal average component of the displacement parallel to $\boldsymbol{q}$ and can be calculated by:

$$\langle\sigma_{\boldsymbol{q}}{}^2\rangle = \frac{B}{8\pi^2} \quad (2.30)$$

The B-factor, B, can be found, for many elemental crystals, as a function of temperature in elementary book e.g. [15].

To account for the structural differences at the surface the three outermost atomic layers are considered separately from the bulk as follows:

$$F_{Surf} = f(\boldsymbol{q})\theta_n\, DW_n e^{2\pi i\left[n\left(-\frac{h}{3}+\frac{k}{3}+l\left[\frac{1}{3}+\epsilon_n\right]\right)\right]} \qquad \text{For } n = 1,2,3 \quad (2.31)$$

Here the structural variables are; the occupation of the surface layer relative to the bulk, θ_n, which is included simply as a fraction (from 0 to 1 ML), the Debye-Waller factor, DW_n, which may differ from the bulk due to differences in the interatomic bond strengths in the near surface region, and finally the surface relaxation, ϵ_n, which represents the displacement of the surface layer along the surface normal direction. Each parameter is considered independently for each of the three surface atomic layers.

The surface structure factor, F_{Surf}, can be added to the bulk structure factor, F_{Bulk}, to give the total structure factor, F_{Tot}, from which the total scattered intensity can be calculated.

$$|F_{Tot}|^2 = |F_{Bulk} + F_{Surf}|^2 \quad (2.32)$$

Finally the total scattered intensity is given by:

$$I(\boldsymbol{q})_{Tot} = I_i \left(\frac{e^2}{mc^2}\frac{1}{R_0}\right)^2 |F_{Tot}|^2 \, {N_1}^2 {N_2}^2 \, \frac{1}{2\,sin^2(\boldsymbol{q}\cdot\boldsymbol{c}/2)} \qquad (2.33)$$

2.4.3 Crystal Truncation Rod Profiles

Figure 2.8 shows 3 different CTR profiles for an fcc(111) single crystal obtained using a theoretical model and illustrates how the surface properties effect the CTR. The solid black line represents an fcc(111) single crystal with a perfectly terminated surface. The Bragg peaks occur when the Laue conditions are satisfied causing a maximum in intensity and are spaced 3 c* apart in l as previously explained. The positions half way between adjacent sets of Bragg peaks are called the anti-Bragg positions. The intensity at the anti-Bragg positions is a minimum as the scattering from the bulk crystal is cancelled out and only the top most atomic layer contributes. If the occupation of this topmost layer is reduced, the intensity at (and near to) the anti-Bragg decreases, as shown by the blue dashed line in Figure 2.8. A relaxation of the top most layer (either an expansion or contraction of the top most atomic plane along the surface normal direction) causes asymmetry in the CTR profile as shown by the dotted red line in Figure 2.8.

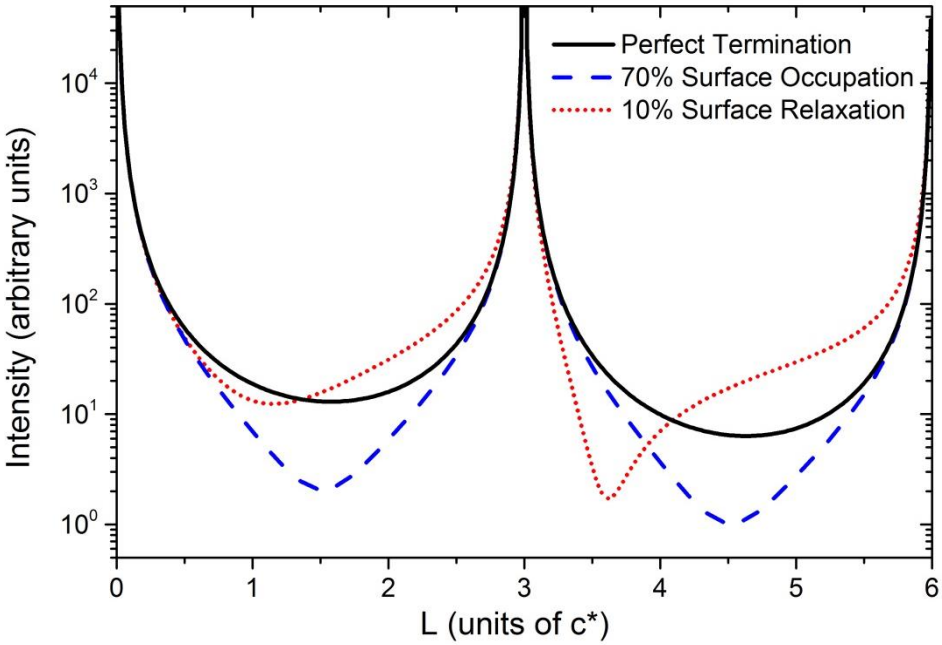

Figure 2.8 CTR profile from an fcc(111) single crystal for the case of a perfectly terminated surface (solid black line), a surface layer with a relative occupation of 70% (dashed blue line) and a surface layer with a surface relaxation of 10% (dotted red line).

The CTR's shown in Figure 2.8 are along the $[0, 0, l]$ direction which is termed the specular direction. The specular CTR $(0, 0, l)$ is unique in that it is dependant only on the surface normal component of the momentum transfer. As a result of this it is uniquely sensitive to any layer ordering in the surface normal direction even when the layers are incommensurate with the underlying bulk or have no in plane ordering. Modelling the specular CTR can hence be used to obtain information about incommensurate layers including the electrolyte above the surface. All other CTR's, for example $(1, 0, l)$, $(0, 1, l)$ and $(1, 1, l)$, are termed non-specular and have an additional in-plane component of the momentum transfer. Modelling of non-specular CTR's can be used to obtain information about the in-plane position of atoms in any commensurate layers. Accounting for commensurate and incommensurate adlayers in the model will be addressed in the following section 2.4.4.

2.4.4 Commensurate and Incommensurate Adlayers

So far we have only considered the termination of a bulk crystal, however it is also possible to adapt equation (2.31) to model additional layers commensurate with the bulk consisting of a different element and even incommensurate structures such as ordering in the electrolyte above the surface. The total form factor from such a system would now be:

$$|F_{Tot}|^2 = |F_{Bulk} + F_{Surf} + F_{Com} + F_{Incom}|^2 \qquad (2.34)$$

where F_{Com} and F_{Incom} are due to commensurate and incommensurate adlayers respectively. This can be used with equation (2.33) to model the total intensity. To model commensurate layers of a different element, for example Ag, $f(\boldsymbol{q})$ from equation (2.31) is replaced by $f(\boldsymbol{q})_{Ag}$ to account for the different atomic form factor of the topmost layers. The three other structural variables, θ_n , DW_n and ϵ_n would also be changed to, θ_{Ag} , DW_{Ag} and ϵ_{Ag} corresponding to the occupation, Debye-Waller factor and surface relaxation of the commensurate layers. The commensurate form factor for up to 3 layers of Ag commensurate with the underlying bulk crystal can then be written as:

$$F_{Com} = f(\boldsymbol{q})_{Ag}\theta_{Ag}\, DW_{Ag} e^{2\pi \mathrm{i}\left[Ag\left(-\frac{h}{3}+\frac{k}{3}+l\left[\frac{1}{3}+\epsilon_{Ag}\right]\right)\right]} \text{ For } Ag = 1,2,3 \qquad (2.35)$$

An incommensurate layer, for example K^+, can also be modelled using the following formula:

$$F_{Incom} = f(\boldsymbol{q})_{K^+}\theta_{K^+}\, DW_{K^+} e^{2\pi \mathrm{i}l\left[1+\epsilon_{K^+}\right]} \qquad (2.36)$$

Since this is only dependant on the surface normal direction l only the specular $(0,0,l)$ CTR is sensitive to changes.

Figure 2.9 illustrates the addition of an ideal monolayer (blue dashed line) or ideal bilayer (red dotted line) to the previously described perfectly terminated crystal (solid black line). In Figure 2.9 both the monolayer and bilayer are commensurate with the bulk and follow the same ABC stacking as the bulk. The addition of a monolayer of a different element to the bulk causes the intensity at the anti-Bragg position to decrease considerably. The shape of the CTR is dependent on the number of commensurate layers. With the addition of a second layer there are 2 minima between each set of Bragg peaks as shown by the red dotted line.

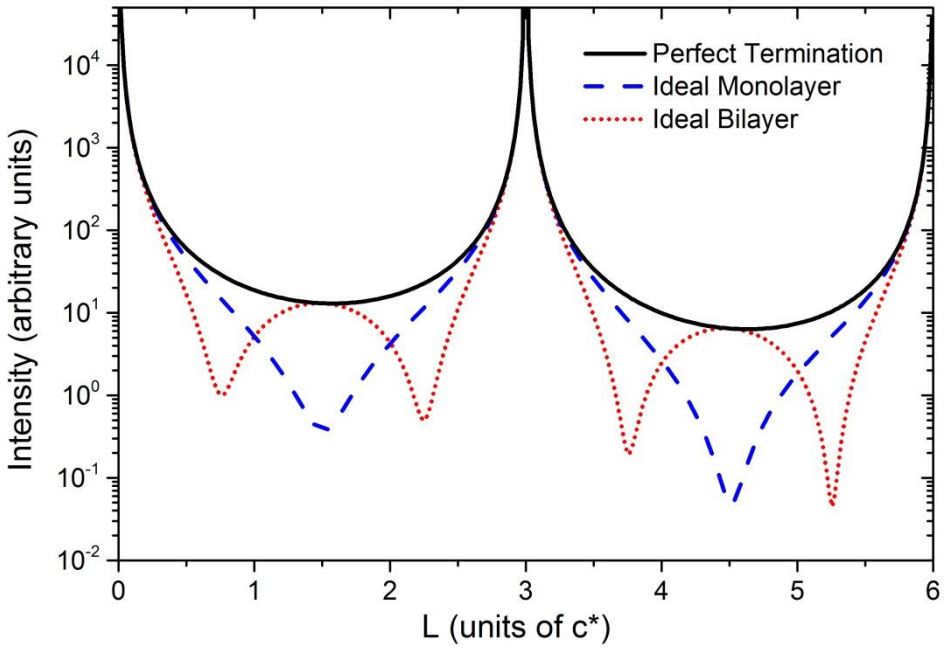

Figure 2.9 CTR profile from an fcc(111) single crystal for the case of a perfectly terminated surface (solid black line), a commensurate monolayer of a different element to the bulk (dashed blue line) and a commensurate bilayer of a different element to the bulk (dotted red line).

X-ray diffraction measurements can be performed with the sample in electrolyte and under electrochemical control. This allows potentiostatic CTR measurements to be done which involves measuring the CTR's at fixed potentials. By modelling this data detailed information about potential dependant changes in the surface

and interface can be obtained. To summarise the following information can be obtained by modelling specular and non-specular CTR's:

- Details of the three outermost atomic layers of the bulk crystal in terms of their occupation, θ_n, Debye-Waller factor, DW_n, and surface relaxation, ϵ_n.
- Details of any commensurate atomic layers of a different element in terms of their in-plane position, occupation, θ_n, Debye-Waller factor, DW_n, and surface relaxation, ϵ_n.
- Details of an incommensurate layer, such as a layer in the electrolyte, in terms of its occupation, θ_n, Debye-Waller factor, DW_n, and surface relaxation, ϵ_n.
- Potential dependant changes in the surface and interface.

2.5 Electrochemistry

Electrochemistry involves the study of chemical reactions connected with the transfer of electrical charge (an electron or an ion) between an electrode and the chemical species contained within an electrolyte. Typical examples of reactions are; oxidation/reduction which involves electron transfer, and deposition/dissolution of a metal, a form of ion transfer. Since electrochemistry revolves around the electrostatic interactions between the electrode and electrolyte ions (and solvent molecules) in solution, understanding of the electrode/electrolyte interface is crucial [16].

2.5.1 Electrode/Electrolyte Interface

The theory of the electrode/electrolyte interface has been developed since the 19th Century when Helmholtz proposed that the distance of closest approach for an ion in the electrolyte is limited by the solvation shell of the ion. The minimum distance from the electrode surface to the centre of the ion is called the Outer Helmholtz Plane (OHP). Helmholtz suggested that the excess charge on the metal is balanced

completely in the solution by the ions in the OHP with potential drop across the interface occurring only over this region. The electrode/electrolyte interface is called the electrical double layer and is equivalent to an electrical capacitor.

In this model it is assumed that no electron transfer reactions occur at the electrode. The charge density on the electrode interface as a whole is electrically neutral such that the charge on the electrode is balanced by an equal and opposite charge in the electrolyte. The charge arises from the redistribution of electrolyte ions at the interface / reorientation of dipoles in solvent molecules.

Gouy and Chapman later concluded that the excess charge density in the solution is not exclusively in the OHP due to Brownian motion in the electrolyte. In 1924 Stern combined the 2 ideas such that there is an initial sharp drop between the electrode (ϕ_m) and the OHP (ϕ_{OHP}) followed by a gradual fall. In 1947 Grahame made a further addition to the model by proposing that if the ion has no solvation shell or if the ion has lost its solvation shell on approach to the electrode surface then it may penetrate the OHP. In this case the ion is in direct contact with the electrode and is said to be 'specifically adsorbed'. The new plane of minimum approach is termed the Inner Helmholtz Plane (IHP). The general effect of the specific adsorption is to reduce the charge density needed in solution in the double layer to compensate the charge on the electrode. A schematic representation of the Grahame model of the electrode/electrolyte interface is shown in Figure 2.10. [16-19]

Since the Grahame model of the electrical double layer there have been extensive studies and vast advances in the understanding of the electrode surface. This has been driven by development of experimental techniques, such as; new methods in situ (in an electrochemical environment) including STM and XRD, the ability to produce high quality single crystals and electrodes and UHV techniques to study surfaces after electrochemical treatment, together with improvements in theoretical concepts [20]. These advances have enabled in situ atomic scale characterisation of countless surface structures such as surface reconstructions,

metal adlayers, specifically absorbed anions and nanostructures [16, 21-24]. Understanding the motion and interaction of atoms at the electrode/electrolyte interface is of crucial to developing knowledge of the mechanisms behind surface processes. For this dynamic studies of the real time surface changes and reactions are required. Dynamic, potential dependant, surface transformations have previously been studied for anion absorption [25] and UPD systems on single crystal electrodes [26-28]. The recent development of high-speed STM, also known as Video-STM, by the Interface Physics Group at Kiel University, lead by Prof. Olaf Magnussen, has enabled the direct observation of dynamic processes in the electrochemical environment with atomic scale resolution and millisecond time resolution [29-31]. Another challenge is determining the structure of the electrolyte at the electrode/electrolyte interface. This has been handled theoretically but experimental confirmation is needed as theoretical approach often gives conflicting answers. In recent years x-ray diffraction measurements have started to explore the structure of the electrolyte [20, 32-36], but there is still a great deal to understand.

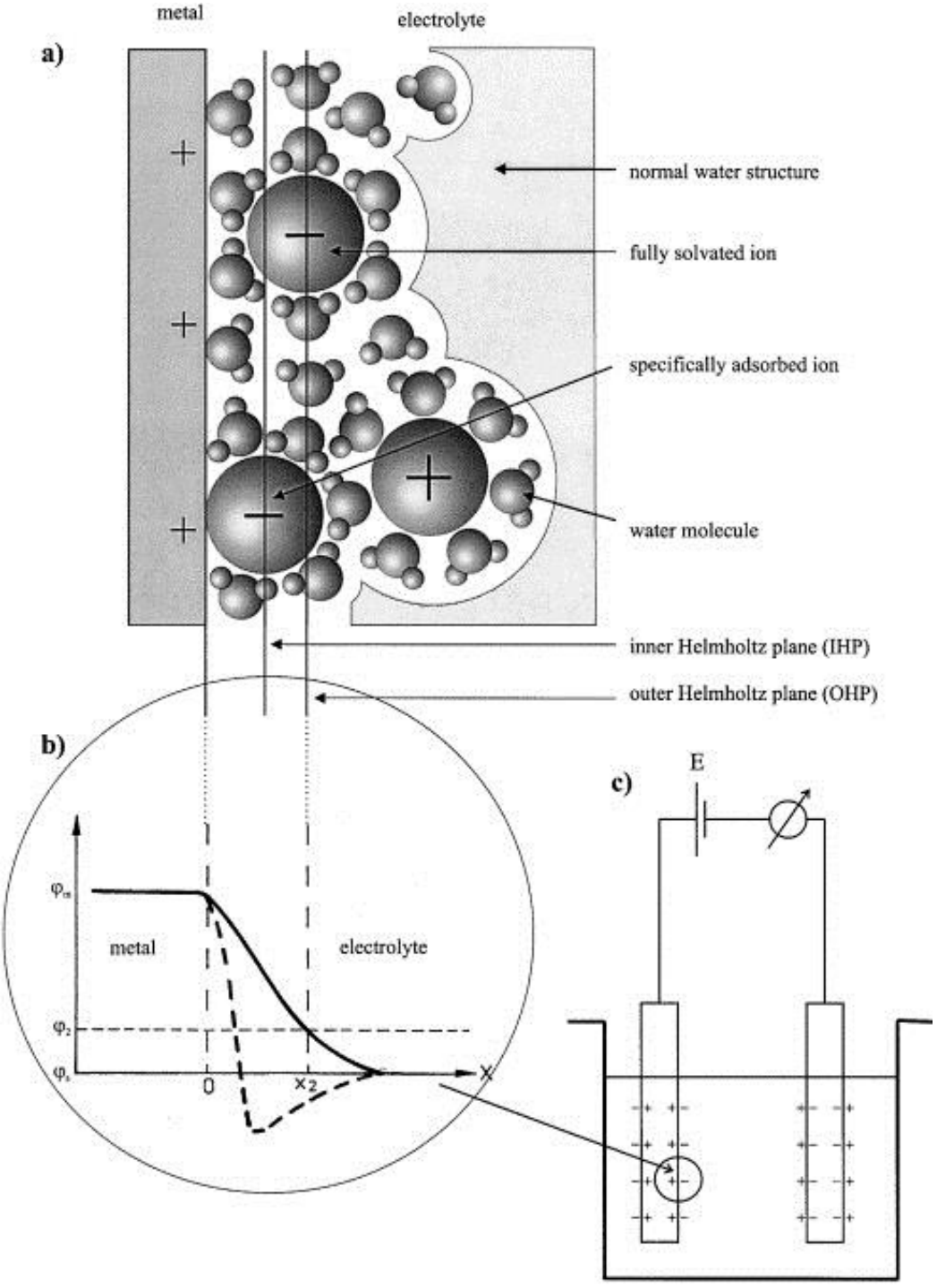

Figure 2.10 (a) Schematic diagram of the electrode/electrochemical interface showing fully solvated and specifically adsorbed anions. (b) Potential drop across the interface in the case of fully solvated (solid line) and specifically adsorbed anions (dashed line). (c) Schematic diagram of an electrochemical cell. Reprinted from Surface Science, 500, Kolb, D. M., An atomistic view of electrochemistry, 722-740, Copyright (2001), with permission from Elsevier.

2.5.2 Cyclic Voltammetry

Electrochemical reactions can be driven and controlled by a voltage applied to the electrode or if the reaction occurs spontaneously can provide electrical current. Hence electrochemistry is seen as a tool for generating electricity, with research into batteries and fuel cells, as well as being important for understanding of processes such as corrosion and applications such as metal plating.

The electrode possesses a charge which can be controlled by the voltage applied to the electrode. Cyclic voltammetry (CV) is a technique that exploits this by measuring the current from an electrode as a function of the applied voltage. It is a measurement of electron transfer and as a result there is no direct information about the chemical or structural changes taking place therefore it is best used in conjunction with techniques such as SXS or STM. Sharp peaks in the cyclic voltammogram are seen as a result of electron transfer to and from the surface due to the formation / breaking of bonds during electrochemical reactions. Other processes such as adsorption / desorption of ionic species from the solution, ordering / disordering of adsorbate layers or structural transitions within the electrode surface will also create peaks and shoulders in the CV.

The electrochemical cell, used for CV measurements, consists of a working electrode (WE) ie the single crystal or sample, counter electrode (CE) such as a metal wire and reference electrode (RE) which provides a stable reference for measurements of the potential drop across the working electrode/solution interface. The reference electrode used for majority of the experiments reported in this thesis was the Ag/AgCl (silver / silver chloride) electrode, although some results are reported versus other electrodes such as the reversible hydrogen electrode (RHE). The potential of the counter electrode is held relative to the reference such that current only flows between the counter and the working electrodes. For a CV experiment the potential applied to the working electrode is varied as a function of time as shown in Figure 2.11 (a) and the current is measured and plotted versus potential in the CV shown in Figure 2.11 (b). Here E_1 and E_2

define the potential range. Figure 2.11 (b) shows the CV for a reversible electrode transfer reaction. From the CV, the positions of peaks give information of the potential at which the reactions occur, and integration of the current under the peaks can give details of the surface coverage for process such as anion adsorption and metal stripping [16, 18, 19, 37].

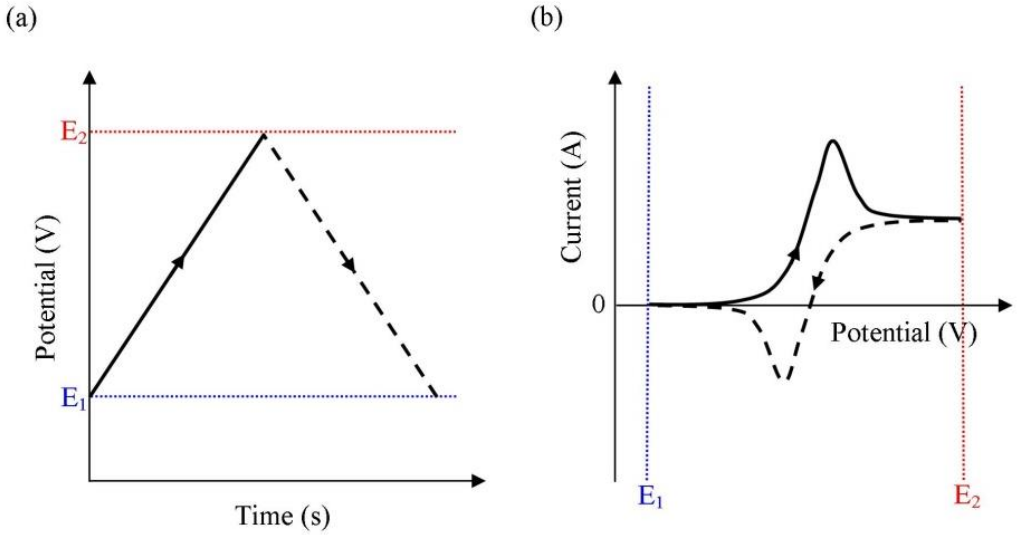

Figure 2.11 (a) Variation of potential with time in a cyclic voltammetry experiment and (b) typical cyclic voltammogram for a reversible electron transfer reaction.

2.6 X-ray Voltammetry

X-ray voltammetry (XRV) is a surface sensitive potentiodynamic x-ray diffraction technique, which can be used alongside potentiostatic CTR measurements to obtain a better understanding of the structural changes and chemical processes occurring at the surface. XRV exploits the fact that certain positions along the CTR are sensitive to specific structural changes, for example, as is evident from Figure 2.8 by the red dotted line, positions either side of the bragg peak are sensitive to surface relaxation [38]. The technique involves measuring the scattered intensity at a fixed position in reciprocal space whilst sweeping the potential. By comparing XRV measurements with CV it is possible to link the electrochemical processes to

the structural changes occurring at the surface. Measurements may show greater hysteresis then in the corresponding CV as the intensity is sensitive to structural changes which are often much slower than the electron transfer measured by CV. It can also be a very helpful indicator of the stability of the surface over a given potential range, since if the surface is not stable then the measured intensity will decay irreversibly.

To perform an XRV experiment first a reciprocal space position is identified, either from prior knowledge of the surface, such as a position sensitive to the reconstruction of Au(111), or via direct structural scans which have located a structure of interest, such as a metal monolayer. The diffractometer is then moved to this position and a rocking scan is performed (one of the diffractometer motors is rotated, through ± 2-4°, and the detector counts are recorded) see Chapter 3 for more details of the experimental set up. If there is a structure present then the rocking scan should contain a peak (the rocking scan is also used to background subtract the data during analysis). The detector is positioned at the centre of the peak in the rocking scan and kept stationary as the potential is slowly cycled through the desired potential range, usually the same as for the CV measurements. The potential steps are kept large, usually 20mV or 50mV per step, and the diffracted intensity is recorded for at least 10 seconds at each step. This results in a potential rate of 2-5 mV/s. The structural changes are often slower than the charge transfer recorded by the CV measurements, and the large, slow potential steps allow for good counting statistics in the x-ray measurement and trends in the intensity to be clearly identified. Usually a set of XRV measurements are performed successively at different reciprocal space positions. With knowledge of the structural and/or process that each position represents the XRV measurements can be used to gain an understanding of the processes occurring at the surface due to changes in the potential. XRV measurements can be used to monitor reciprocal space positions sensitive to; surface relaxation, surface reconstruction, electrochemical deposition/stripping processes, changes in an adsorbed adlayer

and even ordering in the electrochemical double layer. As an example, the scattered intensity at the non-specular anti-Bragg position is only sensitive to atoms commensurate with the underlying bulk structure. However changes in the scattered intensity at the specular anti-Bragg position are sensitive to any layer ordering, whether it is commensurate or incommensurate with the bulk, such as a disordered oxide layer or an ordered structure in the electrolyte. Therefore comparing the XRV from both positions can give a good indication if the changes are due to atoms commensurate or incommensurate with the underlying bulk structure [27, 39].

2.7 References

[1] K. Charles, Introduction to Solid State Physics, 8th ed., Wiley, Danvers, MA, (2005).
[2] J. Als-Nielsen, Elements of Modern X-Ray Physics, Wiley, New York, (2001).
[3] I.K. Robinson, D.J. Tweet, Rep Prog Phys, 55 (1992) 599-651.
[4] R. Feidenhans'l, Surface Science Reports, 10 (1989) 105-188.
[5] P.H. Fuoss, S. Brennan, Annu Rev Mater Sci, 20 (1990) 365-390.
[6] B.E. Warren, X-ray Diffraction, Addison-Wesley, Reading, (1969).
[7] International Tables for Crystallography, 1st online ed., Wiley, Chester: International Union of Crystallography, (2006).
[8] J.L. Hodeau, V. Favre-Nicolin, S. Bos, H. Renevier, E. Lorenzo, J.F. Berar, Chem Rev, 101 (2001) 1843-1867.
[9] A. Menzel, K.C. Chang, V. Komanicky, H. You, Y.S. Chu, Y.V. Tolmachev, J.J. Rehr, Radiat Phys Chem, 75 (2006) 1651-1660.
[10] A.C. Thompson, X-ray Data Booklet, 3rd ed., Lawrence Berkeley National Laboratory California, (2009).
[11] I.K. Robinson, Phys Rev B, 33 (1986) 3830-3836.
[12] J. Wang, B.M. Ocko, A.J. Davenport, H.S. Isaacs, Phys Rev B, 46 (1992) 10321-10338.
[13] A.R. Sandy, S.G.J. Mochrie, D.M. Zehner, K.G. Huang, D. Gibbs, Phys Rev B, 43 (1991) 4667-4687.
[14] C.A. Lucas, N.M. Markovic, Structure Relationships in Electrochemical Reactions, in: E.J. Calvo (Ed.) Encyclopedia of Electrochemistry, vol. 2, Wiley, Weinheim, (2007).
[15] L.M. Peng, G. Ren, S.L. Dudarev, M.J. Whelan, Acta Crystallogr A, 52 (1996) 456-470.
[16] D.M. Kolb, Surf Sci, 500 (2002) 722-740.
[17] D.C. Grahame, Chem Rev, 41 (1947) 441-501.
[18] A.C. Fisher, Electrode Dynamics, Oxford University Press, Oxford, (2006).
[19] A.J. Bard, L.R. Faulkner, Electrochemical Methods: Fundamentals and Applications, 2nd ed., Wiley, Hoboken, (2001).
[20] D.M. Kolb, Angew Chem Int Edit, 40 (2001) 1162-1181.
[21] D.M. Kolb, Prog Surf Sci, 51 (1996) 109-173.
[22] E. Herrero, L.J. Buller, H.D. Abruna, Chem Rev, 101 (2001) 1897-1930.
[23] P. Allongue, F. Maroun, J Phys-Condens Mat, 18 (2006) S97-S114.
[24] K. Itaya, Prog Surf Sci, 58 (1998) 121-247.
[25] C. Safarowsky, A. Spaenig, P. Broekmann, K. Wandelt, Surf Sci, 538 (2003) 137-146.
[26] L.Y.O. Yang, F. Bensliman, C.H. Shue, Y.C. Yang, Z.H. Zang, L. Wang, S.L. Yau, S. Yoshimoto, K. Itaya, J Phys Chem B, 109 (2005) 14917-14924.
[27] S.H. Zheng, K. Krug, F. Golks, D. Kaminski, S. Morin, O.M. Magnussen, J Electroanal Chem, 649 (2010) 189-197.

[28] Y.G. Dai, C. Meier, U. Ziener, K. Landfester, C. Taubert, D.M. Kolb, Langmuir, 23 (2007) 11058-11062.
[29] L. Zitzler, B. Gleich, O.M. Magnussen, R.J. Behm, Localized in-Situ Methods for Investigating Electrochemical Interfaces, 99 (2000) 29-38.
[30] O.M. Magnussen, W. Polewska, L. Zitzler, R.J. Behm, Faraday Discuss, 121 (2002) 43-52.
[31] T. Tansel, O.M. Magnussen, Phys Rev Lett, 96 (2006).
[32] M. Nakamura, N. Sato, N. Hoshi, O. Sakata, Chemphyschem, 12 (2011) 1430-1434.
[33] C.A. Lucas, P. Thompson, Y. Grunder, N.M. Markovic, Electrochem Commun, 13 (2011) 1205-1208.
[34] D. Strmcnik, K. Kodama, D. van der Vliet, J. Greeley, V.R. Stamenkovic, N.M. Markovic, Nat Chem, 1 (2009) 466-472.
[35] M.F. Toney, J.N. Howard, J. Richer, G.L. Borges, J.G. Gordon, O.R. Melroy, D.G. Wiesler, D. Yee, L.B. Sorensen, Nature, 368 (1994) 444-446.
[36] M.F. Toney, J.N. Howard, J. Richer, G.L. Borges, J.G. Gordon, O.R. Melroy, D.G. Wiesler, D. Yee, L.B. Sorensen, Surf Sci, 335 (1995) 326-332.
[37] R.G. Compton, G.H.W. Sanders, Electrode Potentials, Oxford University Press, Oxford, (2006).
[38] D.D. Fong, C.A. Lucas, M.I. Richard, M.F. Toney, Mrs Bull, 35 (2010) 504-513.
[39] C.A. Lucas, J Phys D Appl Phys, 32 (1999) A198-A201.

Chapter 3:

Experimental Details

3.1 Introduction

The previous chapter dealt with the theory behind x-ray diffraction; however successful x-ray diffraction and electrochemistry experiments require careful preparation of the sample and precise control of the sample environment. This Chapter details the procedures for sample preparation and subsequent transfer to electrochemical environment, including a description of the electrochemical cells used. Following this there is a brief explanation of the experimental equipment that makes up a synchrotron beamline and details of the similarities and differences between the beamlines used for the experiments contained within this Thesis. Finally an outline of the experimental process for the collection and subsequent analysis of data is given.

3.2 Single Crystal Sample Preparation

High quality single crystals which have been precisely orientated to the desired crystallographic direction are required for surface X-ray diffraction experiments as, in order to align the samples and get good quality data, the surface plane must be parallel to the corresponding bulk planes. The crystals should be free of defects and contamination and carefully prepared prior to each experiment. The single crystals are ordered from MaTeck in Juelich, Germany to ensure quality of crystal growth and cut [1]. In this thesis the samples are Au single crystals aligned to the [111] crystallographic orientation with a miscut < 0.2°. The crystals are typically disc shaped and range in diameter from 6-10mm with a thickness of 2-3mm. To enable easier handling during experiments the discs may be ordered with a groove around the circumference or 'top hat' geometry. The crystals are polished by MaTeck but require preparation using Ultra High Vacuum (UHV) techniques and flame annealing before first use in order to obtain an atomically smooth surface.

The Au(111) single crystals are prepared in a UHV system by repeated cycles of ion sputtering and thermal annealing. The sputtering involves Argon ion bombardment at an energy of 1.0 kV with a flux hitting the sample of around 20 micro amps. The crystal is annealed to 600 °C, which is around 2/3 of the bulk melting point of the material. Once a sharp low-energy electron diffraction (LEED) pattern showing the (√3x23) reconstruction is observed the sample is removed from UHV. Typically 5 - 10 cycles will be needed for a new crystal. The sample is also checked for contamination using XPS. Prior to each experiment the crystal is flame annealed in a butane flame, until glowing red for approximately 2 minutes, before cooling in air. This step is important as upon cooling the surface atoms rearrange to the lowest energy configuration, leading to the desired (111) surface structure, so the cooling should not be rushed. The crystal is then transferred to the electrochemical cell (see Section 3.3) with a drop of ultrapure water or electrolyte protecting the surface and then immersed in electrolyte at open circuit potential.

Often, for Au(111), only flame annealing is required prior to experiments as Au is not easily oxidised meaning it can be left in air between experiments and the (111) surface is the most energetically favourable configuration, so the surface should not deteriorate with successive anneals as long as they are performed properly. However with use the crystal may periodically need further UHV preparation to ensure a high quality surface and may also occasionally require polishing. The polishing procedure requires manual polishing with a 0.1 µm diamond paste and lubricating fluid until an optically good surface is obtained. After polishing the sample is washed in ultrapure water and placed in an ultrasonic bath to remove any remaining paste. The sample is then prepared using the UHV and flame annealing techniques described above.

3.3 Electrochemical Cells

All the electrochemical cells used consist of a single crystal working electrode (WE), counter electrode (CE) and reference electrode (RE). They are designed to be easily cleaned in concentrated acid and to allow the best geometric configuration (for current flow) of the components achievable whilst still being suitable for the other techniques used (for example x-ray diffraction). Acid resistant plastics such as PCTFE (Kel-F), PTFE (Teflon) and EFTE (Tefzel) are used as well as glass for any parts which come in to contact with the electrolyte. The materials are also chosen for their strength and durability. The cleaning procedure followed for both glass and acid resistant plastics is to fill them with/leave them in the concentrated acid, 1:1 H_2SO_4 and HNO_3, for a minimum of 12 hours for glass and 24 hours for plastics. This removes any traces of biological substances such as grease from fingers which can perturb the electrochemical processes. It will not remove all metallic contaminants so the glass/plastics should be washed in water prior to acid cleaning to physically remove these. Once this has finished (and the used acid safely disposed of) the items are carefully and repeatedly washed in ultrapure water, filled with ultrapure water and brought to the boil on a hot plate and finally left in/containing fresh

ultrapure water for a further 1-2 days to make sure all the residual acid is removed. Three main cell designs are used, two for x-ray diffraction and one for cyclic voltammetry. Both electrochemical x-ray cells are designed so that the single crystal electrode is always in contact with the electrolyte whilst the path length for the incident and diffracted x-rays through the electrolyte is kept to a minimum.

3.3.1 Electrochemistry Hanging Meniscus Glass Cell

The hanging meniscus cell is used for cyclic voltammetry experiments; it can contain a large volume of electrolyte, which allows for good mass transport and is ideal for obtaining high quality cyclic voltammetry and other electrochemistry data. It is in many ways the simplest set up and useful starting point for explaining some key aspects. Figure 3.1 is a schematic diagram of a hanging meniscus cell. Since we are only interested in the processes occurring at the well-ordered single crystal electrode surface the hanging meniscus set up is used to ensure that only the surface of the crystal is in contact with the electrolyte. The electrolyte is deoxygenated by purging with N_2 gas prior to the experiment and during measurements an N_2 atmosphere is maintained. A Pt or Au mesh is usually used for the counter electrode and metal wires are also used for the contact to the single crystal. These need to be of high purity to prevent contamination of the experiment and are prepared by rinsing in ultrapure water and flame annealing for a few seconds until red hot. The reference electrodes used for the majority of experiments within this thesis are leak free Ag/AgCl from manufactures World Precision Instruments, USA (Ag/AgCl Flexref) and Thermo Fisher Scientific, UK (66-EE009 no leak Ag/AgCl). An Autolab or Princeton Potentiostat was used to perform the electrochemical measurements.

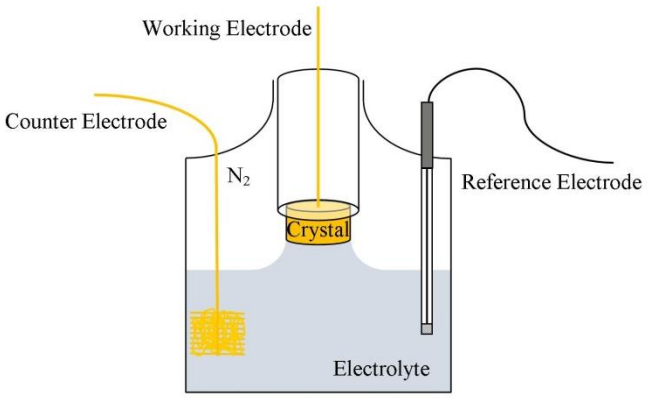

Figure 3.1 Schematic representation of a Hanging meniscus cell. The single crystal surface (working electrode) forms a meniscus with the electrolyte surface.

3.3.2 The Electrochemical Thin-layer X-ray Cell

The electrochemical thin-layer x-ray cell is shown both schematically and in photographs in Figure 3.2. The main body of the cell is machined from a single piece of PCTFE and the whole cell once assembled is designed to be leak free, to electrolyte out or air in, for at least 48 hours. The single crystal is held firmly in the centre of the cell and forms the highest point of the cell. The same reference electrodes are used as for the hanging meniscus cell and the counter electrode is a Pt or Au wire of thickness 0.5mm (the same wire is also used to contact the crystal). The electrolyte may be exchanged through an in-let and out-let at the bottom of the cell. Fittings, bought from IDEX Health & Science, USA, precisely match the dimensions of the wire, reference electrodes and electrolyte tubing. A polypropylene film confines the electrolyte and is held in place with a rubber O-ring. A Kapton film 'hood' surrounds the cell and allows for a controlled atmosphere to be maintained. The cell has two modes of operation. (1) The film may be inflated to facilitate electrochemical processes such as metal deposition. (2) The film may be collapsed to minimise the x-ray path length through the electrolyte for optimal x-ray intensity at the detector. The polypropylene film used is boiled, for approximately 15 minutes, to make it hydrophilic and when collapsed traps ~10

µm of electrolyte on the surface of the crystal. This x-ray cell is stable at any angle, even upside down, which allows it to be used on most diffractometers. However, focused x-ray beams of energy > 15 KeV can be problematic as the can damage the polypropylene film.

Similarly to the hanging meniscus cell a potentiostat is used to control the electrochemical cell during SXS measurements. The potentiostat can be controlled independently of the diffraction measurements, on a separate computer using the manufactures software. However it is useful to integrate the device commands into the beamline software, SPEC (ESRF and APS) or GDA (Diamond Light Source), so that changes in the surface can be correlated directly to the applied potential.

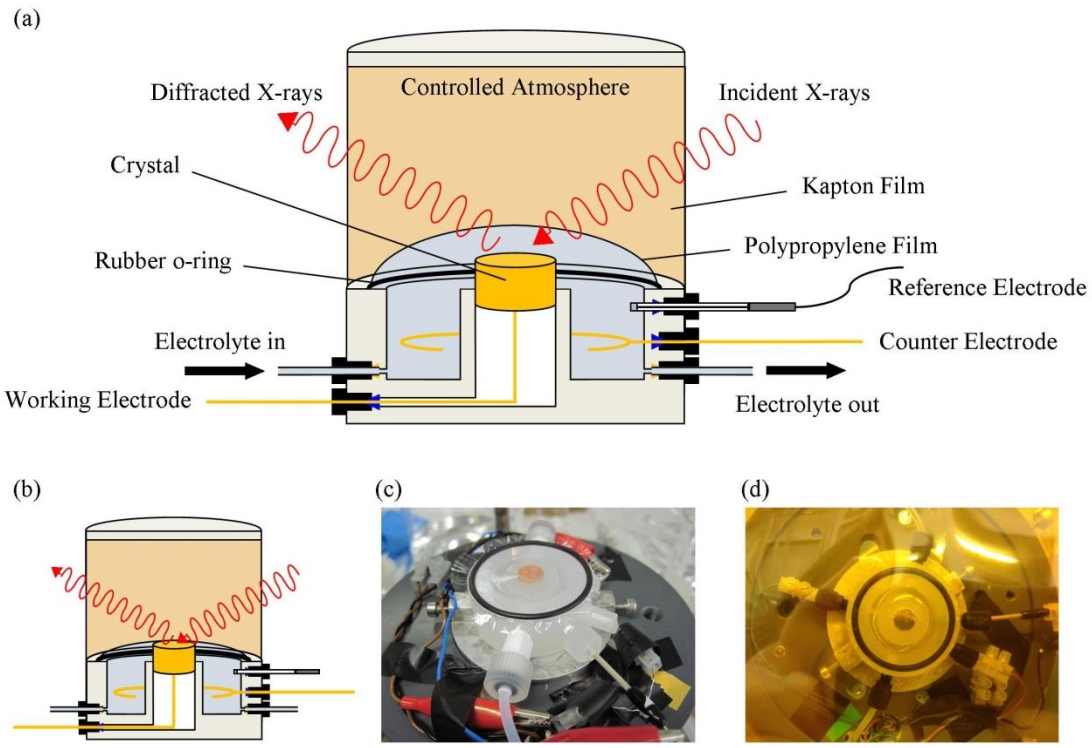

Figure 3.2 (a) and (b) schematic showing electrochemical thin-layer x-ray cell with the film inflated and collapsed respectively. (c) and (d) show photographs of the electrochemical thin-layer x-ray cell in use.

3.3.3 Electrochemical Droplet X-ray Cell

The electrochemical droplet x-ray cell is shown both schematically and in a photograph in Figure 3.3. The single crystal electrode is held in place in a similar manner to the electrochemical thin-layer x-ray cell but, rather than being surrounded by electrolyte, a droplet of electrolyte makes contact with the surface. A cross piece held directly above the crystal contains the electrolyte and reference electrode. The counter electrode forms a small ring several millimetres above the crystal surface and helps support the electrolyte droplet. The droplet size can be controlled by the electrolyte in-let and out-let. Kapton film surrounds the cell enabling a controlled atmosphere to be maintained. The electrochemical droplet x-ray cell works best at incident x-ray energies > 15 KeV as the x-rays lose energy penetrating the liquid droplet. Obviously the droplet is only stable when the cell is flat or has a small incidence angle, this puts limitations on the diffractometer set up.

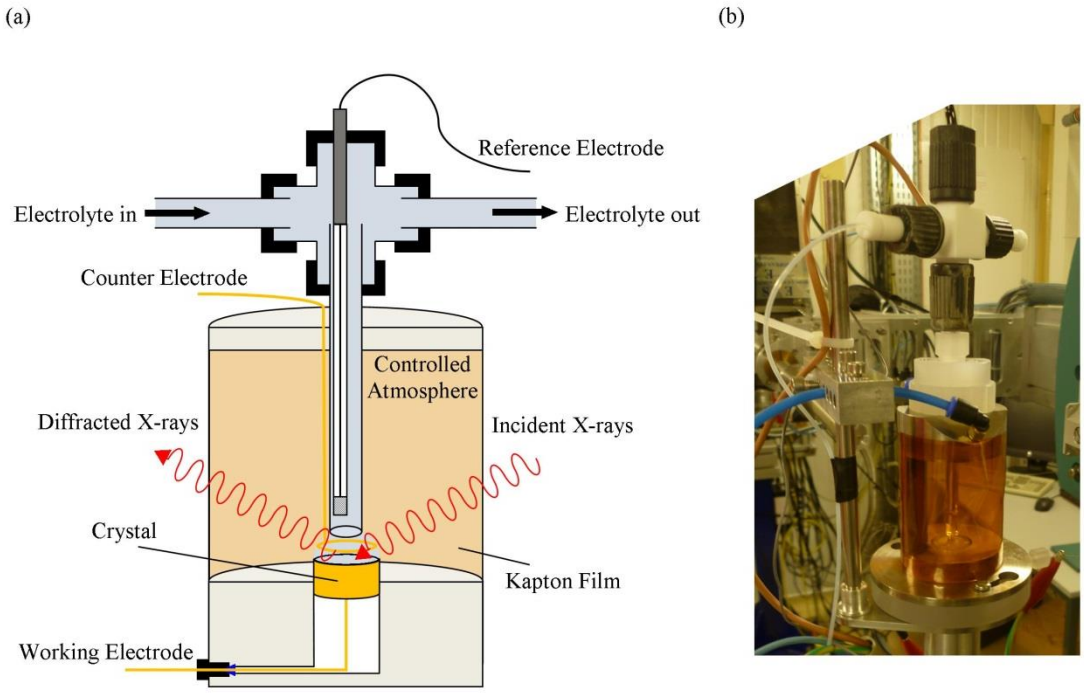

Figure 3.3 (a) schematic and (b) photograph showing electrochemical droplet x-ray cell.

3.4 X-ray Diffraction Instrumentation

3.4.1 Synchrotron Radiation

Synchrotrons dedicated to the production of x-rays have been built since the 1970s, exploiting the fact that high energy x-rays are emitted by relativistic electrons travelling in circular orbits [2, 3]. In the decades that followed synchrotron technology has evolved, the flux and more importantly the brilliance (flux / source size / source divergence) has been dramatically increased and insertion devices have been developed to take advantage of this. Today's third generation synchrotron's have a brilliance 10 orders of magnitude larger than standard laboratory sources. It is the high brilliance that makes synchrotron x-ray beams perfect for surface diffraction experiments, as it is possible to measure the diffracted intensity from just a few atomic layer of the surface of a crystal – i.e. measure CTR's [4].

In typical third generation synchrotron electrons produced by an electron gun are accelerated by a linear accelerator (linac) and then a booster synchrotron up to a GeV energy range before being transferred into the storage ring. The storage ring consists of bending magnets, used to control the path of the beam, insertion devices, present in straight sections and used to produce high intensity x-rays, RF (radiofrequency) cavities, which resupply the energy emitted as x-rays, and many focusing magnets, to maintain the ideal orbital path of the electrons.

Insertion devices consist of arrays of magnets with alternating polarity, which force the electrons to oscillate in the horizontal plane. At each bend radiation is emitted which combines with the radiation emitted from the other bends producing a more brilliant beam than from a single magnet. There are two types of insertion device wigglers and undulators. Wigglers work as just described and produce a broad continuous spectrum of x-rays. Undulators have the added feature that the magnets are spaced such that the radiation emitted from one magnet is in phase with the radiation from the rest. This coherent interference is tunable and results

in a highly collimated beam over a narrow energy range. Bending magnets also create an x-ray beam as a side effect to their main function of steering the electrons. The beam created has a wide continuous spectrum which is less brilliant than that from an insertion device. The insertion device or bending magnet is at the start of a beamline which further defines the x-ray beam before it reaches the sample. The beamlines used for the experiments in this thesis are shown in Table 3.1 which includes details of the energy range and flux.

Beamline	**Source**	**Energy Range (keV)**	**Flux (Photons/sec)**
XMaS, BM28, ESRF, France [5]	Bending Magnet	2.4 – 15	1E12
12BM, APS, USA [6]	Bending Magnet	5 – 23	2E11
ID32, ESRF, France [7]	Undulator	2.5 – 30	1E12 at high energy 1E13 at low energy
I07, Diamond Light Source, UK [8]	Undulator	6 – 30	1E14

Table 3.1 Beamlines used for experiments in this Thesis with details of their source, energy range and flux.

3.4.2 Beamline Configuration and Diffractometers

The purpose of a beamline is to define the incident beam properties, for example the wavelength, size, focus and intensity, dependent on the experimental requirements. A simple schematic of the beamline components required is shown in Figure 3.4, although in reality there may also be further slits to define the beam and several monitors to record the beam intensity at various points. As shown in Table 3.1 the radiation emitted from a bending magnet or an undulator has a wide energy range, however it is often useful to select a single energy (wavelength) in order to produce a monochromatic x-ray beam. Rather than each beamline

working at a single fixed energy, a monochromator is used to allow the beamline to be continuously tunable over the entire energy range. The monochromator is the first main component of the beamline, it consists of two defect free crytals, such as silicon (111), and exploits Bragg's law in order to extract a monochromatic beam from the incident white beam. The next component is either a toroidal mirror or separate horizontal and vertical mirrors used to focus the beam to a small spot on the sample surface. The monochromator and mirror(s) are usually contained within an optics hutch, separate from the experimental hutch, which allows for the shutter to the experimental hutch to be closed (for changing samples, detectors, sample environment, etc.) whilst the x-ray beam is still incident on the monochromator and mirror(s). This helps to avoid drift of the beam position which can occur due to changes in the temperature of the crystals, caused by the incident beam radiation.

In the experimental hutch metal foils, made from varying thicknesses of Aluminium or other metals, are used to attenuate the beam. These are used as necessary to prevent damage to the detector caused by an intense beam. A monitor, usually an ion chamber, placed after the attenuator foils is used to record changes in the incident beam intensity. This information is used in the analysis to correct for changes in the intensity of the beam incident on the sample surface. The monitor is followed by sample slits used to define the size of incident beam and remove scatter which can add to the background noise (the order of these last two components may sometimes be switched). The beam then hits the sample which is held at the center of rotation of a diffractometer, which will be described with respect to the different beamlines used in the following pages. The diffracted beam is finally collected by a detector after travelling through further slits which remove unwanted scatter and noise.

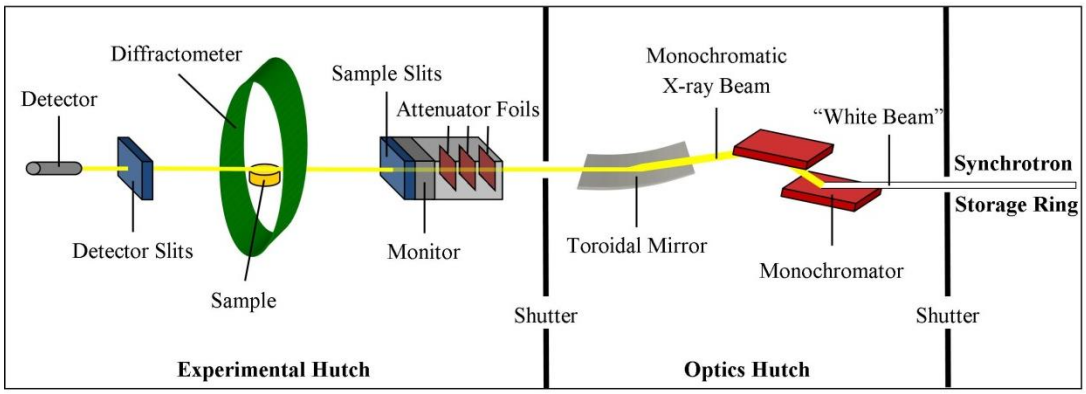

Figure 3.4 Simple schematic showing typical components of a synchrotron beamline.

One of the key differences between the beamlines detailed in Table 3.1 is the diffractometer. All diffractometers work under the same principles, changing the sample angle whilst keeping it at the center of rotation and moving the detector to record the scattered intensity from a certain crystallographic plane or position. However the exact arrangement of the diffractometer can affect how the sample is set up and the correction factors which are applied to the data prior to analysis.

The 11 axis Huber diffractometer on BM28 at the ESRF [5] and 6 circle Huber diffractometer on 12BM at the APS [6] are very similar. Both have the angles of rotation θ, ϕ, χ and 2θ with the sample mounted on a goniometer at the center of these rotations, as show in Figure 3.5. The θ and 2θ circles control the incident beam and detector angles respectively and only these two circles are required for specular diffraction defined in Chapter 2. The ϕ circle rotates the sample about the surface normal direction and the χ circle rotates the sample in the direction perpendicular to the incident beam. The set up shown in Figure 3.5 is called vertical mode, in which the detector moves vertically. The 11 axis Huber diffractometer can also work in horizontal mode, in which the detector moves horizontally and the surface normal is horizontal during specular diffraction.

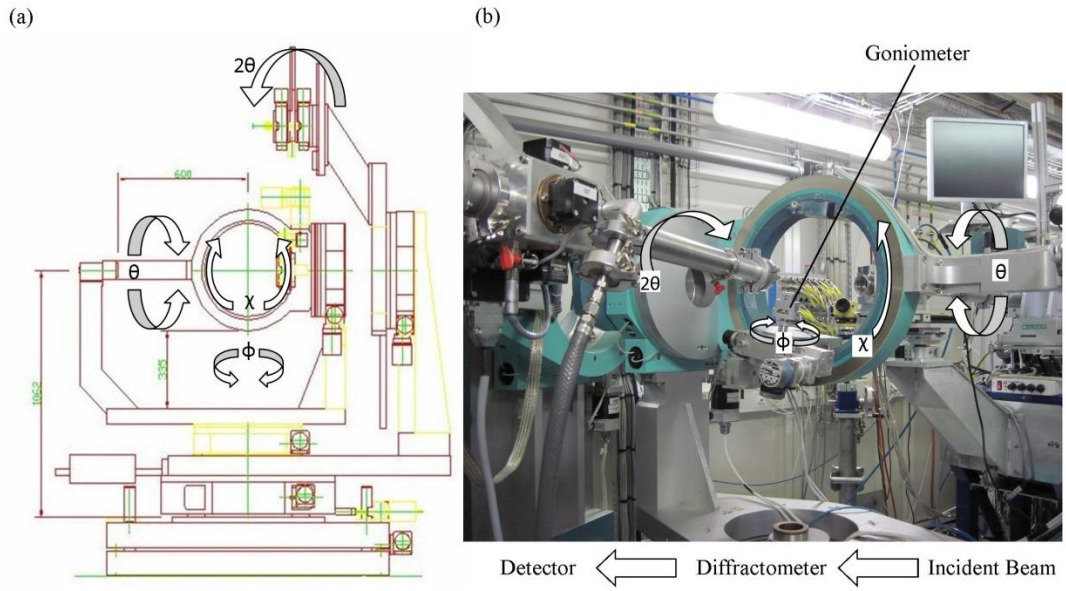

Figure 3.5 (a) schematic [5] and (b) photograph showing the 11 axis Huber diffractometer on XMaS beamline at the ESRF. The photograph shows the vertical four-circle mode of this diffractometer.

The diffractometer on beamline I07 at Diamond Light Source is a 2+3 circle diffractometer [7] together with a Hexapod on which the sample is mounted; it is used in 2+2 mode [9] for the experiments contained within this thesis (for 2+3 mode there is a ν circle for the azimuthal rotation to the detector, which remains stationary in 2+2 mode). The sample may be mounted with the surface normal horizontal or vertical. With the surface normal horizontal the angles of rotation are defined on this beamline as ω, α, γ and δ with the sample mounted at the centre of these rotations, as shown in Figure 3.6. Circles ω and α are used to change the sample position, ω rotates the sample about the surface normal direction (equivalent to ϕ) and α changes the incidence angle (equivalent to θ). The other two rotations move the detector, γ moves the detector horizontally (equivalent to 2θ) and δ moves the detector vertically. Beamline ID32 at the ESRF [8] (no longer operational) uses a 6 circle diffractometer together with a Huber tower. In z-axis geometry (used in the experiments contained within this thesis) the rotations are very similar to the ones just described.

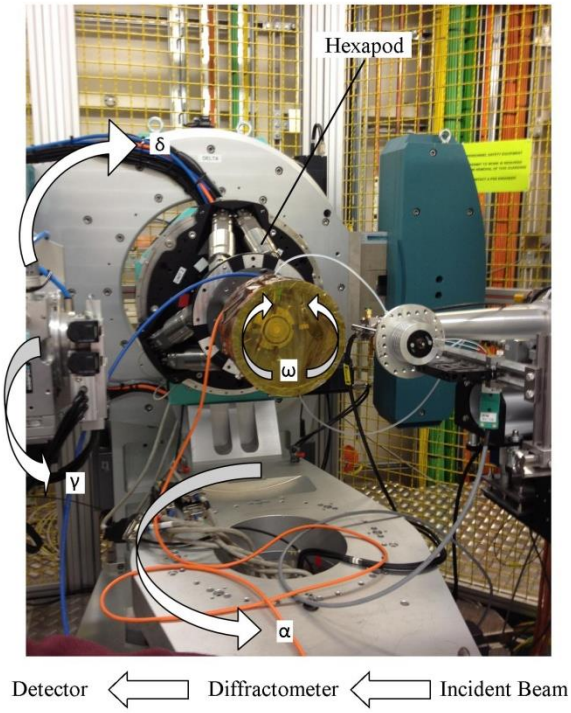

Figure 3.6 Photograph showing the 2+3 circle diffractometer on I07 beamline at Diamond Light Source. The photograph shows the sample mounted on the Hexapod with the surface normal horizontal.

3.5 Experimental Procedure

In order for the synchrotron x-ray diffraction experiment to be successful the sample must be carefully aligned on the beamline prior to measurements being made. Once the alignment has been performed it is possible to use the software on the beamline to work in the reciprocal space of the sample. A range of scans may then be used to determine the structure and behaviour of the sample. The following description is of the procedure followed at beamline BM28 (XMaS), the UK-CRG beamline at the ESRF, Grenoble, with the diffractometer in vertical mode, but a similar method can be used on other beamlines.

The first stage of the alignment process is to ensure the crystal is at the centre of the diffractometer rotations and that the beam is centred on the sample. On the first morning of the experiment the monochromator is tuned to the energy

required and the beam guided and focused to a fine spot at the centre of rotations of the diffractometer. The detector 'straight through' position is determined by scanning the detector across the beam (using attenuating filters) and the diffractometer zero positions set. A pin attached to the goniometer (or equivalent) can be used to check that all the diffractometer circles rotate around the same central point. Burn paper attached to the pin can be used to align the entire diffractometer to the beam. A telescope may be used to help check the rotations and set up to view the final central point to aid positioning of the sample. The newly prepared sample is then placed on the goniometer, moved vertically to the central point and the goniometer adjusted to ensure the sample is optically flat at all ϕ angles (either visually through the telescope or using a laser reflecting off the sample surface). After the basic visual set up has been completed, the x-ray beam is used to complete the alignment process. A process of half cutting the beam is performed with the detector in the straight through position; the sample is scanned in the z-direction through the beam and the detector counts recorded. The sample is then moved to the point at which the counts receive are half the 'straight through' value. This ensures the beam is centred on the sample.

The second stage is to define the crystallographic orientation, which is then saved using a UB matrix, enabling the creation of a reciprocal space map of the crystal sample within the software. The UB matrix requires the real space position of the diffractometer circles for two Bragg peaks with known HKL values (U) and details of the real space unit cell (B), in terms of lattice constants and angles. The first Bragg peak chosen is often a specular Bragg peak, as this requires only the diffractometer motors for θ and 2θ to be moved to the values where the Bragg peak is expected to be. The specular is independent of ϕ but may need a small adjustment of χ from 0° (surface normal vertical) to account for the miscut of the surface. The θ motor is scanned and the detector counts recorded whilst the rest of the motors are kept stationary, a technique termed a 'rocking scan', to locate the centre of the Bragg peak. The second Bragg peak needs to belong to a different set of crystallographic

planes. For a non-specular Bragg peak the diffractometer is moved to the calculated θ, χ and 2θ values. The ϕ circle is then rotated through 120° (due to the symmetry of an fcc(111) crystal) until the Bragg peak is found. Each motor is then tweaked in turn to find the exact location of the Bragg peak. To improve the accuracy of the matrix the specular Bragg peak may be swapped for another non-Specular Bragg peak. With the Bragg peak positions saved in the UB matrix the software is now set up to move the sample in reciprocal space by changing the angular positions of the circles.

Once the alignment is completed the experiment may commence. The quality of the surface is checked by moving to an anti-Bragg position and performing a θ rocking scan (for specular, ϕ rocking scan for non-specular) to check there is a clearly visible peak. If the surface preparation was unsuccessful or has deteriorated on transfer or during alignment, this scan will show only background counts without a peak due to the surface diffraction. The surface response to the applied potential can also be tested by moving to a position sensitive to changes in potential, such as a reconstruction position, performing a rocking scan to check the positioning and then performing an XRV scan (see Section 2.6) to check for an appropriate response. As long as the surface is ordered and responds to the applied potential the experiment may continue. A series of XRV measurements may be performed to confirm the stability of the surface and the response of different reciprocal space positions. In-plane structures such as a reconstructed surface layer or ordered adsorbate adlayer can be located using structure scans, in which h and/or k are scanned through a fixed position in l. If found these can be studied using XRV or rocking scans. CTR measurements may be made by performing rocking scans at increasing values of l along a CTR at a fixed potential. The intensity of each rocking scan is obtained by subtracting the background before calculating the total intensity of the scan using a numerical method or fitting a function to the lineshape. This is repeated for each rocking scan along the CTR to produce a set of

integrated intensities against l, some corrections to this data may be required prior to analysis.

3.6 Geometric Corrections

In order to compare the CTR data with the theoretical models, the raw data needs to be modified to correct for the effects on the integrated intensity of experimental conditions such as experimental geometry, sample size, beam size and detector slit settings. Changes during measurements, such as variations in the beam footprint on the sample surface as a function of incident angle, can artificially suppress or enhance the intensity along the CTR. The precise correction factors which need to be applied depend on the type of diffractometer used, its mode and even the type of scan performed – i.e. which diffractometer circle is moving during the scan. The corrections are summarised as follows: The Lorentz factor (L) accounts for the change in integration volume when converting between real and reciprocal space. The polarisation factor (P) accounts for the beam being polarised in the horizontal plane and therefore depends on whether the experiment is performed in a horizontal or vertical mode. The rod interception correction factor (C_{rod}) accounts for the amount of rod that is intercepted as a function of the outgoing angle. The finite in-plane detector acceptance correction factor (C_{det}) accounts for the finite angular acceptance of the detector and may be kept close to unity by having sufficiently wide detector slits. The area correction factor (C_{area}) accounts for the variation of active sample area, related to the size of the incident and detector slits (ignoring beam footprint and sample size). And finally a beam profile correction factor (C_{beam}) accounts for the previously mentioned variations in the size of the beam footprint on the sample surface with changing incident angle. This may also be kept close to unity so long as the angle of incidence is small. As previously mention these depend on the diffractometer and mode of use, and as a result are all functions of the diffractometer angles. An example of the corrections for a

sample mounted on beamline I07 (2+2 mode) at Diamond Light Source, where the diffractometer angles are ω, α, γ and δ, for a set of specular scans are as follows:

Lorentz Factor:

$$L = \frac{1}{\sin 2\alpha} \tag{3.1}$$

Rod Interception Correction Factor:

$$C_{rod} = \frac{\cos\alpha}{\sin^2(\alpha-\gamma)\cos\delta + \cos\alpha\cos(\alpha-\gamma)} \tag{3.2}$$

Area Correction Factor:

$$C_{area} = \frac{\cos(\beta_{out})}{\sin\delta} = \frac{\cos(\arcsin(\cos\delta\sin(\gamma-\alpha)))}{\sin\delta} \tag{3.3}$$

Polarisation Factor:

$$P = p_h P_{hor} + (1-p_h)P_{ver} \tag{3.4}$$

where

$$P_{hor} = 1 - (\sin\gamma\cos\delta)^2 \tag{3.5}$$

and

$$P_{ver} = 1 - \sin^2\delta \tag{3.6}$$

Where p_h is the horizontal polarization faction, P_{hor} is the horizontal polarisation component and P_{ver} the vertical polarisation component. Since for synchrotron experiments the polarisation is almost completely horizontal the vertical component can be neglected giving:

$$P = 1 - (\sin\gamma\cos\delta)^2 \tag{3.7}$$

Full details of the corrections factors for different diffractometer types, modes and scans can be found in references [9-12].

3.7 Analysis

The CTR data is analysed using the theory described in Chapter 2 and a best fit to the data is obtained using a least-squares method in which the variables are the structural parameters of the surface atomic layer(s). The structural parameters are; the occupation of the surface layer relative to the bulk, θ_n, which is included simply as a fraction (from 0 to 1 ML), the Debye-Waller factor, DW_n, which may differ from the bulk due to differences in the interatomic bond strengths in the near surface region, and finally the surface relaxation, ϵ_n which represents the displacement of the surface layer along the surface normal direction. The 3 topmost layers of the Au(111) surface are included in the model. Additional commensurate layers such as Ag (up to 3 layers) or incommensurate layers such as OH^- may also be included as appropriate, again the structural variables are θ_n, DW_n and ϵ_n. Additionally a parameter to account for changes in the thickness of the liquid layer over the crystal surface is included via an absorption factor in the model.

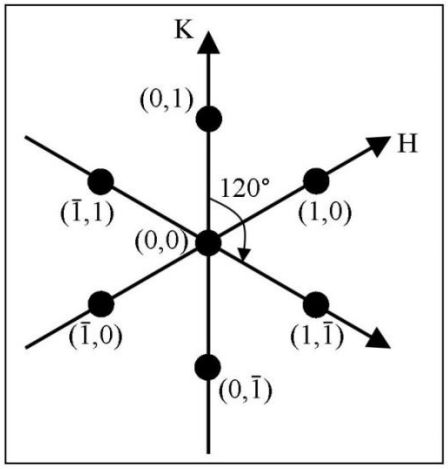

Figure 3.7: (111) reciprocal lattice at an arbitrary fixed value of l. The $(0,1,l)$, $(1,\bar{1},l)$ and $(\bar{1},0,l)$ CTR's are equivalent (as are the $(1,0,l)$, $(0,\bar{1},l)$and $(\bar{1},1,l)$) due to the 120° symmetry of the crystal. The deduced error on a CTR data point is taken from the variance in intensity of symmetry equivalent reflections.

The error on a CTR data point may be due to systematic errors from sources, such as a small misalignment sampling over different areas of the sample, or due to statistical errors, for example when the signal to noise ratio is poor at an anti-Bragg position. The systematic errors have been quantified from the variation in intensity of several symmetry equivalent positions and found to be around 10%. For the case of the (111) reciprocal lattice, at a fixed arbitrary value of l ($l = 0.2$) the positions $(0, 1, 0.2)$, $(1, \bar{1}, 0.2)$ and $(\bar{1}, 0, 0.2)$ are all equivalent due to the 120° symmetry of the crystal, as illustrated in Figure 3.7. Usually the systematic error dominates over any statistical errors, however due to issues with beam stability on initial experiments at beamline I07, the statistical error was more significant for some scans.

The in-plane structure of a surface or adlayer can be probed using scans along the [H, K] direction. When a structure peak is found, a rocking scan may be used to determine the exact position of the scattering in reciprocal space. From the rocking scan the domain size, ξ, of the structure can be calculated using the equation:

$$\xi = \frac{a_0}{4\pi\sigma}$$

where a_0 is the lattice constant of the substrate (used to set up the UB matrix) and σ is the full width half maxima (FWHM) of the peak determined by fitting an appropriate line-shape to the rocking scan.

The XRV data are background subtracted and normalised so that a comparable relative change in intensity at a fixed reciprocal space position may be obtained. Since different reciprocal space positions are sensitive to different changes at the surface of the electrode, such as in-plane ordering, adlayer structures, surface relaxations and surface reconstructions, the XRV scans are used to better understand these surface changes as a function of applied potential and correlate them to the structural parameters analytically obtained from the CTR data.

3.8 References

[1] MaTecK, Metal Single Crystals, http://www.mateck.com/index.php?option=com_content&view=article&id=6&Itemid=7, 2013.
[2] J. Als-Nielsen, Elements of Modern X-Ray Physics, Wiley, New York, (2001).
[3] A.C. Thompson, X-ray Data Booklet, 3rd ed., Lawrence Berkeley National Laboratory California, (2009).
[4] D.D. Fong, C.A. Lucas, M.I. Richard, M.F. Toney, Mrs Bull, 35 (2010) 504-513.
[5] XMaS, XMaS The UK Material Science Beamline at the ESRF: Beamline Description, http://www2.warwick.ac.uk/fac/cross_fac/xmas/description/, 2013.
[6] APS, Beamline 12-BM-B: Sector 12 Bending Magnet Beamline, http://www.aps.anl.gov/Beamlines/Directory/showbeamline.php?beamline_id=18, accessed 2013.
[7] ESRF, ID32 Surface XRD, SEXAFS and X-ray Standing Waves: Beamline: Source Characteristics, http://www.esrf.eu/UsersAndScience/Experiments/StructMaterials/ID32/Beamline/XraySource.html, 2008.
[8] Diamond, I07: Surface and Interface Diffraction: Beamline guide, http://www.diamond.ac.uk/Home/Beamlines/I07/beamline.html, 2012.
[9] E. Vlieg, J Appl Crystallogr, 31 (1998) 198-203.

Chapter 4:

The Au(111) Single Crystal

4.1 Introduction

The Au(111) surface and other Au single crystal surfaces are model systems for investigating and understanding general surface processes such as surface reconstruction [1, 2], adsorption of ordered adlayers [3], self assembly [4, 5] and electrocatalytic reactions [6]. Au single crystal electrodes have has also been commonly used for electrodeposition experiments [7-10]. Due to the inert nature of Au, alterations to the Au electrode surface following brief exposure to air are fairly minimal, this is especially true for Au(111) surface which may be exposed to the ambient environment for 15 minutes after flame annealing before transferring to the electrochemical environment. As a consequence, as long as the Au(111) crystal is carefully prepared so that the surface structure is well defined, prior to being transferred to an electrochemical environment, the surface structure should (under the right electrochemical conditions) remain well ordered for a long period of time (days). This makes it a very suitable substrate for surface x-ray scattering

(SXS) experiments. The Au(111) surface is the most densely packed of the low index faces, however it has been studied extensively in UHV [11-13] and electrolyte [1, 2, 14], and has been found to reconstruct (an in-plane reordering of the top most atomic layer) in both environments to a phase denser than the bulk (111) planes.

All experiments detailed within this thesis use the Au(111) single crystal as the substrate on which the supported metal multilayers are formed. This chapter is intended as a overview of the Au(111) surface and its reconstruction. First the Au(111) reconstruction in UHV and electrolyte will be introduced. Cyclic voltammetry (CV) for the Au(111) electrode in 0.1 M KOH is described. In-situ experimental SXS results are presented for Au(111) in 0.1 M KOH and the results commented on with respect to the reconstruction. The figures contained within the chapter are also a useful reference for the comparison with the supported metal multilayer experiments detailed in this Thesis.

4.2 Au(111) Reconstruction

For many single crystals the structure of the surface atoms is different from that of the bulk. This is due to the forces on atoms at the surface being imbalanced compared to those on atoms in the bulk. To account for this the surface atoms often undergo a lateral displacement in order to lower the surface energy. This surface phenomenon, termed the surface reconstruction, results in a different structure for the outermost atomic layer than the bulk. The three low index surfaces of Au (Au(100), Au(110) and Au(111)) all undergo reconstruction in UHV and electrochemical environments [14]. In UHV, at room temperature, the Au(111) surface is found to be reconstructed to a (23 x √3) phase [11]. This reconstructed surface has been observed to transition back to unreconstructed Au(111) (1 x 1) surface (termed lifting) by the adsorption of atoms or molecules [14]. Preparation of an Au(111) using the flame annealing process described in Chapter 3 produces the same reconstructed surface as that found in UHV [7, 14].

A similar reconstruction is present in the electrochemical environment, however the unit cell may be larger and the reconstruction is then termed (p x √3) where 23 < p < 30. In an electrochemical environment the surface can be transitioned between the reconstructed (p x √3) phase and the unreconstructed (1 x 1) surface by changing the electrode potential. The reconstructed surface has been observed in many aqueous electrolytes using in-situ techniques such as SXS and STM. The potential at which the reconstruction occurs depends significantly on the anions present in the electrolyte. The reconstruction forms at potentials where no specifically adsorbed anions are present on the surface and lifted upon specific adsorption of anions. The formation of the reconstruction usually occurs at potentials negative of the potential of zero charge (*pzc*, the potential at which no excess charge is on the electrode surface) but precisely how negative of the *pzc* depends on the electrolyte. Lifting of the reconstruction usually requires a potential slightly positive of that required for the formation of the reconstruction. The transition to the (1 x 1) phase is much faster than the formation of the reconstructed phase. Adsorbed species such as carbon monoxide (CO) shift the potential at which the reconstruction forms [1, 2, 6, 7, 14-18].

The unit cell of the (23 x √3) reconstructed surface is shown schematically Figure 4.1 together with the unreconstructed (1 x 1) surface for comparison. The (23 x √3) reconstructed surface layer is compressed along one of the three [100] directions such that there are 24 surface atoms in place of 23. The stacking sequence of the surface layer oscillates between C and A sites along the [100] (or equivalent) direction. The resulting reconstructed surface has a factor of 1.043 increase in density compared to the Au(111) (1 x 1) surface [1, 2, 11, 14]. Upon lifting the reconstruction excess atoms form monoatomic high Au islands on the Au(111) (1 x 1) surface. Reconstruction domains created due to the three possible [100] directions of the reconstructed surface result in a superstructure with a herringbone pattern, which is formed as a result of regular alternation between two of the three reconstruction direction. The “elbows” of the herringbone

superstructure act as preferential nucleation centres for metal overlayers such as Ni and Co [7, 14, 19, 20]. A series of in situ STM images performed by O. M. Magnussen et al. are presented in Figure 4.2 [21] showing the Au(111) herringbone superstructure during the onset of Ni deposition.

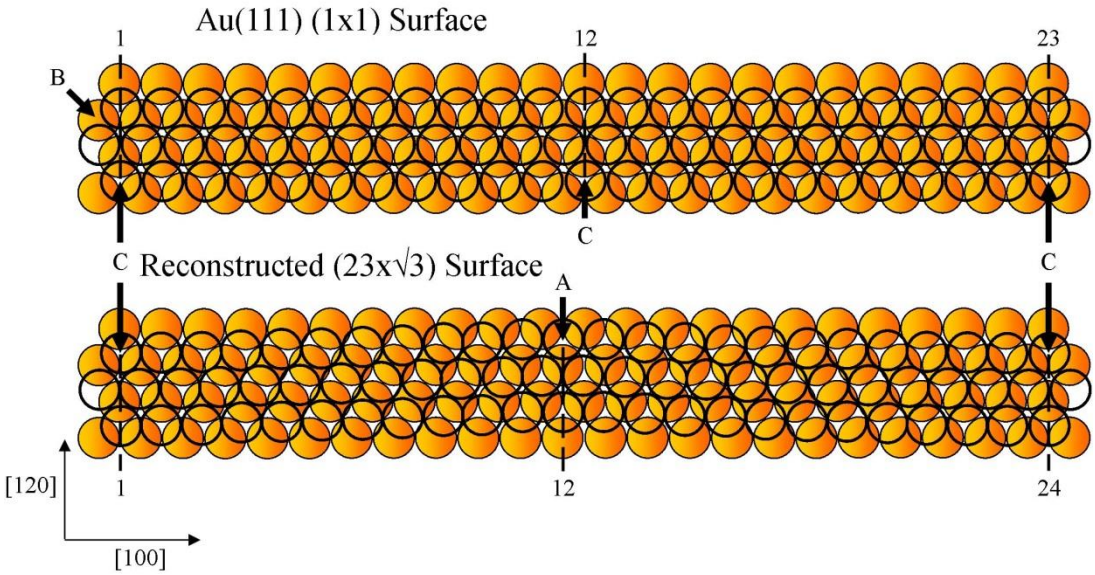

Figure 4.1 Schematic real space model for the Au(111) unreconstructed (1x1) surface (top half) and reconstructed (23 x √3) surface (bottom half). The filled orange circles correspond to the atoms in the second layer and the open circles correspond to the surface atoms. The stacking sites are indicated. On the Au(111) (1x1) surface the second layer are in B sites and the surface atoms are in C sites (a third layer would be in A sites). The reconstructed surface is compressed such that there are 24 atoms in place of 23 underlying bulk atoms along the [100] direction. The surface atoms on the left and right-hand sides are in undistorted hexagonal sites (C), whereas the atoms in the centre of the figure are in faulted sites (A).

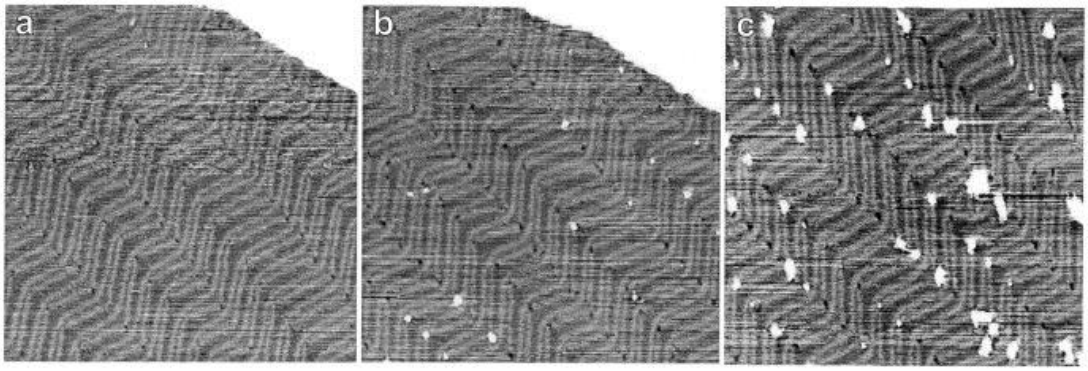

Figure 4.2 A series of in situ STM images for Ni growth on reconstructed Au(111) in 10^{-2} M H_3BO_3 + 10^{-4} M HCl + 10^{-3} M $NiSO_4$ (a) directly after decreasing the potential from -0.2 to -0.6 V (the onset Ni deposition), (b) after 3 min at -0.6 V, and (c) after 20 min at -0.6 V (vs Ag/AgCl). Slow nucleation and growth of Ni adlayer islands at the elbows of the Au reconstruction is visible (1050 x 1050 $Å^2$). The nanosized Ni islands result from nucleation driven by place exchange at elbows of the (23 x √3) surface reconstruction. Reprinted from the Journal of Electroanalytical Chemistry, 467, O.M. Magnussen, R.J. Behm, Structure and growth in metal epitaxy on low-index Au surfaces – a comparison between solid-electrolyte and solid-vacuum interfaces, 258-269, Copyright (1999), with permission from Elsevier. [21]

4.3 Au(111) in 0.1M KOH

4.2.1 Electrochemistry in 0.1M KOH

Previous in-situ studies of Au(111) electrode in 0.1M KOH have identified the potentials at which the Au(111) surface reconstruction forms and lifts [6, 18]. Figure 4.3 show the CV for Au(111) surface in 0.1 M KOH [18]. The region denoted "Pure Capacitance" corresponds to that of charging/discharging of the double layer. The second region denoted "Reversible Oxide" corresponds to the adsorption OH_{ad}, with the scatter line showing the related change in OH surface coverage. Finally the third region denoted "Irreversible Oxide" consists of two stages, the first (E > 1 V vs RHE – reversible hydrogen electrode) is a phase transition triggered by additional OH adsorption the second (E > 1.3 V) is responsible for the formation of irreversible oxide. The reconstruction forms at potentials negative of -0.25 ± 0.1 V (vs SCE – saturated calomel electrode, ≅ -0.2 V

vs Ag/AgCl and ≅ +1.2 V vs RHE) and lifts at potentials positive of -0.10 ± 0.1 V (vs SCE, ≅ -0.05 V vs Ag/AgCl and ≅ +1.05 V vs RHE) [6].

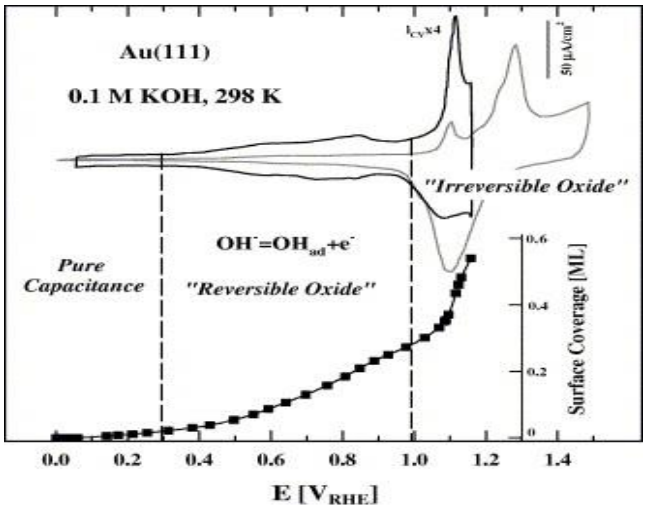

Figure 4.3 Cyclic voltammetry of Au(111) in 0.1 KOH over range 0 – 1.5 V (gray line) and 0 – 1.2 V (black line - which has been x4 magnified to show greater detail). The adsorption isotherm E versus surface coverage of OH_{ad} (scatter + line curve). Reprinted from Surface Science, 582, Gallagher, M. E. et al., Structure sensitivity of CO oxidation on gold single crystal surfaces in alkaline solution: Surface X-ray scattering and rotating disk, 215-226, Copyright (2005), with permission from Elsevier. [18]

Figure 4.4 shows an example of the CV taken for the Au(111) single crystal in 0.1M KOH. Cathodic peak C1 is due to the hydrogen evolution reaction. Anodic peak A1 is due to a phase transition triggered by additional OH adsorption, A2 is due to irreversible oxide formation and C2 is due to oxide reduction. The CV is very similar to that from the literature shown by the grey line in Figure 4.3. These features are all well defined which confirms that the Au(111) surface is of high quality, clean of unwanted adsorbates and well ordered. The experiments performed in 0.1 M KOH in Chapters 5 and 7 were restrained to within the potential range -0.1 V to -1.0 V (vs Ag/AgCl) to ensure no irreversible oxides were formed, whilst being able to study OH adsorption and investigate any reconstruction of the Au(111) surface.

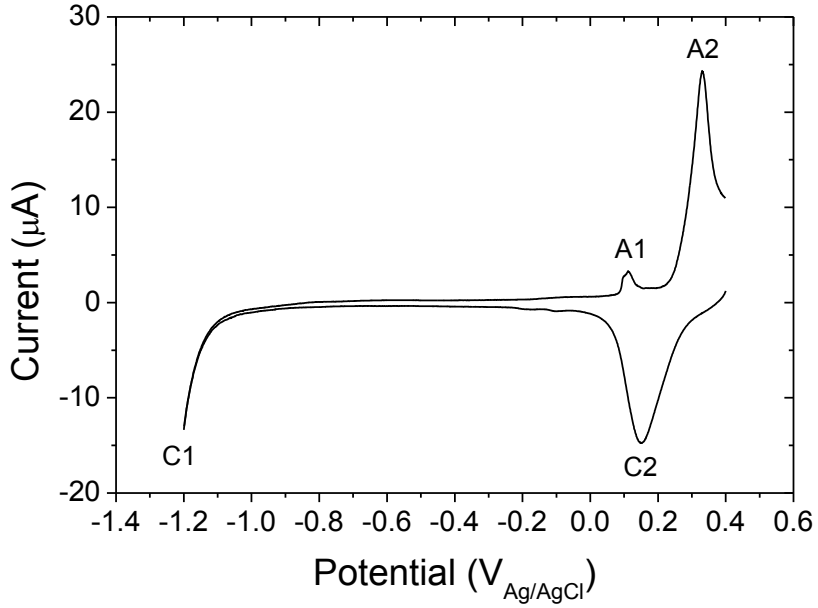

Figure 4.4 Cyclic voltammetry of the Au(111) surface in 0.1 M KOH at a sweep rate of 20 mV/s vs Ag/AgCl.

4.2.2 SXS studies of the Au(111) Reconstruction

SXS measurements were performed on a Au(111) in 0.1M KOH. The crystal was prepared by flame annealing and transferred into a thin-layer cell with a N_2 atmosphere as described in Chapter 3. Prior to each experiment, the potential was cycled for ~30 minutes in the alkaline electrolyte, over the range 0.25-1.2 V (at 50 mV/sec) and then held at 0.25 V. This was to ensure reproducible surface preparation ('surface conditioning') in each case. X-ray measurements were performed on beamline BM28 (XMaS), the UK-CRG beamline at the ESRF, Grenoble using focused incident x-rays of energy 11 keV. The reference electrode used in the x-ray cell was Ag/AgCl but quoted vs RHE. For the SXS measurements the electrode potential was restricted to between 0.0 V to 0.7 V (vs RHE) to ensure that no potential-induced lifting of the reconstruction occurs.

For the Au(111) surface, the (p x $\sqrt{3}$) reconstruction gives rise to a well-defined diffraction pattern which, in the surface plane of reciprocal space, is characterised by a hexagon of additional diffraction spots around the scattering that occurs for

the bulk Au(111) crystal. This is schematically illustrated in Figure 4.5, which shows a detailed map of the scattering that occurs in reciprocal space around the (h, k) positions. Figure 4.6 shows the scattered intensity measured along the [1, 1, 0] direction through the (0, 1, 0.3) reciprocal lattice point (indicated by the blue arrow in Figure 4.5) for two potentials of 0.7 V and 0.25 V (vs RHE). In each scan shown, two clear peaks can be seen, the one at H,K = 0 corresponding to the scattering from the (0, 1, L) CTR and the peak at H,K ~ 0.02 which arises due to the (p x √3) reconstruction. The surface is reconstructed at both potentials, but the size of the unit cell (p x √3) varies as a function of applied potential [1], which causes a shift in the position of the peak at H,K ~ 0.02 shown in Figure 4.6. A detailed characterisation of the changes in the surface reconstruction can be obtained from the [H, K] scans shown in Figure 4.6. The position of the reconstruction peak is directly related to the periodicity of the reconstruction defined by the value of p, the stripe separation, which defines the unit cell (p x √3). The value of the stripe separation is determined from p = 1 / (2ΔH), where ΔH is the separation from the CTR position (at H = 0), to the position of the reconstruction peak projected onto the H position [1, 22]. Fits of a double Lorentzian lineshape to the data shown in Figure 4.6 enable both the value of p and the domain size, ξ, to be obtained for each potential. The Lorentzian lineshape is derived from a 1D real space atomic model in which ξ decays exponentially with a length $\xi = a_0/(4\pi\sigma)$, where a_0 is the lattice constant of Au, 4.078 Å, and σ is the full width half maximum (FWHM) of the peak in Figure 4.6 in units of H. It should be noted that the lineshape can be affected by substrate mosaic effects which have a Gaussian component and, additionally, can have an asymmetry caused by a distribution of domains with a range of p values. These effects are not included in the Lorentzian model, however, the essential structural information can be extracted from the analysis. From Figure 4.6 values of p are found to be p = 25.3 ± 0.3 at 0.25 V and p = 24.3 ± 0.3 at 0.7 V.

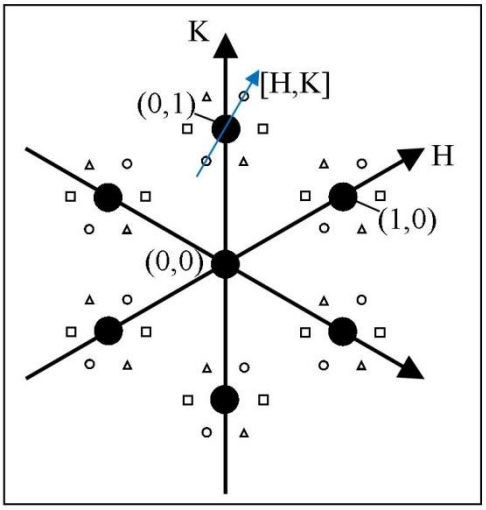

Figure 4.5 In-plane diffraction pattern for the (23 x √3) reconstruction. The solid circles correspond to the scattering from the bulk Au(111). The open symbols are from the (23 x √3) reconstructed phase with three rotationally equivalent domains.

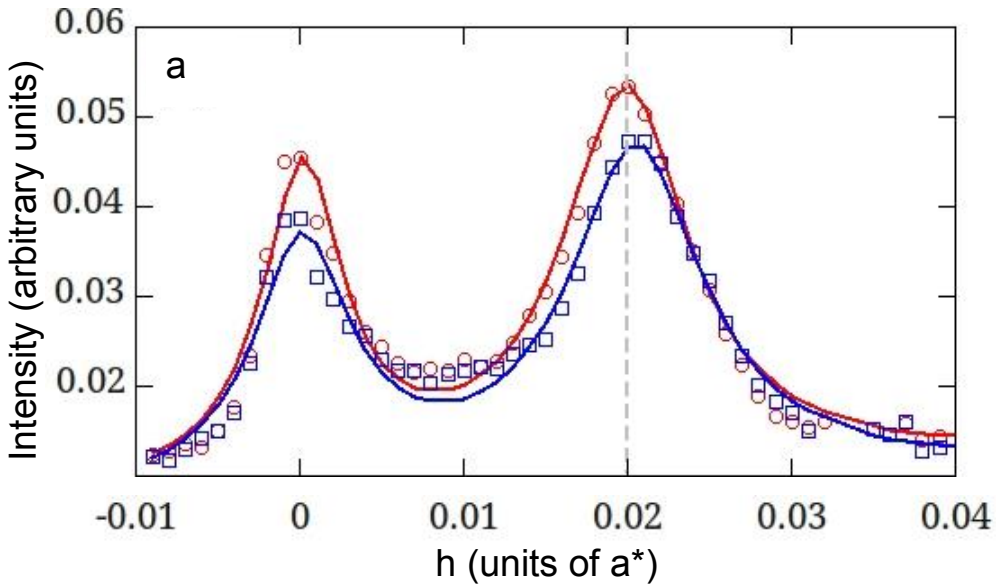

Figure 4.6 In plane x-ray diffraction from the reconstructed Au(111) surface in 0.1 M KOH. Measured along the [1, 1, 0] direction at 0.7 V (blue) and 0.25 V (red) (vs RHE). The data is fitted with a double Lorentzian line profile (see text for details). The dashed vertical line indicates the peak position measured at 0.25 V.

4.2.3 X-ray Voltammetry in 0.1M KOH

X-ray voltammetry (XRV) measurements made at positions along the (0, 0, L) CTR and at the (1, 0, 3.7) position at a scan rate of 5 mV/s are shown in Figure 4.7. The intensity at the specular anti-Bragg position, (0, 0, 1.52), is sensitive to ordering in the electrode surface and electrolyte side of the interface. The intensity here increases as adsorbed OH is removed from the surface and the reconstruction is formed. The positions (0, 0, 2.7) and (0, 0, 3.3) are either side of the specular Bragg peak and the intensity at these positions is sensitive to surface relaxation [23, 24]. These two positions mirror each other, an increase in intensity at (0, 0, 2.7) (decrease in intensity at (0, 0, 3.3)) corresponds to an expansion of the surface. The position (1, 0, 3.7) is close to a non-specular Bragg peak and changes in intensity here are sensitive to expansions of interfacial atomic positions that are commensurate with the Au lattice. This position is also sensitive to the reconstruction, but since the reconstructed surface is incommensurate with the bulk the intensity falls as the reconstruction is formed. The formation of the reconstruction is not immediate and may take minutes to complete [14], hence there is some hysteresis in the structurally sensitive XRV scans.

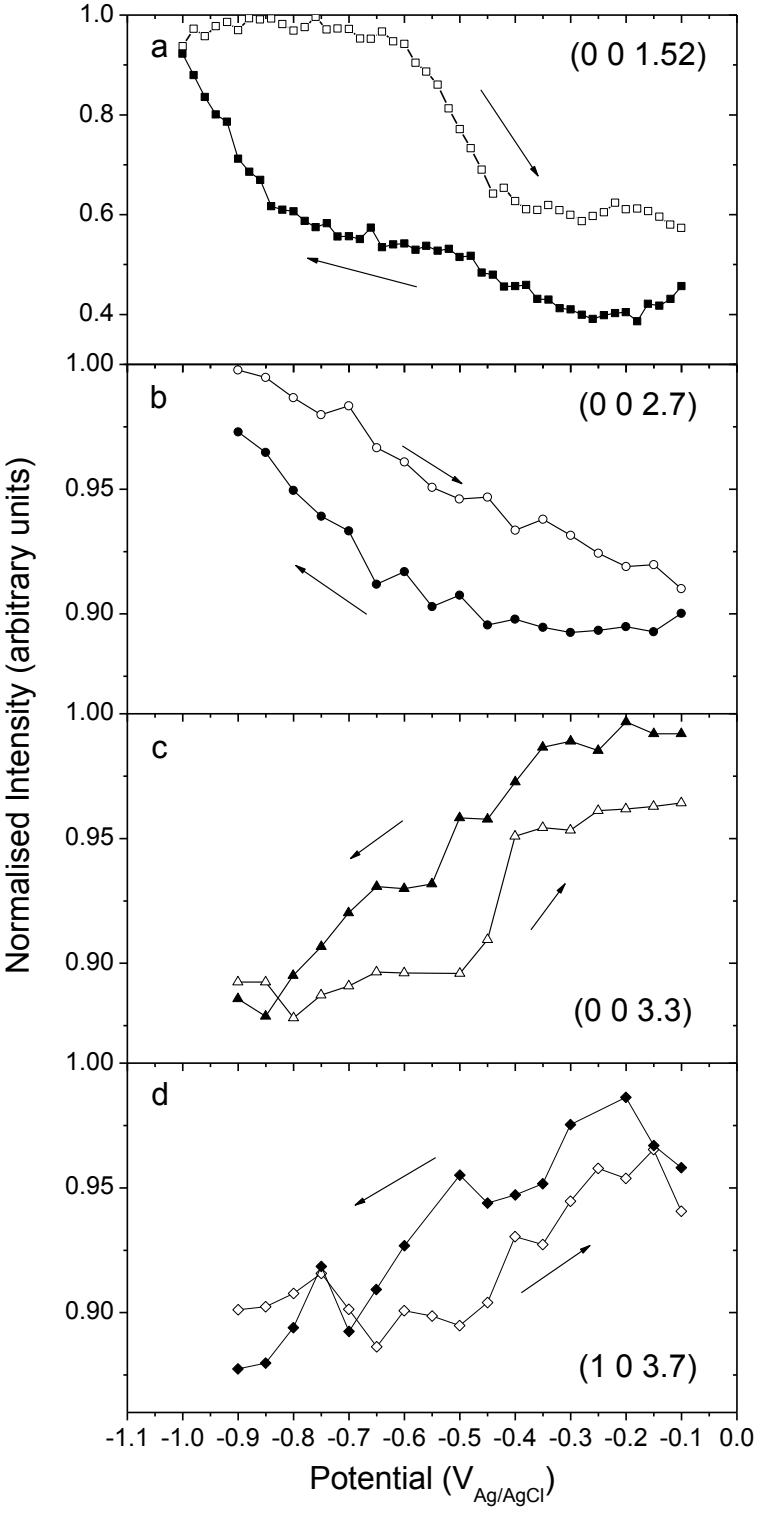

Figure 4.7 X-ray voltammetry for Au(111) in 0.1 M KOH taken at reciprocal space positions (0, 0, 1.52), (0, 0, 2.7), (0, 0, 3.3) and (1, 0, 3.7) at a scan rate of 5 mV/s.

4.2.4 CTR of the Reconstructed Surface

Figure 4.8 shows the specular CTR data measured at 0.7 V in 0.1 M KOH. The solid line is a fit to the data according to a simple model. In the model the surface density of the topmost Au layer was fixed according to the values obtained from the p value (p=24) and an additional oxygen layer was included to represent possible ordering of the water on the electrolyte side of the interface. The surface relaxation of the topmost Au layer, ε_{Au} (expressed as a percentage of the Au(111) lattice spacing, 2.354 Å), the Au-O distance (for ordering in the water), $d_{Au\text{-}O}$, the coverage, θ_O and an *rms* roughness for the surface Au layer, σ_{Au}, were allowed to vary in order to fit the data. The calculated best fit (solid line) yielded the following parameters; θ_O = 0.5 ± 0.4, $d_{Au\text{-}O}$ = 3.4 ± 0.4 Å, ε_{Au} = +3.2 ± 0.8% (the positive sign indicating an outward expansion of the surface atomic layer), σ_{Au} = 0.16 ± 0.02 Å (the *rms* roughness for the oxygen layer was fixed at 0.1 Å as this parameter can be coupled to the coverage, θ_O, during the least-squares fit). The results are in excellent agreement with previous SXS studies of the Au(111) surface reconstruction in electrolyte [1] and the surface relaxation of the topmost Au layer also agrees with results obtained for the reconstructed surface under UHV conditions [11].

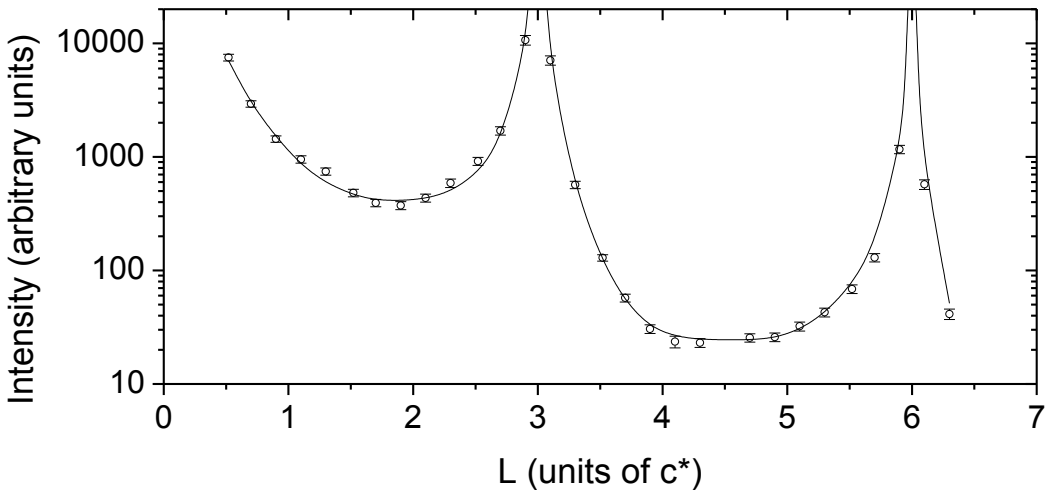

Figure 4.8 CTR The specular CTR data measured at 0.7 V (vs RHE). The solid line is a best fit to the data according to the simple structural model described in the text.

4.4 References

[1] J. Wang, B.M. Ocko, A.J. Davenport, H.S. Isaacs, Phys Rev B, 46 (1992) 10321-10338.
[2] D.M. Kolb, J. Schneider, Electrochim Acta, 31 (1986) 929-936.
[3] O.M. Magnussen, J. Hagebock, J. Hotlos, R.J. Behm, Faraday Discuss, 94 (1992) 329-338.
[4] M. Schweizer, D.M. Kolb, J Electroanal Chem, 564 (2004) 85-91.
[5] J. Bjork, F. Hanke, S. Stafstrom, J Am Chem Soc, 135 (2013) 5768-5775.
[6] I.M. Tidswell, N.M. Markovic, P.N. Ross, Surf Sci, 317 (1994) 241-252.
[7] P. Allongue, F. Maroun, J Phys-Condens Mat, 18 (2006) S97-S114.
[8] P. Allongue, F. Maroun, Mrs Bull, 35 (2010) 761-770.
[9] E. Herrero, S. Glazier, H.D. Abruna, J Phys Chem B, 102 (1998) 9825-9833.
[10] S. Garcia, D. Salinas, C. Mayer, E. Schmidt, G. Staikov, W.J. Lorenz, Electrochim Acta, 43 (1998) 3007-3019.
[11] A.R. Sandy, S.G.J. Mochrie, D.M. Zehner, K.G. Huang, D. Gibbs, Phys Rev B, 43 (1991) 4667-4687.
[12] C. Woll, S. Chiang, R.J. Wilson, P.H. Lippel, Phys Rev B, 39 (1989) 7988-7991.
[13] U. Harten, A.M. Lahee, J.P. Toennies, C. Woll, Phys Rev Lett, 54 (1985) 2619-2622.
[14] D.M. Kolb, Prog Surf Sci, 51 (1996) 109-173.
[15] J. Wang, A.J. Davenport, H.S. Isaacs, B.M. Ocko, Science, 255 (1992) 1416-1418.
[16] B.M. Ocko, O.M. Magnussen, R.R. Adzic, J.X. Wang, Z. Shi, J. Lipkowski, J Electroanal Chem, 376 (1994) 35-39.
[17] T. Kondo, J. Morita, K. Hanaoka, S. Takakusagi, K. Tamura, M. Takahasi, J. Mizuki, K. Uosaki, J Phys Chem C, 111 (2007) 13197-13204.
[18] M.E. Gallagher, B.B. Blizanac, C.A. Lucas, P.N. Ross, N.M. Markovic, Surf Sci, 582 (2005) 215-226.
[19] S. Narasimhan, D. Vanderbilt, Phys Rev Lett, 69 (1992) 1564-1567.
[20] P. Allongue, F. Maroun, Curr Opin Solid St M, 10 (2006) 173-181.
[21] O.M. Magnussen, R.J. Behm, J Electroanal Chem, 467 (1999) 258-269.
[22] O.M. Magnussen, K. Krug, A.H. Ayyad, J. Stettner, Electrochim Acta, 53 (2008) 3449-3458.
[23] R.J. Nichols, T. Nouar, C.A. Lucas, W. Haiss, W.A. Hofer, Surf Sci, 513 (2002) 263-271.
[24] C.A. Lucas, Electrochim Acta, 47 (2002) 3065-3074.

Chapter 5:

The Structure and Stability of Ag on Au(111) in Alkaline Electrolyte

5.1 Introduction

The adsorption of oxygen and hydroxide species onto metal surfaces is key to understanding surface reactivity and catalytic behavior, both in the high pressure gas environment and at the electrochemical interface. In an electrochemical environment, while there has been widespread study of multilayer oxide growth on Ag electrode surfaces [1, 2], there has been less study of underpotential oxidation, in spite of the fact that this is the potential region of the oxygen reduction reaction [3]. This is mainly due to the difficulty in obtaining atomic-scale structural information from a reactive surface in the liquid environment. OH^- adsorption is of particular interest as it is involved in many surface reactions such as oxidation/reduction. It is also the precursor state of surface oxide formation which is of fundamental importance in both electrochemical and gaseous environments

as it is the oxide surface that plays the key role in many catalytic applications [4] and is the first stage of the corrosive process.

By forming supported metal multilayers we are able to separate surface effects from bulk properties. The formation and properties of supported metal multilayers on a metallic substrate and core-shell nanoparticles, in which the surface atomic layer is a different element to the core, is of great interest as the surface metal can greatly affect the properties and reactivity of the material [5-8]. Much research has been done on the underpotential deposition (UPD) of Ag on Au(111) [9-12] and the synthesis of gold-silver core-shell nanoparticles [13-16], the latter have been found to have enhanced antibacterial activity [17] and improve the catalytic reduction of 4-nitrophenol by $NaBH_4$ (sodium borohydride) in water [18].

The term underpotential deposition (UPD) refers to the deposition of metal monolayer(s) on a foreign metal substrate, for example copper on to Au(111), at potentials positive of that predicted by the Nernst equation for bulk deposition [10, 19-21]. The violation of the Nernst equation is permitted when the adatom-substrate interaction is stronger than that between the adatoms. As a result, usually only the first monolayer may be formed through UPD, however in the unusual case of Ag on Au(111) up to 2 monolayers maybe formed in the UPD region [9, 20]. UPD systems are of great interest as they allow precise and reproducible control of the surface coverage and structure. The nature and concentration of anions in the supporting electrolyte greatly affect the UPD process, changing the kinetics and structure of the adlayer(s) formed, and helping to stabilise the UPD monolayer(s) [10, 22-27]. This is the case for the UPD of Ag on Au(111). To fully understand the effect of the anions, the deposition of Ag on Au(111) in UHV conditions is first considered. The first Ag layer deposits as fingerlike rows locked to the Au(111) (23x√3) reconstruction [28, 29]. The growth is not layer by layer, instead the second layer commences before the first is complete [30]. This growth is due to the attractive forces between adatoms which leads to an aggregation process resulting in a close packed structure, even when the total coverage is less

than 1 monolayer. In contrast the UPD of less than 1 monolayer Ag on the Au(111) surface produces open structures [31-36]. However a series of first-principle calculations by Sanchez *et al*. found that no structure more expanded that the (1x1) compact monolayer is more stable than the bulk silver phase and hence should not be deposited [37]. An assumption in their calculation was that the structure of the double layer remains unchanged upon adsorption of Ag on the Au(111) surface, but their results for the change in the work function indicate that this condition is not fulfilled. The changes in the double layer may be due to three different effects: additional adsorption of anions, negative shift in the potential of zero charge (*pzc*) and effect of the electric field on the binding energy. The open structures produced in the UPD of Ag on Au(111) are dependent on the anion present; for example in sulphate the Ag UPD overlayer exhibits a (3x3) structure, in nitrate a (4x4) structure and in perchlorate another open structure [31-36]. These open structures imply that there is a repulsive effect due to the presence of the anions. As the coverage of the Ag deposit is increased in the sulphate electrolyte the structure transitions from expanded (3x3) to a close-packed pseudomorphic monolayer of Ag. STM images have revealed that before the initial Ag deposition (bi)sulphate forms an ordered (√3 x √7)R19.1° structure on the Au(111) surface, it is also suspected that sulphate is adsorbed on the Ag monolayer, but the exact nature of this is unknown [35]. On the Ag(111) surface sulphate forms an ordered (3 x 3√3) structure [38].

In this Chapter, an *in-situ* surface x-ray scattering (SXS) [39] study of the UPD of Ag on to the Au(111) electrode surface and subsequent behaviour of the Ag modified Au(111) surface in alkaline electrolyte is presented. Transferring the Ag-modified Au(111) electrode to a silver free alkaline electrolyte allows the applied potential to be altered without depositing further Ag. 0.1 M KOH was used to study the region of OH^- adsorption through SXS, cyclic voltammetry and x-ray voltammetry (XRV). Crystal truncation rod (CTR) results allow structural information of the underlying Au(111) substrate, the Ag layers and any ordering in the electrochemical double layer to be determined. Potentiodynamic XRV measurements, involving the

monitoring of x-ray diffraction at key reciprocal lattice positions as a function of potential, have been performed to determine the potential dependent structural changes induced by the deposition of Ag and subsequent adsorption of OH^- on the Ag surface. The results indicate that as well as an ordered OH^- layer in the electrolyte side on the interface there is also sub-surface OH present.

5.2 Experimental Methods

The Au(111) crystal was prepared as described in Section 3.2 and transferred to either the x-ray cell or the hanging meniscus cell depending on the experiment as shall be explained. To study the Ag deposition process the crystal was transferred to the electrochemical x-ray cell and was immersed at open circuit potential in nitrogen purged electrolyte 0.05 M H_2SO_4 + 1 mM Ag_2SO_4. To study the Ag layers in alkaline electrolyte separate electrochemical cells were used for the deposition and subsequent x-ray measurements in alkaline electrolyte. First the crystal was immersed at open circuit potential in a hanging meniscus electrochemical cell containing nitrogen purged electrolyte 0.05 M H_2SO_4 + 1 mM Ag_2SO_4 to allow precise control of the deposition of Ag layers on the Au(111) surface. Once the Ag layers were formed the crystal was transferred to the electrochemical x-ray cell with a drop of ultrapure water protecting the surface and immersed at open circuit potential into nitrogen purged alkaline electrolyte, 0.1 M KOH, in order to study the supported metal multilayers. The outer chamber of the x-ray cell was continuously purged with nitrogen to protect the surface from oxygen. The cyclic voltammetry measurements were performed in a hanging meniscus cell with the same sample preparation, nitrogen purged electrolytes and nitrogen atmosphere. The reference electrode used was leak free Ag/AgCl versus which all potentials are quoted.

X-ray measurements were performed on beamline I07, at the Diamond Light Source, Oxfordshire and on beamline ID32, at the ESRF, Grenoble using focused incident x-rays of energy 11 keV and 21.3 keV respectively. The electrochemical x-

ray cell used depends on the diffractometer and energy of the incident x-rays. The electrochemical 'thin-layer' x-ray cell was used on beamline I07, mounted on the hexapod on the (2+3)-circle diffractometer with surface normal horizontal. The electrochemical 'droplet' x-ray cell was used on beamline ID32, mounted on the Huber tower on the 6-circle diffractometer with surface normal vertical and an incidence angle of 0.6°. The experimental procedure followed that of similar studies reported previously [39, 40].

5.3 Formation of Ag Layers on Au(111) in Acid Electrolyte

There have been numerous studies of the underpotential deposition of Ag on to Au(111) [9-11]. These have shown that there are different potential regions for monolayer, bilayer and bulk deposition, hence electrochemical deposition can allow fine control of the Ag structure formed. Figure 5.1 shows the cyclic voltammetry (CV) for the Au(111) electrode in 0.05 M H_2SO_4 + 1 mM Ag_2SO_4 performed in a hanging meniscus cell at a sweep rate of 5 mV/s. The three cathodic peaks at 0.95 V (C1), 0.57 V (C2) and 0.46 V (C3) are due to the deposition of Ag. C1 and C2 are responsible for the deposition of an incomplete monolayer and C3 for the bilayer [9]. At potentials negative of C3 bulk deposition of Ag occurs. The completion of the Ag monolayer occurs between C2 and C3. Although the charge of the first two cathodic peaks corresponds to 0.72 of a monolayer, Kondo *et al*. found using x-ray diffraction that the monolayer is actually complete at 0.05 V (vs Ag/Ag^+) [9].

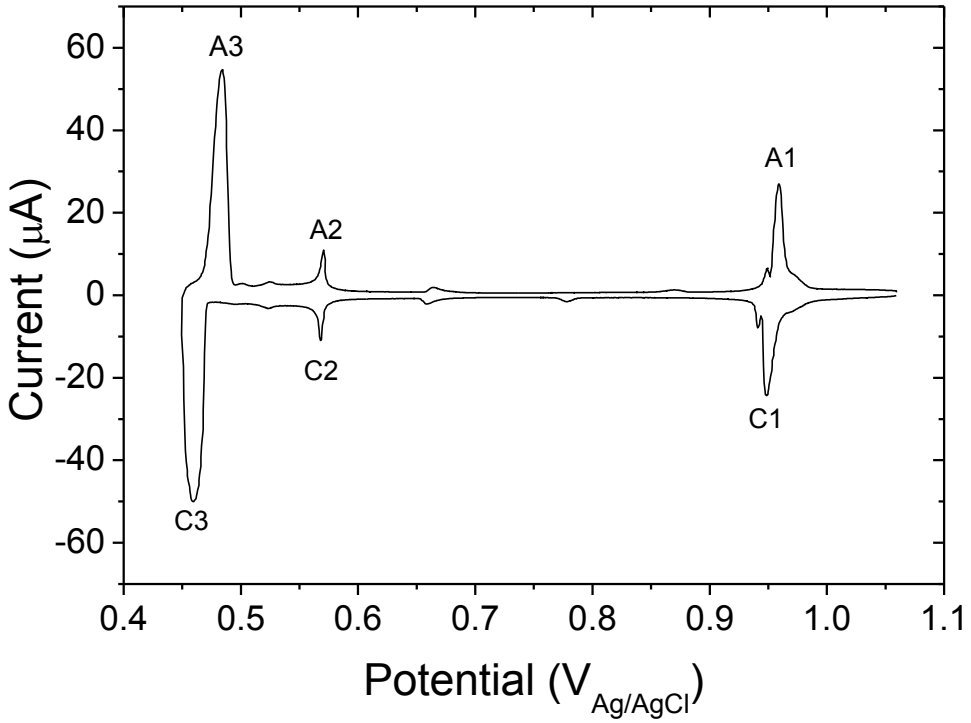

Figure 5.1 Cyclic voltammetry of Au(111) in 0.05 M H_2SO_4 + 1 mM Ag_2SO_4 recorded at a sweep rate of 5 mV/s vs Ag/AgCl.

Underpotential deposition was also performed with the Au(111) crystal in the electrochemical x-ray cell. This allowed x-ray diffraction measurements to be made in-situ during the Ag deposition process, including XRV measurements in which the scattered x-ray intensity at key reciprocal lattice positions is measured as a function of the applied electrode potential. Figure 5.2 shows the XRV at a sweep rate of 2 mV/s corresponding to the Ag UPD at reciprocal space positions (b) (0, 0, 1.5), (c) (1, 0, 3.7) and (d) (0, 1, 0.5) together with the CV from Figure 5.1 for reference. (0, 0, 1.5) is an 'anti-Bragg' position on the specular CTR sensitive to any layer ordering at the interface, including that of the electrolyte, the (1, 0, 3.7) is a position on the non-specular CTR sensitive to lattice relaxation of the Au surface and the (0, 1, 0.5) is an 'anti-Bragg' position on the non-specular CTR, (0, 1, L), and is sensitive to the Ag atoms which are commensurate with the Au lattice. Figure 5.3 shows ideal CTR's for clean Au(111) electrode (green), an Ag monolayer on Au(111) electrode (red) and an Ag bilayer on Au(111) electrode (blue) with the three XRV positions

indicated to aid understanding of the changes which occur in the XRV. It is also worth noting that the number of minima between each Bragg peak on the CTR corresponds to the number of commensurate layers, this is due to the diffraction from a crystal being similar to that from an N-slit interference function as mentioned in Chapter 2. The diffraction from a monolayer or bilayer on the crystal surface is convoluted with the bulk crystal diffraction pattern and as a result the monolayer has 1 minima between adjacent Bragg peaks whereas the bilayer has 2, as shown in Figure 5.3.

To discuss the XRV we will start at 1.06 V where the surface is free of Ag atoms, the potential is scanned cathodically (open symbols) and just before reaching C1 (Figure 5.1) a partial monolayer of Ag is deposited on the surface, thus causing the decay in intensity for all the XRV's at this potential. The intensity is then stable until reaching C2 where further silver is deposited. This is only apparent in Figure 5.2 (d) as further silver completing the monolayer reduces the intensity at the anti-Bragg position. The scattered intensity at the specular anti-Bragg position should also be sensitive to the monolayer completing as this position is very sensitive to changes in the topmost layer of Ag, however the intensity here is already at the background level. In the other two XRV's there is no change in the intensity but at the (0, 1, 0.5) position the intensity decays further until the monolayer is completed. Finally just before reaching C3 the monolayer completes and the bilayer starts to form. Again a change in intensity is measured at all the positions, the direction of which depends on the reciprocal space position as shown in Figure 5.3. It is important to note that the XRV measures the ordering at the surface so features may not always correlate exactly with those in the CV. The UPD process is fully reversible over this potential range as shown in both the CV and XRV.

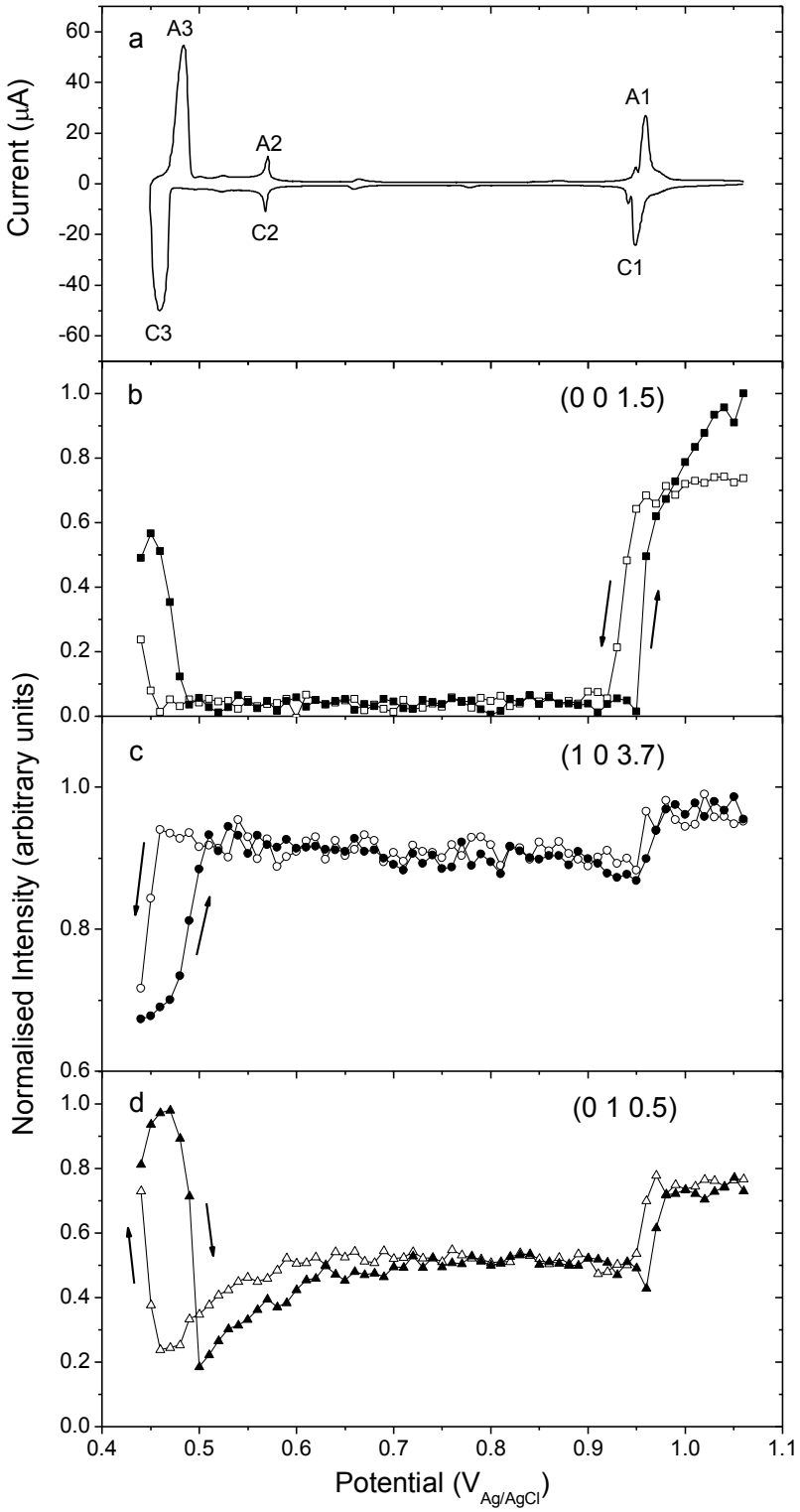

Figure 5.2 (a) Cyclic voltammetry of Au(111) in 0.05 M H_2SO_4 + 1 mM Ag_2SO_4 recorded at a sweep rate of 5 mV/s. X-Ray voltammetry (XRV) measured at (b) (0, 0, 1.5), (c) (1, 0, 3.7) and (d) (0, 1, 0.5) at a sweep rate of 2 mV/s vs Ag/AgCl and corrected for RC.

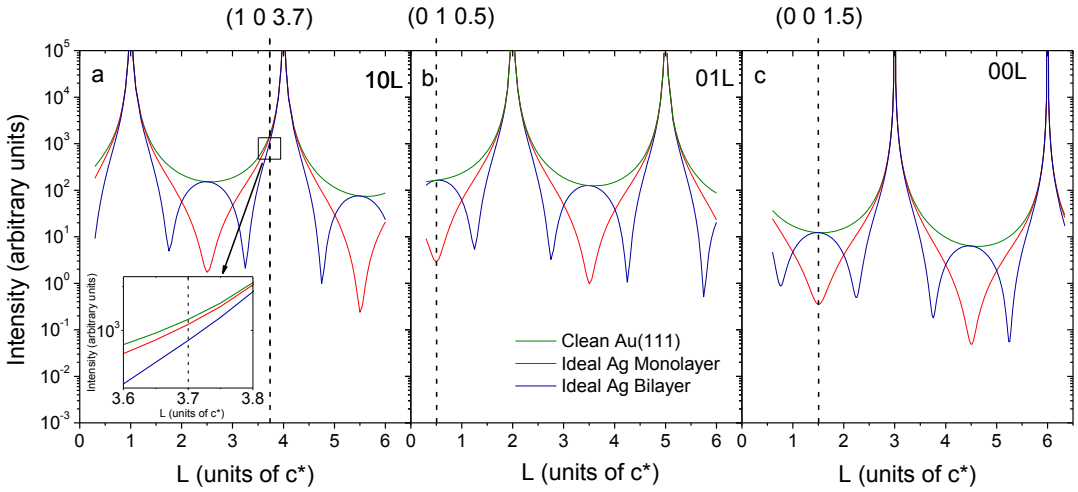

Figure 5.3 (a) (1, 0, L), (b) (0, 1, L) and (c) (0, 0, L) CTR models corresponding to the ideal surfaces of clean Au(111) (green), an Ag monolayer on Au(111) (red) and an Ag bilayer on Au(111) (blue). The positions corresponding to the XRV measurements are indicated by a dashed line. The inset shows the (1 0 3.7) position in more detail.

Following XRV studies of the deposition process the potential was scanned anodically from 0.44 V, where a bilayer would be present, to 0.47 V (which is between peaks C2 and C3 on Figure 5.1) in order to leave a monolayer of Ag deposited on the surface. The potential was then held at 0.47 V so that structural measurements could be made. In order to obtain a structural model for the Ag-Au(111) interface non-specular CTR's (1, 0, L) and (0, 1, L) were measured by performing rocking scans at successive L values to obtain background subtracted integrated intensities.

Figure 5.4 shows the non-specular CTR's for the Ag partial monolayer on Au(111) electrode taken at 0.47 V. The background-subtracted integrated intensities obtained from each rocking scan have been corrected for the instrumental resolution [41, 42] and are plotted versus L (black circles).

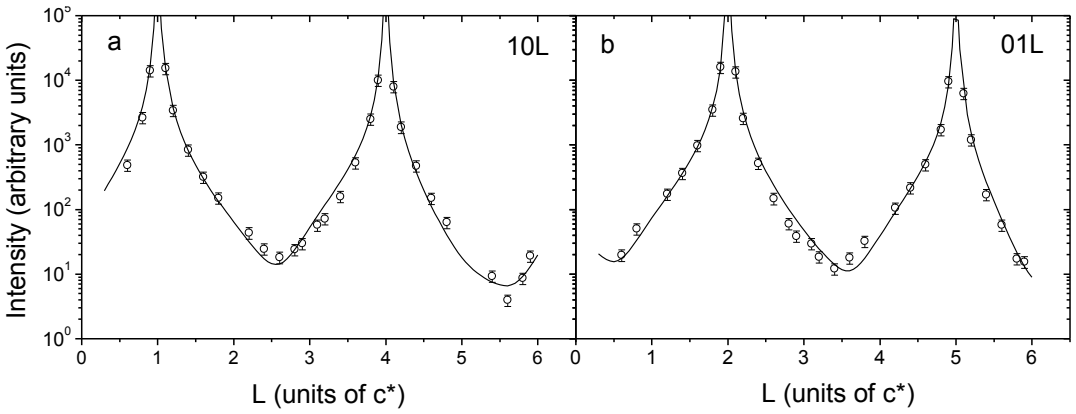

Figure 5.4 Crystal truncation rod (CTR) data (black circles) for the Ag monolayer on Au(111) measured in 0.05 M H_2SO_4 + 1 mM Ag_2SO_4 at 0.47 V for the non-specular CTR's (a) (1, 0, L) and (b) (0, 1, L) with the best fit to the data (black line).

The best fit to the CTR data (black line) was obtained using a least squares method in which the variable structural parameters were the relative occupation (θ) of the Ag atoms to surface Au atoms, surface atomic layer expansion (ε) (d-spacing) and root-mean-square(rms) surface roughness (σ) (modelled using a static Debye-Waller factor). The model used consisted of an Ag monolayer on a substrate of Au(111) as shown in Figure 5.5 where the corresponding d-spacings have been indicated. The occupation, d-spacing and rms surface roughness of the Ag layer and topmost Au(111) layer were allowed to vary. The bulk parameters used for Au(111) correspond to a d-spacing between adjacent atomic layers of 2.356 Å and are of an ideal crystal (full occupation (1 ML) and rms surface roughness = 0).

The best fit to the data ($\chi^2 = 2.6^*$) gives an Ag occupation of 0.6 monolayer (ML) (fraction of Ag atoms per surface Au atom) with the Ag layer relaxed inwards by 1.5% of Bulk Ag(111) d-spacing (2.361 Å). The top most Au layer is relaxed outwards by 0.5% of bulk Au(111) d-spacing (2.355 Å). Further parameters obtained are shown in Table 5.1. The Ag occupation obtained of 0.6 ML is lower than that expected from the literature and the corresponding CV and XRV measurements presented in this Chapter. One explanation may be that the CTR

* A systematic error on each data point of 20% was estimated by measurements made at symmetry-equivalent CTR positions.

was performed after cycling down to 0.44 V then back to 0.47 V so it is possible that the deposited Ag does not strip as uniformly as it is deposited.

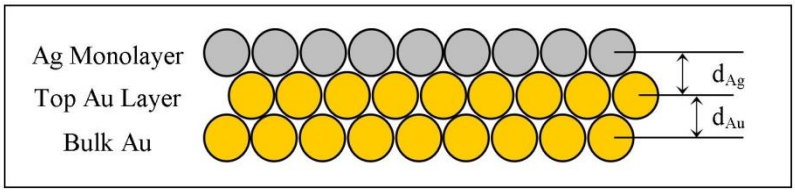

Figure 5.5 Schematic representation of an UPD Ag monolayer on Au(111). The d-spacings used as variable parameters in the fitting program are indicated.

	Occupation Θ (ML)	D-spacing ε (Å)	Surface Roughness σ (Å)
Top Au layer	1.0 ± 0.1	2.367 ± 0.006	0.12 ± 0.07
Ag Monolayer	0.6 ± 0.1	2.325 ± 0.032	0.12 ± 0.07

Table 5.1 Best fit parameters obtained from analysis of CTR data for Ag Monolayer on Au(111) measured in 0.05 M H_2SO_4 + 1 mM Ag_2SO_4 at 0.47 V. The fit parameters of occupation, d-spacing and surface roughness are shown for the top most Au layer and the Ag monolayer.

5.4 Transfer to Alkaline electrolyte

Transferring the Ag modified Au(111) crystal to a silver-free alkaline electrolyte enables potential dependent measurements to be made without further deposition of Ag atoms and by using 0.1M KOH we were able to study the region of OH^- adsorption. To study the Ag layers in alkaline electrolyte separate electrochemical cells were used for the deposition and subsequent x-ray measurements in alkaline electrolyte. First the hanging meniscus electrochemical cell containing nitrogen purged electrolyte 0.05 M H_2SO_4 + 1 mM Ag_2SO_4 was used to enable precise control of the deposition of Ag layers on the Au(111) surface. A monolayer or bilayer of Ag was formed on the Au(111) crystal, by holding the potential at 0.47 V and 0.45 V

respectively. Once the Ag layers were formed the crystal was transferred to the electrochemical x-ray cell with a drop of ultrapure water protecting the surface and immersed at open circuit potential into nitrogen purged alkaline electrolyte, 0.1 M KOH. After transferring the Ag modified Au(111) crystal to the alkaline electrolyte a series of CTR and XRV measurements were made to fully characterise the surface and understand its behaviour in alkaline electrolyte. CV measurements were also made in the hanging meniscus cell.

5.5 Studies of Ag-Au(111) in Alkaline Electrolyte

5.5.1 Cyclic Voltammetry of Ag layers on Au(111) in Alkaline Electrolyte

The cyclic voltammetry of the Ag monolayer and bilayer are shown in Figure 5.6 together with that of clean Au(111) surface in 0.1 M KOH. For the clean gold the potential region -0.9 V to -0.6 V corresponds to charging/discharging of the double layer and the potential region -0.6 V to 0 V corresponds to the reversible adsorption/desorption of oxygenated species, hereafter called OH [40]. The CV for both the Ag monolayer and bilayer on the Au(111) electrode show features which are characteristic of Ag crystal surfaces. Ag single crystals have been studied in NaOH electrolyte [3, 43, 44] and sets of peaks similar to A4 and C4 in Figure 5.6 have been attributed to the specific adsorption and desorption of OH^- anions. Savinova *et al*. attributed features similar to C5 to the sub-surface incorporation of OH species into Ag(111) [45, 46] and polycrystalline (pc) Ag [47] in NaF + NaOH electrolyte.

The potential region for OH^- anion adsorption on Ag single crystals is dependent on the single crystal surface [43]. This is reflected by a difference in the potential of OH^- anion adsorption for the Ag monolayer compared to the Ag bilayer and will be addressed in more detail in Section 5.6. The potential ranges for the following CTR measurements are marginally different for the 2 cases to account for this.

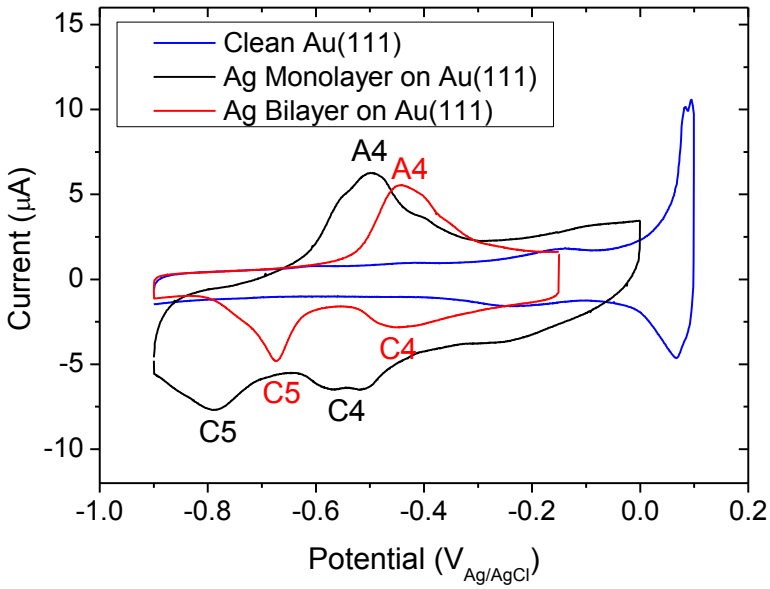

Figure 5.6 Cyclic voltammetry of clean Au(111) (blue line), Ag monolayer on Au(111) (black line) and Ag bilayer on Au(111) (red line) in 0.1 M KOH at a sweep rate of 20 mV/s.

5.5.2 Ag Bilayer on Au(111)

As previously mentioned the Au(111) crystal was held at 0.45 V in 0.05 M H_2SO_4 + 1 mM Ag_2SO_4 electrolyte to deposit a bilayer of Ag on the Au(111) surface. Once the Ag layers were formed the crystal was transferred to the electrochemical x-ray cell containing nitrogen purged alkaline electrolyte, 0.1 M KOH. Specular CTR (0, 0, L) measurements of the Ag bilayer on Au(111) surface were performed at fixed potentials of -0.9 V and -0.1 V by performing rocking scans at successive L values.

Figure 5.7 (a) shows the specular CTR (0, 0, L) obtained for the Ag bilayer on Au(111) electrode in 0.1 M KOH at the fixed potentials -0.9 V (black circles) and -0.1 V (red squares). Best fits to the CTR data (solid lines) were obtained using a least squares method in which the variable structural parameters were the relative occupation (θ), surface atomic layer expansion (ε) (d-spacing) and root-mean-square (rms) surface roughness (σ) (modelled using a static Debye-Waller factor). The structural model used consisted of 2 Ag monolayers on a substrate of Au(111)

as shown in Figure 5.8. The addition of an OH^- layer was also required at -0.1 V and shall be discussed shortly. The occupation, d-spacing and rms surface roughness of the 2 Ag layers and topmost Au(111) layer were allowed to vary. The bulk parameters used for Au(111) crystal correspond to a d-spacing between adjacent atomic layers of 2.356 Å and are of an ideal crystal (full occupation (1 ML)). The corresponding best fit parameters for the data at -0.9 V and -0.1 V are given in Table 5.2 and Table 5.3 respectively.

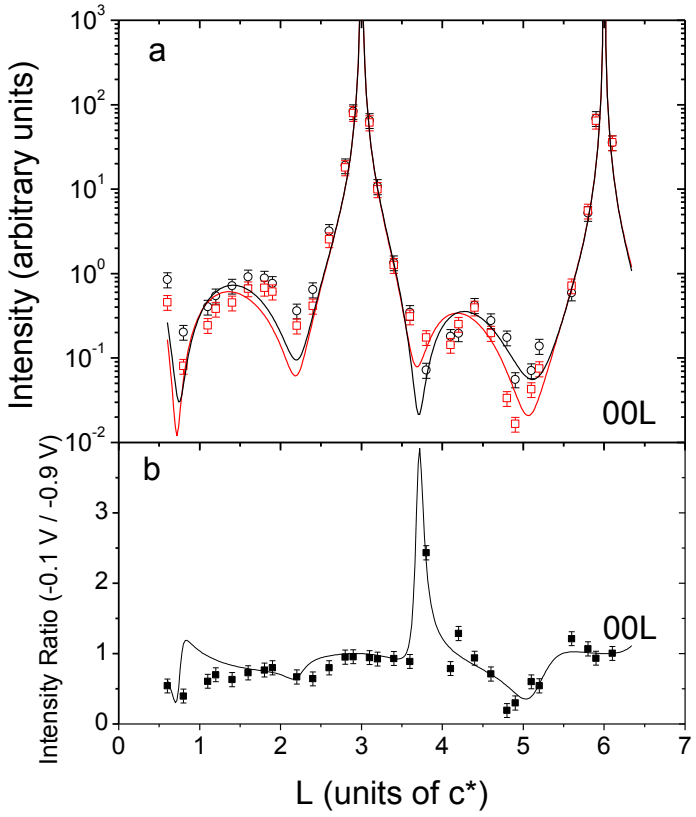

Figure 5.7 (a) Specular CTR (0, 0, L) data for Ag bilayer on Au(111) in 0.1 M KOH at -0.9 V (black circles) and -0.1 V (red squares). The solid lines are fits to the data according to the structural model described in the text. (b) The ratio of the -0.1 V CTR / -0.9 V CTR for the (0, 0, L).

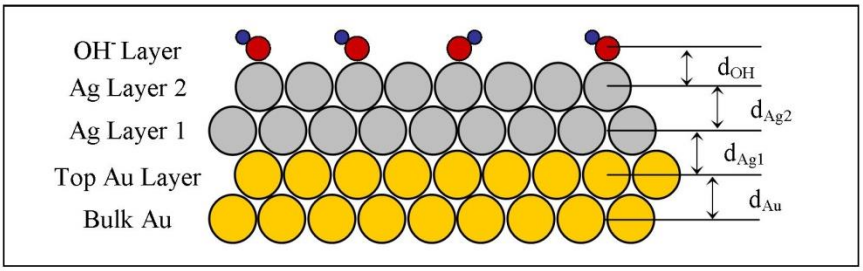

Figure 5.8 Schematic representation of an UPD Ag bilayer on Au(111). The d-spacings used as variable parameters by the fitting program are indicated.

At -0.9 V the best fit ($\chi^2 = 5.4$ using errors of 20 % of the data point) consists of 2 Ag layers on Au(111) surface each with an occupation of 1 ML. The top most Au layer is relaxed inwards by 0.4 % (with respect to (wrt) the bulk Au(111) crystal). The Ag layer 1 is relaxed inwards by 0.6 % (wrt bulk Ag(111)) and Ag layer 2 relaxed outward by 3.3 % (wrt bulk Ag(111)).

Figure 5.7 (b) shows the ratio of the set of specular CTR's ($R = I_{-0.1\ V} / I_{-0.9\ V}$) (black squares) which was used to highlight the differences between the -0.9 V and -0.1 V data together with the best fit to the ratio (black line) ($\chi^2 = 4.7$ using a fixed error of 0.1 for each ratio data point). The specular CTR is of particular interest as it is sensitive to any layer ordering at the interface, including that of the electrolyte [48]. In order to get a good fit to the data at -0.1 V it was necessary to add a layer on the electrolyte side of the interface. This extra layer is assigned to OH^- with a coverage, θ_{OH} = 0.45 ML, and a d-spacing of 2.19 Å which is very similar to that found for Ag(111) electrode in 0.1M KOH [48]. There was very little change to the top most Au layer and Ag layer 1 compared with the more negative potential. However the Ag layer 2 had a further increase in d-spacing. This may be due to presence of subsurface OH causing an increase in the Ag-Ag spacing and will be discussed further in Section 5.6.

	Occupation Θ (ML)	D-spacing ε (Å)	Surface Roughness σ (Å)
Au	1 ± 0.14	2.347 ± 0.014	0.05 ± 0.08
Ag 1	1 ± 0.12	2.346 ± 0.042	0.05 ± 0.10
Ag 2	1 ± 0.31	2.438 ± 0.071	0.1 ± 0.25

Table 5.2 Best fit parameters obtained from analysis of CTR data for Ag bilayer on Au(111) measured in 0.1 M KOH at -0.9 V. The fit parameters of occupation, d-spacing and surface roughness are shown for the top most Au layer and the Ag layers 1 and 2.

	Occupation Θ (ML)	D-spacing ε (Å)	Surface Roughness σ (Å)
Au	1 ± 0.07	2.346 ± 0.016	0.05 ± 0.05
Ag 1	1 ± 0.07	2.346 ± 0.014	0.11 ± 0.04
Ag 2	1 ± 0.06	2.466 ± 0.078	0.17 ± 0.02
OH^-	0.45 ± 0.3	2.191 ± 0.07	0.3 ± 0.2

Table 5.3 Best fit parameters obtained from analysis of CTR data for Ag bilayer on Au(111) measured in 0.1 M KOH at -0.1 V. The fit parameters of occupation, d-spacing and surface roughness are shown for the top most Au layer and the Ag layers 1 and 2.

5.5.3 Ag Monolayer on Au(111)

The Au(111) crystal was re-prepared and a monolayer of Ag deposited on the surface by holding the potential at 0.47 V in 0.05 M H_2SO_4 + 1 mM Ag_2SO_4 electrolyte before transferring to alkaline electrolyte. Figure 5.9 shows the specular CTR (a) (0, 0, L) and the non-specular CTR's (b) (1, 0, L) and (c) (0, 1, L) for the Ag monolayer on Au(111) surface at -1 V (black circles) and -0.2 V (red squares). It is clear from the profile of the CTR's that on transfer to the alkaline electrolyte the

monolayer changes to a partial bilayer. This is supported by previous studies which found that on exposure to ambient atmosphere the Ag monolayer on the Au(111) surface transforms to a partial bilayer [12]. For clarity this will henceforth be referred to as the monolayer deposit. The same best fit procedure was followed as for the Ag bilayer. The corresponding best fit parameters for the data at -1 V and -0.2 V are given in Table 5.4 and Table 5.5 respectively.

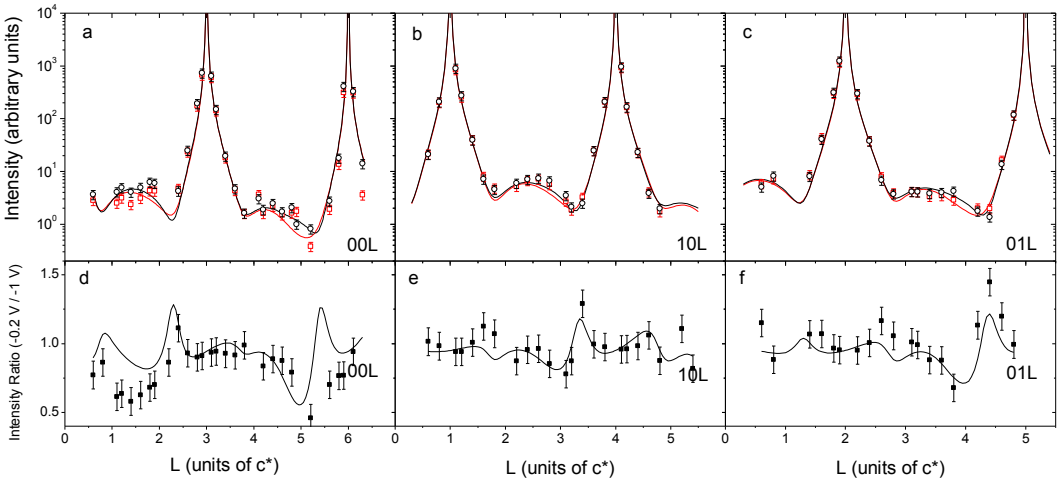

Figure 5.9 CTR data of the Ag monolayer on Au(111) in 0.1 M KOH at -1.0 V (black circles) and -0.2 V (red squares) for **(a)** the specular CTR (0, 0, L) and the non-specular CTR's **(b)** (1, 0, L) and **(c)** (0, 1, L). The solid lines are fits to the data according to the structural model described in the text. The ratio of the -0.2 V CTR / -1 V CTR for the **(d)** (0, 0, L), **(e)** (1, 0, L) and **(f)** (0, 1, L).

At the negative potential limit (-1 V) the best fit ($\chi^2 = 2.5$) indicates that the new Ag structure is composed of 2 Ag layers with a occupation of 0.5 ML each. The Ag layer 1 is relaxed inwards by 3.04 % (wrt bulk Ag(111)) and Ag layer 2 relaxed outward by 1.15 % (wrt bulk Ag(111)). The reduced occupation in the topmost Au layer may be due to a roughening/alloying effect that occurs when Ag is repeatedly deposited and stripped from the Au(111) surface.

Figure 5.9 also shows ratios of each set of CTR's ($R = I_{-0.2\,V} / I_{-1\,V}$) (black squares) (d) (0, 0, L), (e) (1, 0, L) and (f) (0, 1, L) together with the best fit to the ratio (black line) ($\chi^2 = 1.9$). As for the bilayer deposit, an OH^- layer was added in order to improve

the fit to the data and its coverage was found to be θ_{OH} = 0.2 ML with a d-spacing of 2.19 Å.

	Occupation Θ (ML)	D-spacing ε (Å)	Surface Roughness σ (Å)
Au	0.92 ± 0.07	2.348 ± 0.007	0.1 ± 0.1
Ag 1	0.5 ± 0.10	2.290 ± 0.057	0.1 ± 0.1
Ag 2	0.5 ± 0.13	2.389 ± 0.085	0.1 ± 0.1

Table 5.4 Best fit parameters obtained from analysis of CTR data for Ag monolayer on Au(111) measured in 0.1 M KOH at -1 V. The fit parameters of occupation, d-spacing and surface roughness are shown for the top most Au layer and the Ag layers 1 and 2.

	Occupation Θ (ML)	D-spacing ε (Å)	Surface Roughness σ (Å)
Au	0.92 ± 0.12	2.342 ± 0.010	0.10 ± 0.18
Ag 1	0.5 ± 0.18	2.353 ± 0.078	0.11 ± 0.19
Ag 2	0.5 ± 0.25	2.283 ± 0.120	0.17 ± 0.23
OH^-	0.2 ± 0.2	2.191 ±	0.3 ± 0.4

Table 5.5 Best fit parameters obtained from analysis of CTR data for Ag monolayer on Au(111) measured in 0.1 M KOH at -0.2 V. The fit parameters of occupation, d-spacing and surface roughness are shown for the top most Au layer and the Ag layers 1 and 2.

5.5.4 Potential dependence in 0.1M KOH

In addition to the CTR measurements further XRV measurements were performed on Ag (1 ML) and Ag (2 ML) films in alkaline electrolyte. Figure 5.10 shows the XRV for the Ag monolayer and bilayer in 0.1 M KOH. The XRV measurements were made at the reciprocal lattice positions used to monitor Ag deposition i.e. (a) (0, 0, 1.52), (b) (1, 0 3.7) and (c) (0, 1, 0.51). The changes in the specular 'anti-Bragg' position are quite significant ~30%. The same shift in potential response that was seen in the CV (Figure 5.6) between the monolayer and bilayer structures is present. The increase in the intensity at the (0, 0, 1.5) position on the cathodic scan commences at the same potential as the peaks C4 (Figure 5.6) suggesting that the change occurring is related to OH^- desorption. The non-specular CTR positions show more subtle changes which can be attributed to small relaxations in the Ag-Ag and Ag-Au layer spacing. The observed changes are fully reproduced in the potentiostatic CTR measurements and the data in Figure 5.10 is totally consistent with the CTR data in Figure 5.7 and Figure 5.9. For comparison Figure 5.11 shows the XRV at (0, 0, 1.52) for the Au(111) electrode and the Ag(111) electrode in 0.1M KOH. For the pure single crystal surface the changes in the XRV for Ag(111) electrode are due to structural changes in the electrolyte side of the interface and for Au(111) electrode are due to the lifting and reforming of the Au surface reconstruction.

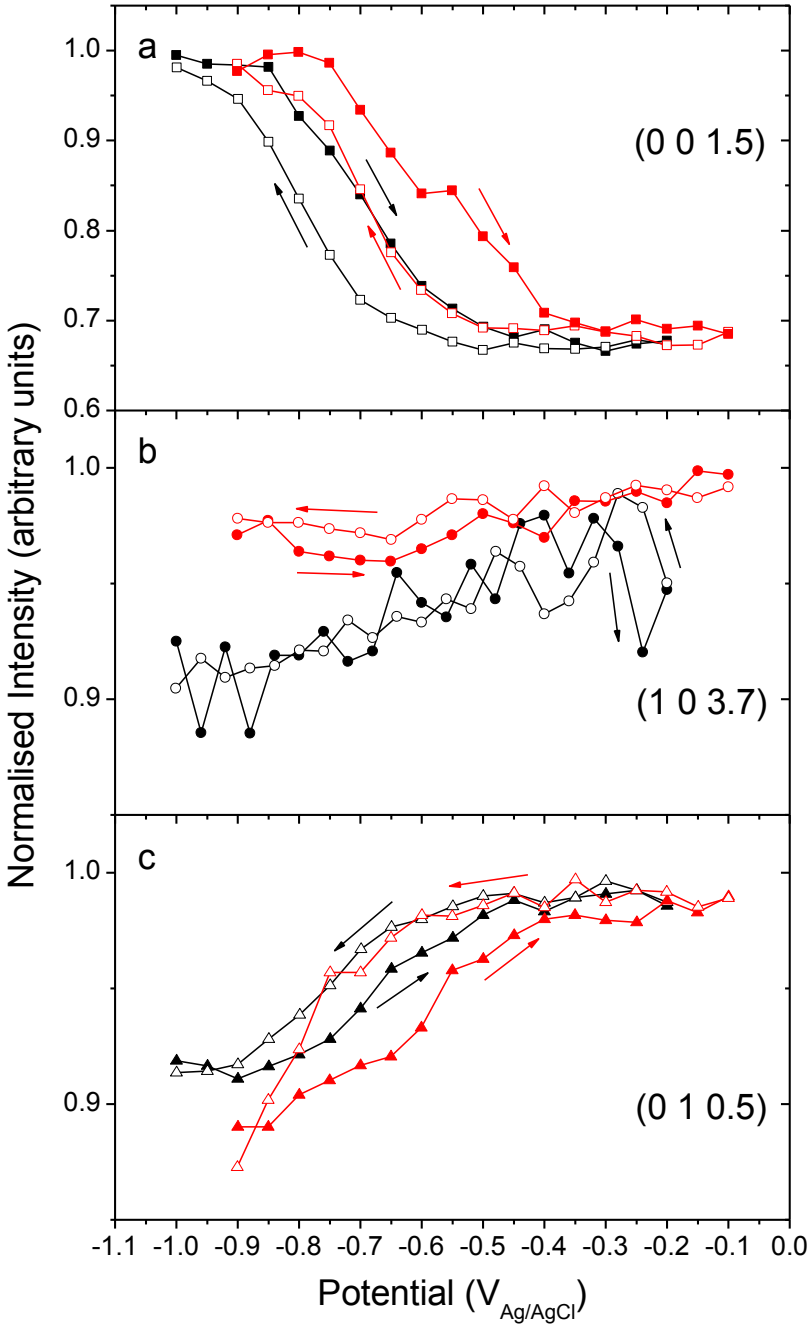

Figure 5.10 X-ray voltammetry (XRV) for Ag monolayer on Au(111) (black line) and Ag bilayer on Au(111) (red line) in 0.1 M KOH, measured at (a) (0, 0, 1.52), (b) (1, 0, 3.7) and (c) (0, 1, 0.51) at a sweep rate of 5 mV/s.

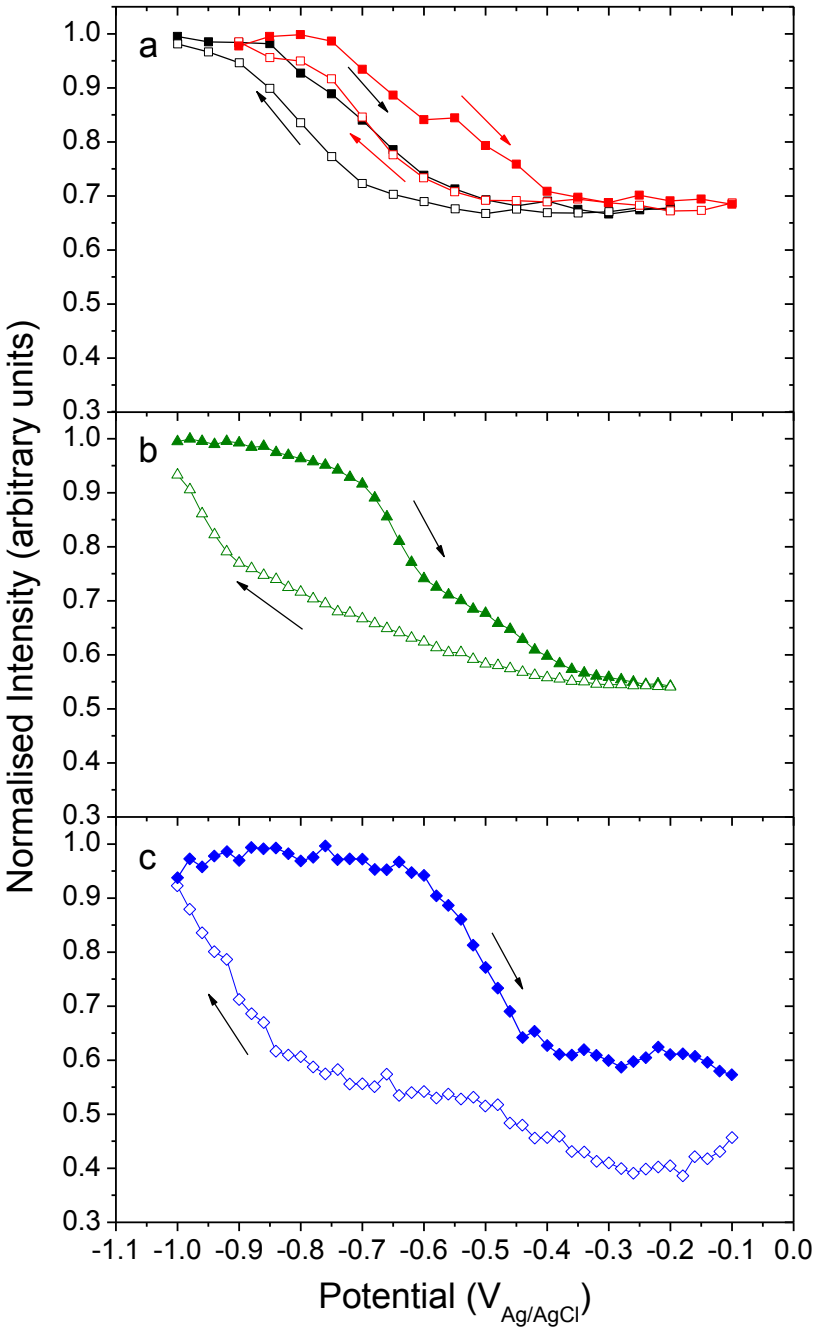

Figure 5.11 X-ray voltammetry (XRV) measured at (0, 0, 1.52) for (a) Ag monolayer on Au(111) (black line) and Ag bilayer on Au(111) (red line) in 0.1 M KOH, (b) Ag(111) in 0.1 M KOH and (c) Au(111) in 0.1 M KOH at a sweep rate of 5 mV/s.

5.6 Summary

The structure and electrochemical behaviour of UPD Ag monolayer and bilayer on Au(111) have been studied using SXS and CV. Figure 5.12 shows a schematic illustration of the structural changes for both the Ag monolayer and bilayer on Au(111). It is clear from the CTR measurements that on transfer to the alkaline electrolyte the Ag bilayer on Au(111) was stable, conversely the Ag monolayer re-orders to a partial bilayer structure. Marinkovic *et al* found that in an electrolyte containing both OH and SO_4 (0.1 M K_2SO_4 + 0.01 M NaOH) the adsorption of sulphate on Ag(111) surface is inhibited by the more strongly specifically adsorbed OH^- ions [49]. It is therefore likely that for the Ag monolayer on Au(111) the sulphate anions which are stabilising the monolayer structure [50] are replaced by OH^- causing the silver to rearrange to a more stable state – e.g. a partial bilayer. Detailed modelling of the CTRs required an OH^- layer in the electrolyte side of the interface. The coverage of the OH^- layer was found to be 0.45 ML for the complete bilayer and 0.2 ML for the partial bilayer. As shown in Figure 5.6 the potential of OH^- adsorption on the Ag/Au(111) surface is dependent on the silver deposited. It has been shown that for Ag single crystals in sodium hydroxide electrolytes the potential for OH^- adsorption/desorption is dependent on the single crystal surface, with the OH^- adsorption/desorption potential decreasing in the order Ag(111) > Ag(100) > Ag(110) [43, 44]. Horswell *et al*. showed that this effect is related to the *pzc* for each surface as when the CV's are plotted with respect to the *pzc* (on a rational potential scale) the potential of OH^- adsorption/desorption for the different faces coincide [43]. They inferred that the onset of OH^- adsorption on the different Ag single-crystal planes is related to the work function and atomic density of the surface [43]. The *pzc* of Au(111) and Ag(111) are separated by approximately 1 V in the order Au(111) < Au(100) < Au(110) < Ag(111) < Ag(100) < Ag(110) [35, 51]. For sub monolayer coverage of Ag on Au(111) the *pzc* stays close to that of Au(111) shifting from -0.55 V for clean Au(111) to -0.75 V (vs Ag/AgCl/KCl (sat) in 0.1M NaOH) with the deposition of 1/3 ML[52]. As the monolayer is completed the

pzc shifts close to that of Ag(111), becoming almost identical to that of Ag (111) with the deposition of the second monolayer [35, 53, 54].

By considering all of the above it possible to conclude that the bilayer surface is stable on transfer and has a similar behaviour in 0.1 M KOH to that of the Ag(111) electrode. The monolayer on the other hand is not stable and, although a Ag surface structure with a (111) close packed structure is initially formed, on transfer to the alkaline electrolyte the sulphate anions, which stabilise the monolayer structure, are removed by the more strongly adsorbed OH^- ions and the silver rearranges itself to a partial bilayer. The new partial bilayer surface results in the creation of Ag (100) and (110) step sites, which have a lower *pzc* and as a result a lower potential for OH^- adsorption. This accounts for the lower potential of OH^- adsorption/desorption for the monolayer compared to the bilayer shown in Figure 5.6 and Figure 5.10 (a).

Savinova *et al*. found a cathodic peak on Ag(111) and Ag(pc) in sodium hydroxide electrolytes similar to C5 (Figure 5.6) and suggested this was due to subsurface OH [45-47]. The diffusion of OH species in the bulk is a slow process on Ag(111), but is much faster for Ag(pc) due to the higher concentration of the grain boundaries and other defects. This would explain why C5 is so pronounced for the supported Ag multilayers, as these UPD surfaces would have many defects. The amount of subsurface OH measured by Savinova *et al*. does not exceed 0.04 ML so would be extremely difficult to model directly, however it would cause an increase in the surface roughening which is seen for both the monolayer and bilayer systems at the positive potential limit.

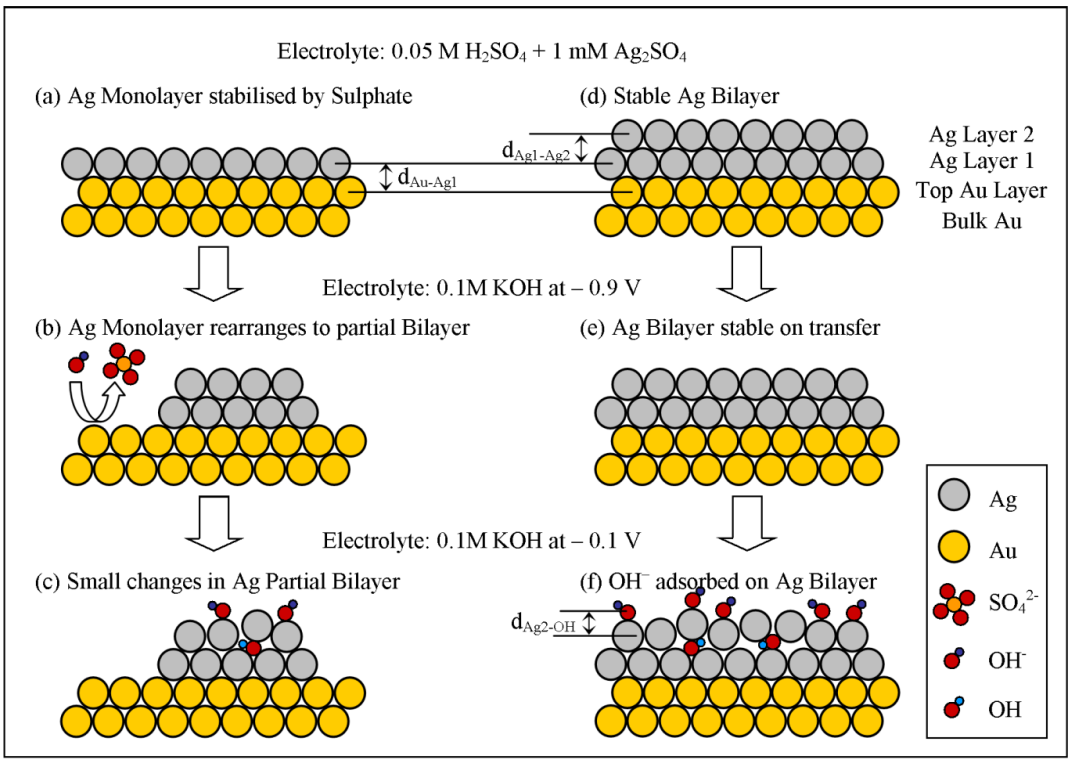

Figure 5.12 Schematic illustration of all the structural changes for an underpotentially deposited Ag Monolayer and Bilayer on Au(111) before and after transfer to alkaline electrolyte.

5.7 References:

[1] C.I. Carlisle, D.A. King, M.L. Bocquet, J. Cerda, P. Sautet, Phys Rev Lett, 84 (2000) 3899-3902.
[2] W.X. Li, C. Stampfl, M. Scheffler, Phys Rev B, 65 (2002).
[3] E.R. Savinova, A. Scheybal, M. Danckwerts, U. Wild, B. Pettinger, K. Doblhofer, R. Schlogl, G. Ertl, Faraday Discuss, 121 (2002) 181-198.
[4] M. Danckwerts, E.R. Savinova, S.L. Horswell, B. Pettinger, K. Doblhofer, Z Phys Chem, 217 (2003) 557-572.
[5] C. Wang, M.F. Chi, D.G. Li, D. van der Vliet, G.F. Wang, Q.Y. Lin, J.F. Mitchell, K.L. More, N.M. Markovic, V.R. Stamenkovic, Acs Catal, 1 (2011) 1355-1359.
[6] N. Danilovic, R. Subbaraman, D. Strmcnik, K.C. Chang, A.P. Paulikas, V.R. Stamenkovic, N.M. Markovic, Angew Chem Int Edit, 51 (2012) 12495-12498.
[7] V.R. Stamenkovic, B.S. Mun, M. Arenz, K.J.J. Mayrhofer, C.A. Lucas, G.F. Wang, P.N. Ross, N.M. Markovic, Nat Mater, 6 (2007) 241-247.
[8] B. Fowler, C.A. Lucas, A. Omer, G. Wang, V.R. Stamenkovic, N.M. Markovic, Electrochim Acta, 53 (2008) 6076-6080.
[9] T. Kondo, J. Morita, M. Okamura, T. Saito, K. Uosaki, J Electroanal Chem, 532 (2002) 201-205.
[10] E. Herrero, L.J. Buller, H.D. Abruna, Chem Rev, 101 (2001) 1897-1930.
[11] J.D. Snyder, J.D. Erlebacher, Langmuir, 25 (2009) 9596-9604.
[12] T. Kondo, S. Takakusagi, K. Uosaki, Electrochem Commun, 11 (2009) 804-807.
[13] S.S. Shankar, A. Rai, A. Ahmad, M. Sastry, J Colloid Interf Sci, 275 (2004) 496-502.
[14] S.P. Chandran, J. Ghatak, P.V. Satyam, M. Sastry, J Colloid Interf Sci, 312 (2007) 498-505.
[15] S. Pande, S.K. Ghosh, S. Praharaj, S. Panigrahi, S. Basu, S. Jana, A. Pal, T. Tsukuda, T. Pal, J Phys Chem C, 111 (2007) 10806-10813.
[16] H.M. Chen, R.S. Liu, L.Y. Jang, J.F. Lee, S.F. Hu, Chem Phys Lett, 421 (2006) 118-123.
[17] M. Banerjee, S. Sharma, A. Chattopadhyay, S.S. Ghosh, Nanoscale, 3 (2011) 5120-5125.
[18] H.L. Jiang, T. Akita, T. Ishida, M. Haruta, Q. Xu, J Am Chem Soc, 133 (2011) 1304-1306.
[19] A.C. Fisher, Electrode Dynamics, Oxford University Press, Oxford, (2006).
[20] D.M. Kolb, Angew Chem Int Edit, 40 (2001) 1162-1181.
[21] D.M. Kolb, Surf Sci, 500 (2002) 722-740.
[22] N. Markovic, P.N. Ross, Langmuir, 9 (1993) 580-590.
[23] Y. Grunder, P. Thompson, A. Brownrigg, M. Darlington, C.A. Lucas, J Phys Chem C, 116 (2012) 6283-6288.
[24] F.A. Moller, O.M. Magnussen, R.J. Behm, Phys Rev B, 51 (1995) 2484-2490.
[25] J.L. Bubendorff, L. Cagnon, V. CostaKieling, J.P. Bucher, P. Allongue, Surf Sci, 384 (1997) L836-L843.
[26] R. Gomez, J.M. Feliu, J Electroanal Chem, 554 (2003) 145-156.

[27] L.Y.O. Yang, F. Bensliman, C.H. Shue, Y.C. Yang, Z.H. Zang, L. Wang, S.L. Yau, S. Yoshimoto, K. Itaya, J Phys Chem B, 109 (2005) 14917-14924.
[28] M.M. Dovek, C.A. Lang, J. Nogami, C.F. Quate, Phys Rev B, 40 (1989) 11973-11975.
[29] D.D. Chambliss, R.J. Wilson, J Vac Sci Technol B, 9 (1991) 928-932.
[30] M. Jurczyszyn, I. Morawski, M. Nowicki, Thin Solid Films, 519 (2011) 6196-6201.
[31] C.H. Chen, S.M. Vesecky, A.A. Gewirth, J Am Chem Soc, 114 (1992) 451-458.
[32] C.H. Chen, A.A. Gewirth, Ultramicroscopy, 42 (1992) 437-444.
[33] P. Mrozek, Y.E. Sung, M. Han, M. Gamboaaldeco, A. Wieckowski, C.H. Chen, A.A. Gewirth, Electrochim Acta, 40 (1995) 17-28.
[34] D. Borissov, C.L. Aravinda, W. Freyland, J Phys Chem B, 109 (2005) 11606-11615.
[35] M.J. Esplandiu, M.A. Schneeweiss, D.M. Kolb, Phys Chem Chem Phys, 1 (1999) 4847-4854.
[36] S. Garcia, D. Salinas, C. Mayer, E. Schmidt, G. Staikov, W.J. Lorenz, Electrochim Acta, 43 (1998) 3007-3019.
[37] C.G. Sanchez, S.A. Dassie, E.P.M. Leiva, Langmuir, 18 (2002) 6628-6632.
[38] M. Schweizer, D.M. Kolb, Surf Sci, 544 (2003) 93-102.
[39] D.D. Fong, C.A. Lucas, M.I. Richard, M.F. Toney, Mrs Bull, 35 (2010) 504-513.
[40] M.E. Gallagher, B.B. Blizanac, C.A. Lucas, P.N. Ross, N.M. Markovic, Surf Sci, 582 (2005) 215-226.
[41] E. Vlieg, J Appl Crystallogr, 31 (1998) 198-203.
[42] E. Vlieg, J Appl Crystallogr, 30 (1997) 532-543.
[43] S.L. Horswell, A.L.N. Pinheiro, E.R. Savinova, M. Danckwerts, B. Pettinger, M.S. Zei, G. Ertl, Langmuir, 20 (2004) 10970-10981.
[44] B.M. Jovic, V.D. Jovic, G.R. Stafford, Electrochem Commun, 1 (1999) 247-251.
[45] E.R. Savinova, D. Zemlyanov, B. Pettinger, A. Scheybal, R. Schlogl, K. Doblhofer, Electrochim Acta, 46 (2000) 175-183.
[46] D.Y. Zemlyanov, E. Savinova, A. Scheybal, K. Doblhofer, R. Schlogl, Surf Sci, 418 (1998) 441-456.
[47] E.R. Savinova, S. Wasle, K. Doblhofer, Electrochim Acta, 44 (1998) 1341-1348.
[48] C.A. Lucas, P. Thompson, Y. Grunder, N.M. Markovic, Electrochem Commun, 13 (2011) 1205-1208.
[49] N.S. Marinkovic, J.S. Marinkovic, R.R. Adzic, J Electroanal Chem, 467 (1999) 291-298.
[50] P. Mrozek, Y.E. Sung, A. Wieckowski, Surf Sci, 335 (1995) 44-51.
[51] S. Trasatti, J Electroanal Chem, 329 (1992) 237-246.
[52] S. Ben Aoun, Z. Dursun, T. Koga, G.S. Bang, T. Sotomura, I. Taniguchi, J Electroanal Chem, 567 (2004) 175-183.
[53] K.A. Soliman, L.A. Kibler, Electrochim Acta, 52 (2007) 5654-5658.
[54] K.O. Thiel, A. Vollmer, M. Hintze, E. Avci, C. Donner, Z Phys Chem, 221 (2007) 1255-1271.

Chapter 6:

Thin Co Films Electrodeposited onto Au(111)

6.1 Introduction

Deposition processes and structure formation at the electrochemical interface enables a number of modern technologies, ranging from the formation of nanosized electronic components to the tailoring of surface reactivity in catalytically active materials. Ultrathin magnetic layers are important devices from a fundamental as well as from a technological viewpoint. Among specific properties, perpendicular magnetization anisotropy (PMA) is one phenomenon of strong interest for high density data storage, in particular with respect to the switching of the magnetization easy axis in ultrathin magnetic layers, i.e. also called spin reorientation transition (SRT) [1]. Many different systems exhibit interface driven PMA [2], for instance PMA at Co/Au(111) [3] layers mainly arises from a modification of the magnetic moment of cobalt atoms due to their hybridization

with gold atoms. To be observable PMA requires, in this peculiar case, cobalt layers that are thinner than 5-6 cobalt atomic planes and the method of sample preparation is key in determining the inner structure of the deposited metal layers and the morphology of the interfaces, e.g. roughness, intermixing etc. In this respect electrochemistry stands as a powerful method for preparing epitaxial films and nanostructures over large surfaces [4]. Initial studies have shown that Co/Au(111) layers can be grown from a modified Watts bath [5] and the method has been extended to produce thin Au/Co bilayer structures [6]. Co/Au(111) layers prepared in this way exhibit an interface driven PMA if the cobalt layer is thinner than a critical thickness t* of ~8 ML (monolayer) that is comparable to that found for Co films grown by molecular beam epitaxy (MBE).

In situ magnetic characterization, using the magneto optical kerr effect (MOKE), revealed however that t* was only 1.6 ML as long as the Co/Au(111) layer stays in contact with the electrolyte solution (note: t* ~8 ML is measured after capping the Co film with Au) [3, 7]. This illustrates the strong influence of the Co/electrolyte interface on the overall magnetic anisotropy of the system. The in-situ measurements also suggest the SRT (from perpendicular to in-plane magnetisation) coincides with the coalescence of the biatomic Co islands [3] indicating that structural factors such as strain and relaxation may be responsible.

Recent MOKE results [8] also indicated that the interface anisotropy may be altered in two ways: (i) By adsorption of small molecules: for instance CO (carbon monoxide) increases *t** to ~6-8 ML. The effect is not only observable at room temperature but is also stronger than reported in vacuum (low temperature is also required in UHV). (ii) By changing the surface charge (via the electrode potential): For instance the coercive field of a 1.6 ML Co film varies by 50% over a ~300 mV range of applied potential. Figure 6.1 shows an example of these magnetization curves [unpublished work by P. Allongue and F. Maroun] for a 2.2 ML Co film covered by CO and measured at different potentials. The surface charge effect is becoming very topical as it opens the route to new magnetization switching

methods in memory or storage devices [9]. Theoretical works predict that charge transfer is at the origin of this phenomenon [10]. The possible role of charge-induced structural changes has not been investigated so far and therefore remains an open question. In this context, the electrochemical interface offers invaluable advantages over solid state structures since the magnetic layer is not buried under other material. Hence one may considerably vary the surface charge of the magnetic layer within a narrow potential window of ~1 V and, due to the specific structure at the electrochemical interface, electric fields as large as 0.3 V/Å are attainable. In addition, by saturating the electrolyte with CO it possible to study the effect of CO adsorption on the magnetic properties.

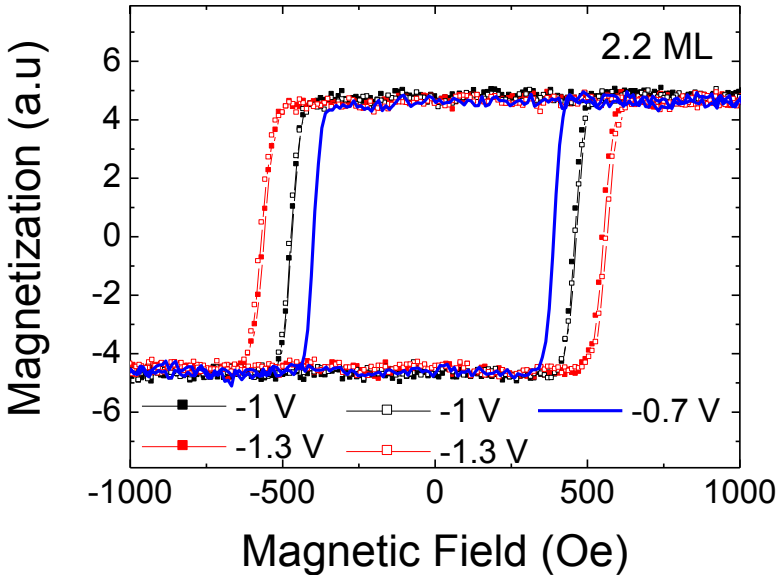

Figure 6.1 Hysteresis loop of a 2.2 ML Co film covered by carbon monoxide at different potentials. [unpublished work by P. Allongue and F. Maroun]

The development of *in-situ* experimental techniques, such as surface x-ray scattering (SXS) and scanning tunneling microscopy (STM), for studying the electrochemical interface has allowed an atomic-scale understanding of structure and phase formation and several reviews of these techniques have been published [11-15]. Whereas STM is useful for probing the surface structure and thin film morphology, SXS can give information on sub-surface structures and provide high

precision measurements of strain in thin epitaxial films. In this chapter in-situ STM and SXS techniques are combined to probe the growth and structure of Co thin films on Au(111). The growth of the Co films is monitored in real time with the thickness of the Co film being correlated to the strain. Surface relaxation and the Co-Au interface structure is probed in detail for a two monolayer thick (2 ML) Co film. The electrolyte is then saturated with CO to study the influence of adsorbed CO on the surface structure and strain in the Co thin film. The results are discussed in relation to the magnetic properties.

6.2 Experimental Methods

The Au(111) crystal was prepared as described in Section 3.2 and transferred to the electrochemical x-ray cell with a drop of ultra pure water protecting the surface and was immersed at open circuit potential in electrolyte. The electrolyte used in all x-ray experiments consisted of 1mM $CoSO_4$ in supporting electrolyte 10mM K_2SO_4 + 1mM H_2SO_4 + 0.1mM KCl (pH ~ 4). X-ray measurements were performed on beamline BM28 (XMaS), the UK-CRG beamline at the ESRF, Grenoble and on the 6-circle surface diffractometer at the ID32 beamline at the ESRF, Grenoble. The measurements on XMaS used the diffractometer in a 4-circle mode with incident x-rays of energy 11 keV focussed to a spot size of 0.8 mm (vertically) by 0.8 mm (horizontally). On ID32 the incident x-ray beam (energy = 22.2 keV) was collimated to a spot size of 40 μm (vertically) by 0.3 mm (horizontally) and the scattered x-ray beam was detected after reflection from a graphite analyzer crystal. The horizontal sample surface was aligned with the x-ray beam for a fixed incidence angle of 0.2º and the diffractometer is operated in a six circle configuration. The thin film electrochemical cell was also used for these experiments, however, as the cell maintains a horizontal geometry in the 6-circle mode, no polypropylene film was used to trap the electrolyte and a thick electrolyte layer (~3 mm) covers the crystal surface. This is easily penetrated by the 22.2 keV x-ray beam and allows *in-situ* x-

ray measurements in an ideal electrochemical environment, i.e. it is more suited to study the kinetics of the growth process. CTR data were obtained by performing rocking scans around the surface normal at successive L values to obtain background-subtracted integrated intensities at each L position. During the x-ray measurements the outer chamber of the x-ray cell was continuously purged with nitrogen to protect the surfaces from oxygen. The reference electrode Ag/AgCl was used in the x-ray cell and for some cyclic voltammetry measurements. The reference electrode Hg/Hg_2SO_4 (mercury sulphate electrode or MSE) was also used for cyclic voltammetry measurements.

For CO adsorption studies, the outer cell was filled with an overpressure of CO (99.999% purity) which is able to diffuse through the polypropylene film (if present) and the electrolyte and saturate the surface (saturation of the electrolyte and surface was confirmed by cyclic voltammetry during dissolution of the Co deposit as the presence of adsorbed CO shifts the dissolution potential anodically [unpublished work by P. Allongue and F. Maroun]). In order to compare the effect of the applied electric field on the magnetic properties for the 2.2 ML thick Co film in CO-saturated electrolyte (Figure 6.1), the scattered x-ray intensity was measured both at key points on the specular CTR and on the scattering due to the Co film as the potential was cycled over the range -0.95 V to -1.4 V (vs MSE). In order to perform this measurement the electrolyte was exchanged to a solution free of Co ions so as to prevent further Co deposition at the negative potentials.

6.3 Cyclic Voltammetry and Co Film Growth

The cyclic voltammetry (CV) of Au(111) in 10 mM $CoSO_4$ + 10mM K_2SO_4 + 1mM H_2SO_4 + 0.1mM KCl (pH ~4) is shown in Figure 6.2. Two main negative peaks are observed at –1.25 V and –1.45 V and a single positive peak at ~ –0.8 V (vs MSE). The negative peaks correspond to the growth of the first Co bilayer on Au (–1.25 V) and the growth of Co on the bilayer (–1.45 V). The positive peak corresponds to Co

dissolution. The broad shoulder more positive than –1.25 V corresponds to H^+ reduction into H_2. Similar voltammograms are obtained in 1mM Co^{2+} except that the more negative peak is less well-defined. In order to determine the deposition rate, the potential was held at –1.25 V for a range of times from 0s (seconds) to 160s. The deposited film was then stripped, and the thickness of the Co layer calculated from the charge associated with the dissolution peak using the equivalence charge to thickness of 0.59 mC/cm^2 per monolayer of Co [5] (the deposition charge is mainly due to H^+ reduction). The thickness versus time curve is shown in Figure 6.3 and indicates two distinct growth rates; the faster rate between 0 and 2 ML and a slower rate when the film thickness is above 2ML. This was repeated for a range of potential steps more negative than -1.25V and it was found that the latter (slower) rate increases with decreasing the deposition overpotential and saturates at ~ –1.4 V.

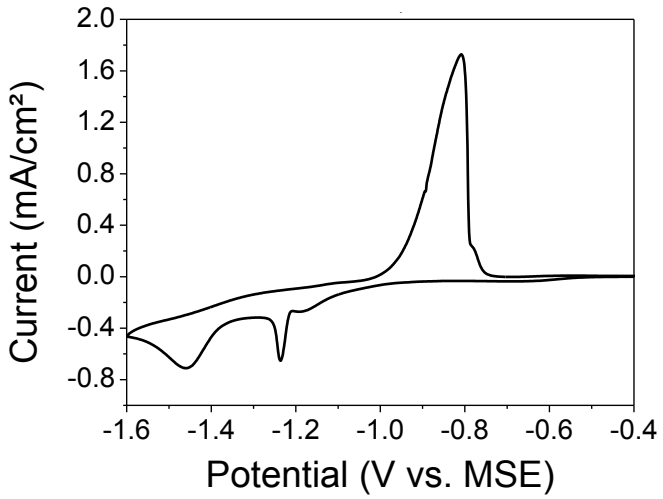

Figure 6.2 Cyclic Voltammetry of Au(111) in 10 mM $CoSO_4$ + 10mM K_2SO_4 + 1mM H_2SO_4 + 0.1mM KCl (vs MSE) [unpublished work by P. Allongue and F. Maroun].

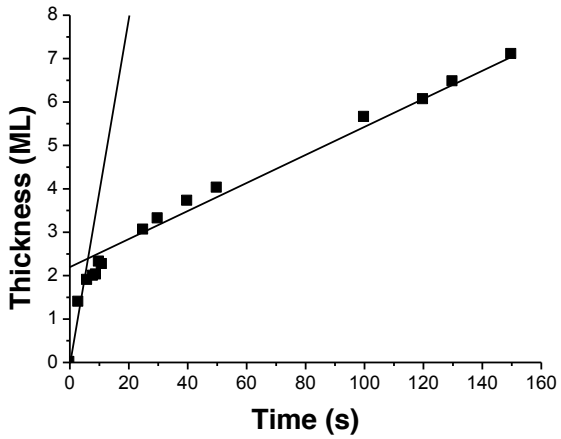

Figure 6.3 Co thickness in monolayers as a function of the deposition time for Co UPD in 0 mM $CoSO_4$ + 10mM K_2SO_4 + 1mM H_2SO_4 + 0.1mM KCl at -1.4 V (vs MSE) [unpublished work by P. Allongue and F. Maroun].

Structural information obtained from STM can be correlated with the CV results in Figure 6.2 and Figure 6.3. Figure 6.4 shows representative STM images, recorded by Allongue et al. [3], during the initial stages of Co growth on Au(111). The Au(111) surface is reconstructed in the potential range at which Co deposition occurs, the reconstructed surface being clearly evident in Figure 6.4. Previous studies have shown that the reconstruction is lifted upon deposition of Co [7]. Co nucleation on the Au(111) surface is potential dependant, for example at -1.3 V (vs MSE) the Co starts by nucleating at the Au steps as shown in Figure 6.4 and alternatively at -1.6 V growth occurs homogenously on the Au terraces [2]. The nuclei thickness corresponds to two atomic monolayers. The nuclei grow laterally and covers almost completely the Au substrates before the third Co monolayer start growing. Further Co growth is essentially layer-by-layer. The growth of the first bilayer is two dimensional and the STM images indicate that all islands are biatomic in height [5]. Hexagonal close packed (hcp) Co(0001) has a lattice parameter of 2.51 Å [16, 17], where as the Au(111) surface nearest-neighbour spacing (a_{NN}) is 2.88 Å [16, 17]. Previous analysis of STM images have shown that this lattice mismatch results in a Co film which is strained by 4.4% (2.61 Å) when a bilayer is deposited and 2.5% (2.57 Å) if there is a third layer of Co present [5].

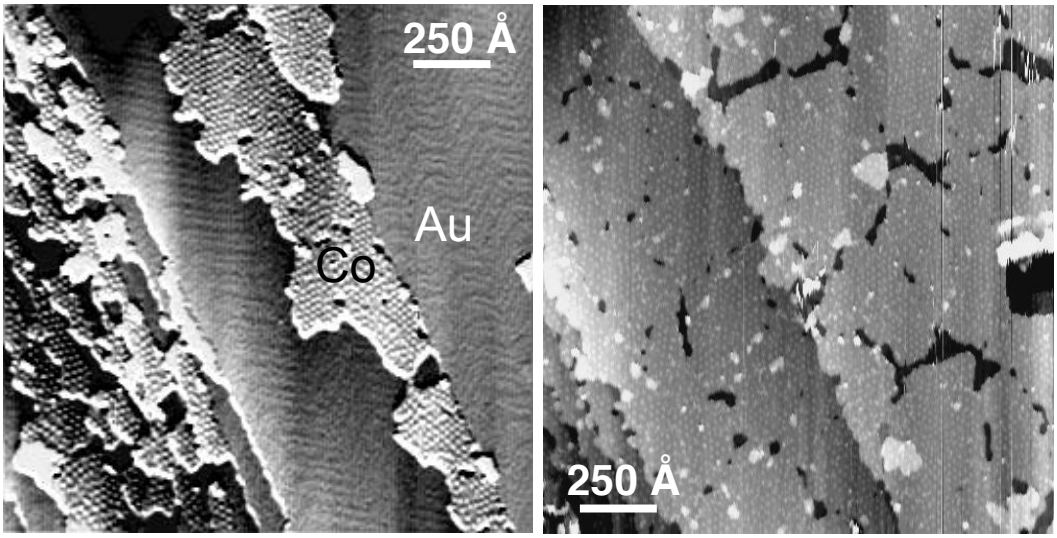

Figure 6.4 In situ scanning tunnelling microscopy (STM) images showing the morphology of Co/Au(111) layers deposited in a 10 mM Co^{2+} solution at pH = 4 at a potential of -1.3V vs MSE. STM images reprinted from Surface Science, 603, Allongue P., Magnetism of electrodeposited ultrathin layers: Challenges and opportunities, 1831-1840, Copyright (2009), with permission from Elsevier.

The CV and STM data can also be compared to in-situ SXS measurements of the Co growth. As previously mentioned the Co film grows with a lattice parameter that is different from the underlying Au lattice (and strained with respect to bulk Co). As a result scattering from the Co film is separated from that due to Au in any non-specular measurements. If the lattices of Au and Co are coincident, i.e. there is no rotation between them, then scattering due only to the Co film is expected to be observed along the [H, 0, L] direction (through the (1, 0, L) position) where the value of H determines the relative in-plane lattice parameter of the Co film. This is illustrated schematically in Figure 6.5 in which the surface plane of reciprocal space around the (1, 0, L) position has been used to indicate where scattering from the bulk Au substrate, the Au surface reconstruction and the Co film arises. The position of the Co peak was found to vary depending on the film thickness and resulting film strain, details of which will be given in Section 6.4, but was found to be between (1.121, 0, L) and (1.128, 0, L) for a Co bilayer.

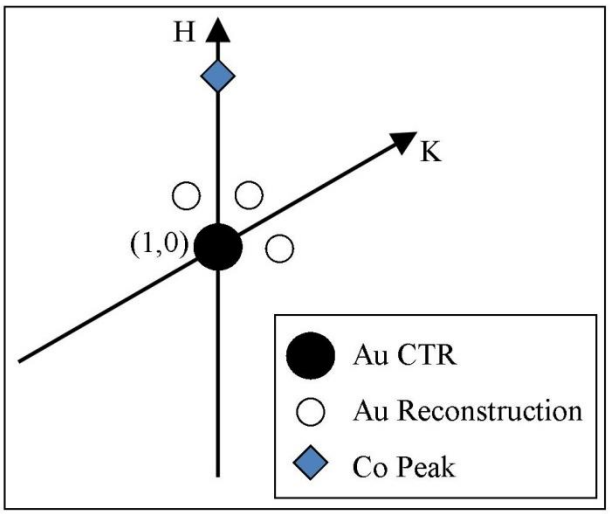

Figure 6.5 Schematic showing the surface region of the reciprocal lattice around the (1, 0, 0.3) CTR position indicating where scattering from the Au surface reconstruction and the deposited Co layer are observed.

Monitoring the scattering from the Co peak position and other key reciprocal space positions whilst Co is being deposited can be used to determine the rate of growth of the Co layer and to confirm how many layers of Co have been deposited. Measurements of the intensity at non-specular position corresponding to the Co peak (1.126, 0, 1.7) and specular position (0, 0, 1.185) are shown in Figure 6.6 as a function of the Co deposition time (for a deposition potential of -1.4 V). At (0, 0, 1.185), as shown in Figure 6.6(a), the intensity drops during Co deposition and reaches a minimum after ~7 seconds of growth whereupon it begins to increase again. At (1.126, 0, 1.7), as shown in Figure 6.6(b), although the scattered intensity increases continuously during Co deposition (as expected as this position is sensitive to Co growth), there is a clear shoulder after ~7 seconds of growth. These features at ~7 seconds of growth indicate that this is the point at which a 2 monolayer thick Co film is completed (which is confirmed by CTR measurements in section 6.4). Thus the SXS measurements in Figure 6.6 are consistent with the CV and STM data shown in Figure 6.2 and Figure 6.4. Although the scattering due to the Au surface reconstruction was not monitored during Co deposition, scans performed through the Au reconstruction position, (1.018, 0.018, L), immediately

after Co deposition (of 7 seconds), indicate that the reconstruction has been completely lifted.

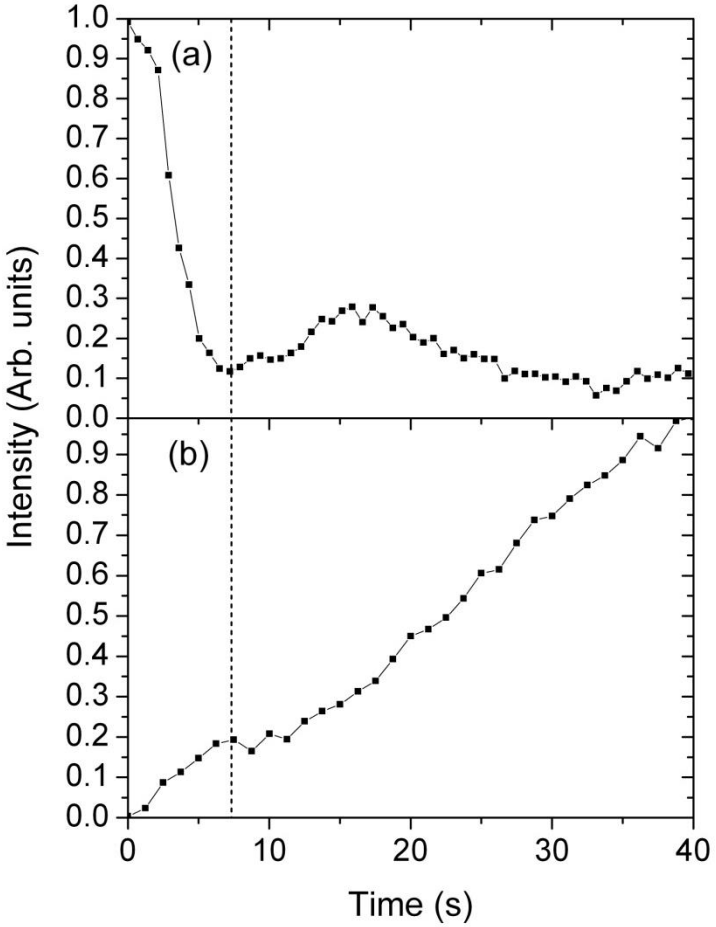

Figure 6.6 Scattered x-ray intensity measured at (a) (0, 0, 1.185), a position on the specular CTR and (b) (1.126, 0, 1.7), a position where scattering from the Co film is expected measured as a function of Co deposition time at -1.4 V.

6.4 Co Thin Film and Interface Structure

A detailed description of the atomic structure of the thin electrodeposited Co films can be obtained by surface x-ray diffraction. This can be acquired by measuring the scattering from the Co film which is separated from the scattering due to the underlying bulk Au substrate due to the different lattice constant of the Co film. This gives information about the lattice strain and orientation of the crystalline Co

lattice with respect to the Au lattice. The Co films (detailed in this section) were formed by holding the potential at -1.4 V (for the period of time described in the text) followed by stepping the potential to -1.15 V, i.e. between the potentials of Co deposition and stripping shown in Figure 6.2, at which the Co film is stable. Figure 6.7 shows the x-ray scattering measured along the [H, 0, 1.7] reciprocal space direction, i.e. approximately in the surface reciprocal space plane for increasing Co deposition times. A peak due to the (1, 0, L) crystal truncation rod (CTR), which arises due to the truncation of the Au(111) lattice at the surface, occurs at H=1 and the data shown have been background corrected by subtracting the intensity measured prior to Co deposition. Due to the lattice mismatch between Au and Co, the scattering due to the Co film occurs at the position shown. Rocking scans through the peak indicating that the Co film is perfectly aligned with the underlying Au lattice, i.e. the peak is not rotated with respect to the [H, 0, 0] direction. After 40s of Co deposition the Co peak is located at H = 1.128, which corresponds to an in-plane lattice constant of a = 2.556 Å which is expanded by ~1.8% compared to the bulk Co lattice constant (2.51 Å). As the thickness of the deposited film decreases the peak shifts to lower H values indicating a more strained Co film. For 7 seconds of Co deposition which, according to the CV results and supported by SXS measurements in Figure 6.6, corresponds to a 2 ML thick Co film, the Co peak is located at H = 1.121 giving an in-plane lattice constant a = 2.572 Å, corresponding to a lattice strain of ~2.5% compared to bulk Co.

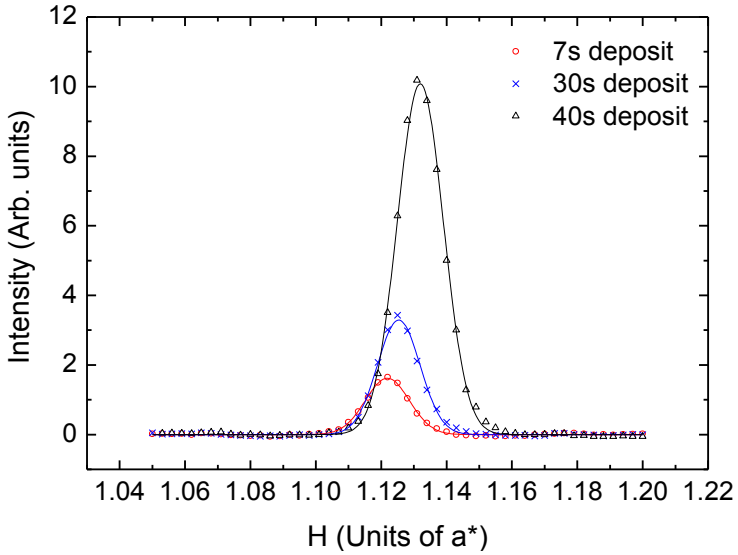

Figure 6.7 Scans measured along the <H, 0, 1.7> direction for different times of Co deposition. A scan measured before Co deposition has been subtracted from the data.

The structure of the 2 ML thick Co film was probed in detail: The out of plane structure of the Co film can be probed by measuring the L dependence of the Co peak at (1.121, 0, L) combined with a measurement of the specular CTR, (0, 0, L), from the underlying Au lattice. The specular CTR is sensitive only to layering along the surface normal direction and does not require the Co film to be commensurate with the Au lattice. In Figure 6.8 and Figure 6.9, which show the measured intensity along (1.121, 0, L) and (0, 0, L) respectively, the data points correspond to background subtracted integrated intensities obtained by performing rocking scans at each L position. The specular CTR data in Figure 6.9 shows clear oscillations which are consistent with a Co film thickness of ~2 monolayers. In fact the form of the specular CTR data can explain the intensity dependence measured at (0, 0, 1.185) during Co deposition (Figure 6.6 (a)). For a 2 ML thick Co film the minimum in the intensity along the specular CTR is close to this position. A 3 ML thick Co film would exhibit two oscillations between the Bragg reflections and hence the increase in intensity in Figure 6.6 (a) can be attributed to the growth of the third Co layer which is completed after ~17 s of Co deposition confirming the slower growth rate of Co after completion of the 2 ML thick Co film.

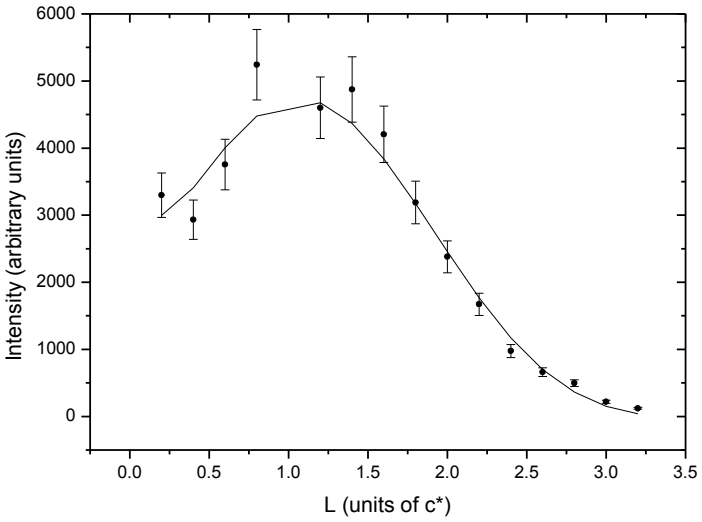

Figure 6.8 X-ray data measured along [1.121, 0, L] probing the surface normal structure of the 2 monolayer thick Co film. Data points are background-subtracted integrated intensities obtained from rocking scans at each L position. The solid line is a fit to the data as discussed in the text.

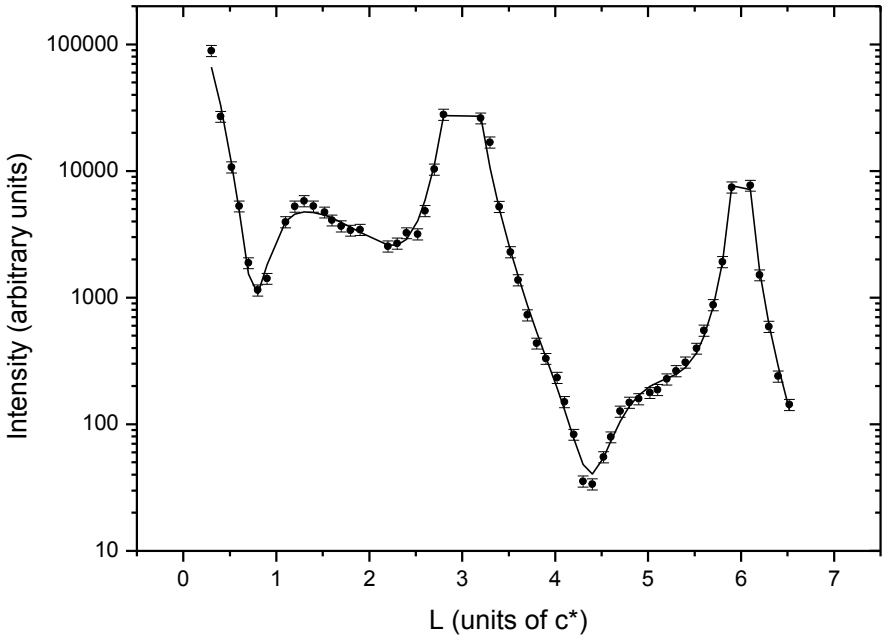

Figure 6.9 Specular CTR data, (0, 0, L), measured after 7 seconds of Co deposition (2 ML film). Data points are background-subtracted integrated intensities obtained from rocking scans at each L position. Data was measured in the thin film electrochemical cell on the XMaS beamline (BM28).The solid line is a fit to the data as discussed in the text.

The solid lines in Figure 6.8 and Figure 6.9 are a simultaneous fit to the data according to a structural model which includes up to 3 Co layers on top of the Au(111) surface. The parameters for the best fit are shown in Table 6.1. It should be noted that several independent preparations of the 2 ML Co film (i.e. different growth cycles) were made and that the results shown in Figure 6.8 and Figure 6.9 are representative examples. Fits to all of the measured data were performed and quality of the fits was similar to that shown in Figure 6.8 and Figure 6.9. In order to represent the full data set, the error bars given in Table 6.1 correspond either to the statistical error or to the variation in the results obtained from different growth preparation (the larger value is quoted in each case). The results indicate that a nearly perfect 2 monolayer thick Co film has been formed on the Au(111) surface and give information about the lattice relaxations along the surface normal direction. Given that measurements of the in-plane Co lattice parameter indicate that the film is significantly expanded relative to the bulk Co-Co spacing due to the large lattice mismatch between Au and Co, it might be expected that the Co film would be compressed along the surface normal direction. The results in Table 6.1, however, indicate that this is not the case. The reconstruction of the Au surface is lifted and the Au surface atoms are expanded outwards by ~2% of the Au(111) lattice spacing. According to a hard sphere calculation assuming the occupation of 3-fold hollow surface Au sites, the Au-Co surface normal spacing should be 2.195 Å (bulk constants) or 2.14 Å (using the in-plane Co-Co distance). The value for the surface normal Au-Co distance is 2.16 Å which is in between these values. It should of course be noted that the mismatch between the Co film and the Au substrate means that Co should occupy a range of surface Au sites. The Co-Co distance in the thin film is expanded by ~5% compared to the c axis lattice spacing in *hcp* bulk Co. At the electrode potential at which the measurement is performed it is expected that the surface may be covered by adsorbed hydrogen. There are currently no experimental studies of the hydrogen-induced lattice relaxation on Co(0001) surfaces. However, in a theoretical study of hydrogen chemisorption on Ni(111) and Co(0001) [18] a hydrogen-induced lattice expansion at the Co(0001) surface in

the range 4-7% is proposed and this is consistent with our experimental results. Finally it is noted that the 3rd partially occupied Co layer in the structural model is at an unrealistically small distance (1.65 Å) from the surface of the 2 monolayer Co film. Given that the specular CTR is only probing order along the surface normal direction, this component is tentatively assigned to some ordering in the electrochemical double layer rather than a partially occupied third atomic layer of Co. This is discussed in more detail in section 6.5 which describes the adsorption of CO onto the thin Co film.

θ_{Au1}= 1.0f	$d_{Au2\text{-}Au1}$=2.407 Å	σ_{Au1}= 0.13 Å
θ_{Co1}= 1.0	$d_{Au1\text{-}Co1}$= 2.157 Å	σ_{Co1}= 0.04 Å
θ_{Co2}= 1.0	$d_{Co2\text{-}Co1}$= 2.136 Å	σ_{Co2}= 0.31 Å
θ_{Co3}= 0.25	$d_{Co3\text{-}Au2}$= 1.65 Å	σ_{Co3}= 0.14 Å

Table 6.1 Parameters to the best fit shown by the solid lines in Figure 6.8 and Figure 6.9

6.5 CO Adsorption

The effect of CO adsorption on the Co thin film structure was probed in several SXS experiments. Figure 6.10 shows the results of an experiment in which Co was deposited for 7 seconds (nominally a 2 ML thick film) and, after characterization, CO was added to the electrolyte as described in section 6.2. As this measurement was made on the ID32 diffractometer, there is a limited range of the specular CTR that can be accessed due to the limited range of incident angle. The specular CTR data measured before (red squares) and after (black circles) saturation of electrolyte with CO, is shown in Figure 6.10 (a) together with a calculated fit to the data which gave similar structural parameters to those obtained from the more extended CTR data set in Figure 6.9. The ratio between the two data sets is shown in Figure 6.10 (b); plotting the ratio highlights any systematic changes that have

occurred due to the adsorption of CO onto the Co film. In addition to the measurements shown in Figure 6.10, the scattering due to the Co film was also measured in the form of H scans (such as Figure 6.7), rocking curves through the Co peak at (1.121, 0, 0.3) and scans along the [1.121, 0, L] direction, such as the data shown in Figure 6.8, but measured directly in an L scan after background subtraction. Interestingly the adsorption of CO caused no measureable change in any of the scattering due only to the Co film. This indicates that there is no significant change in the strain in the Co film induced by the adsorption of CO and that the changes in the magnetic properties are not driven by structural rearrangement in the Co thin film. This will be discussed in more detail below. The only measureable change in the SXS experiment due to adsorption of CO is the small change to the specular CTR data as shown in Figure 6.10 (b). The systematic change can be seen in the ratio data set in Figure 6.10 (b). Although the limited data set precludes analysis to the level of detail shown in the section 6.4, a similar structural model was used to calculate the solid lines shown in Figure 6.10 in an attempt to determine the main effect of CO adsorption. The calculated solid line shown in Figure 6.10 (b) is obtained with a reduction in the outward expansion of the surface Co layer and a change in the 3rd Co layer which had previously been assigned to be due to ordering in the electrochemical double layer. Although it is difficult to provide a definitive analysis of the results, it is clear that the adsorption of CO may reduce the outward expansion in the thin Co film (probably due to the replacement of adsorbed hydrogen by CO) with an accompanying rearrangement of the structure in the electrolyte adjacent to the Co film. This is discussed in section 6.7.

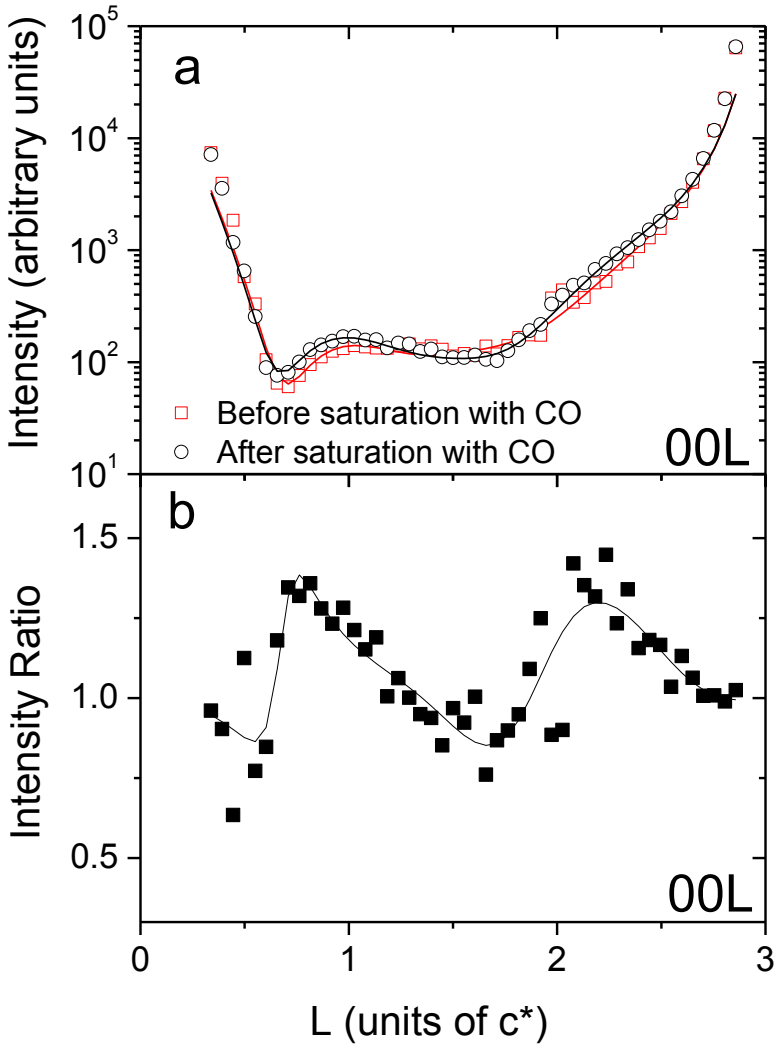

Figure 6.10 (a) Specular CTR (0, 0, L) data for a 7 seconds Co deposition on Au(111) before (red squares) and after (black circles) saturation with CO. (b) The ratio of the CTR data after saturation with CO / before saturation with CO. The solid lines are fits to the data as discussed in the text.

6.6 Co dissolution

Following each deposition experiment the potential was cycled anodically to strip the Co film and the CV of this process was recorded. An example of the CV is shown by the black line in Figure 6.11, the dissolution peak occurring at -0.94 V and the broader peak at -0.76V due to the H_2 oxidation current. Simultaneously, XRV

measurements were made at [1.126, 0, 1.7], a reciprocal space position sensitive to the Co deposit, to further characterise the dissolution process. As the potential is scanned anodically, the intensity is initially high and stable, it then falls suddenly at around -0.65 V suggesting that the Co structure is no longer present.

An intriguing fact shown in Figure 6.11 is that the x-ray signal (XRV - red line) systematically vanishes at a potential more positive than the dissolution peak shown in the CV (black line). This suggests that the transfer of charge across the surface is occurring prior to the Co structure being removed from the surface, which is not possible. However, since the CV corresponds to the current from the majority of the sample surface (any areas in contact with electrolyte) and alternatively the x-ray signal corresponds to a small fraction of the crystal surface on which the x-rays are incident (~ 2.5 % or 0.02 cm^2), one plausible explanation is that, the presence of the x-rays stabilise the portion of the Co film they are incident on.

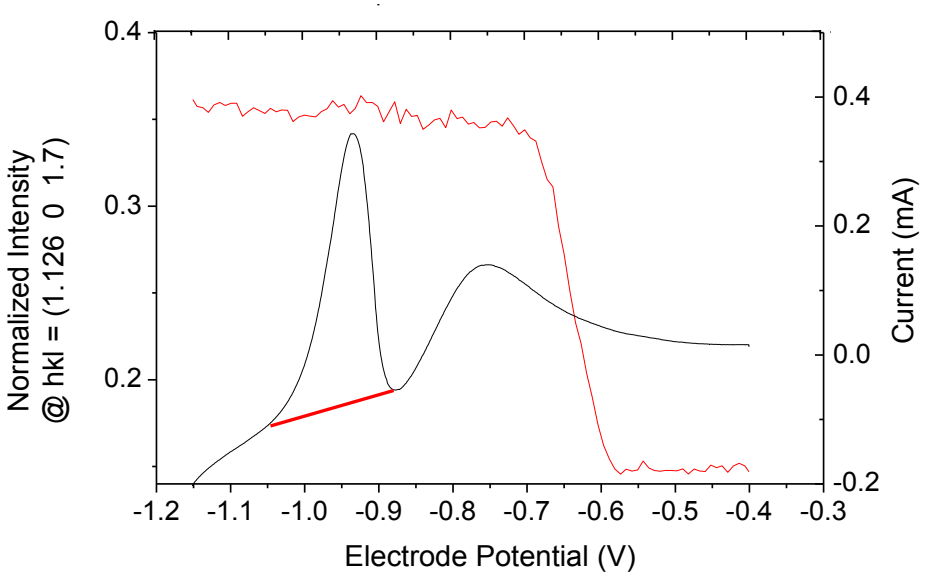

Figure 6.11 XRV (red) and CV (black) recorded simultaneously. This shows a significant difference in potential of stripping of Co due to the presence of the x-ray beam on a small fraction of the sample.

6.7 Summary

The principle aim of the experiments described in this chapter was to attempt to link the atomic structure in the Co thin films electrodeposited onto Au(111) with the magnetic properties, particularly with relation to the CO-induced change in magnetization in films which are thicker than one Co monolayer. The electrodeposition of the Co films was monitored in-situ, both by STM and SXS. The results indicate that the Co film grows initially as a bilayer, i.e. 2ML thick as confirmed by the STM images (Figure 6.4) and the SXS signals measured at two reciprocal space positions (Figure 6.6). From the location of the x-ray scattering peak due to the deposited Co (Figure 6.7), in the surface plane of the Au reciprocal lattice, the in-plane strain for a 2 ML thick Co film is ~2.5% ($a = 2.572$ Å) compared to bulk Co ($a = 2.51$ Å). Detailed characterization of the thin film structure, performed by analysis of the specular CTR which probes the surface normal structure across the Au(111) electrolyte interface, revealed a small outward expansion in the Co film by ~2% of the Au(111) lattice spacing which may be caused by the presence of adsorbed hydrogen on the Co surface.

Following CO adsorption on the Co films the SXS results indicate that there are only very small changes in the atomic structure at the surface of the Co film. In particular the adsorption of CO has no effect at all on the in-plane lattice strain of the Co film, which is entirely due to the lattice mismatch with the underlying Au substrate. There is some evidence that there is a slight reduction in the outward expansion of the surface Co layer and this may be due to the partial replacement of adsorbed hydrogen with CO. No potential dependence was found at any position where the scattering was uniquely due to the Co film. The intensity measured at one position on the specular CTR, (0, 0, 0.4), showed a linear and reversible dependence on the applied potential although the measured changes over the entire potential range were only ~5% of the measured signal. At higher values of L the potential dependent changes in the scattered intensity were significantly

smaller. It can be concluded, therefore, that the potential dependence of the magnetic behaviour (shown in Figure 6.1) is driven by subtle changes in the electrolyte double layer region adjacent to the Co surface. The SXS measurements imply that some surface sites are blocked by the adsorption of CO and it may be that the potential dependent effect is due to the incorporation of solvated cation species into the outer Helmholtz plane. The measurements certainly indicate that the changes in the magnetic behaviour are driven by a surface process associated with the surface charge and not by any structural rearrangement in the Co film.

6.8 References

[1] F.J. Himpsel, J.E. Ortega, G.J. Mankey, R.F. Willis, Adv Phys, 47 (1998) 511-597.
[2] P. Allongue, F. Maroun, Mrs Bull, 35 (2010) 761-770.
[3] P. Allongue, F. Maroun, H.F. Jurca, N. Tournerie, G. Savidand, R. Cortes, Surf Sci, 603 (2009) 1831-1840.
[4] P. Allongue, F. Maroun, Electrocrystallization and Nanotechnology, Wiley, Weinheim, (2006).
[5] P. Allongue, L. Cagnon, C. Gomes, A. Gundel, V. Costa, Surf Sci, 557 (2004) 41-56.
[6] P. Prod'homme, F. Maroun, R. Cortes, P. Allongue, J. Hamrle, J. Ferre, J.P. Jamet, N. Vernier, J Magn Magn Mater, 315 (2007) 26-38.
[7] P. Allongue, F. Maroun, Curr Opin Solid St M, 10 (2006) 173-181.
[8] N. Tournerie, A.P. Engelhardt, F. Maroun, P. Allongue, Phys Rev B, 86 (2012).
[9] T. Maruyama, Y. Shiota, T. Nozaki, K. Ohta, N. Toda, M. Mizuguchi, A.A. Tulapurkar, T. Shinjo, M. Shiraishi, S. Mizukami, Y. Ando, Y. Suzuki, Nat Nanotechnol, 4 (2009) 158-161.
[10] K. Nakamura, R. Shimabukuro, Y. Fujiwara, T. Akiyama, T. Ito, A.J. Freeman, Phys Rev Lett, 102 (2009).
[11] D.M. Kolb, Prog Surf Sci, 51 (1996) 109-173.
[12] K. Itaya, Prog Surf Sci, 58 (1998) 121-247.
[13] C.A. Lucas, N.M. Markovic, Interfacial Kinetics and Mass Transport, in: E.J. Calvo (Ed.) Encyclopedia of Electrochemistry, vol. 2, Wiley, Weinheim, (2003).
[14] C.A. Lucas, N.M. Markovic, Advances in Electrochemical Science and Engineering, Wiley, Weinheim, (2006).
[15] C.A. Lucas, N.M. Markovic, In-Situ Spectroscopic Studies of Adsorption at the Electrode and Electrocatalysis, Elsevier, Oxford, (2007).
[16] B. Cullity, Elements of X-ray Diffaction, 3rd ed., Prentice Hall, Upper Saddle River, N.J., , 2001.
[17] W.B. Pearson, Handbook of Lattice Spacings and Structures of Metals and Alloys, Pergamon, London, 1958.
[18] D.J. Klinke, L.J. Broadbelt, Surf Sci, 429 (1999) 169-177.

Chapter 7:

Co-modified Au(111) in Alkaline Electrolyte

7.1 Introduction

Improving the efficiency for electrochemical transformation of water to molecular hydrogen is of increasing importance to meet the growing use of hydrogen as an energy storage medium and for industrial applications. Water-alkali electrolysers and chlor-alkali electrolyers are currently the main sources of electrolytically produced hydrogen and key to both these systems is the electrocatalysis of the hydrogen evolution reaction (HER). However the main barriers to use are the high overpotential for the HER and the stability of the catalyst, making the whole process energy intensive and expensive. The HER is split into two stages, the first being water dissociation, $H_2O \leftrightarrow H + OH^- + e^-$, and the second hydrogen adsorption (H_{ad}) and recombination to H_2 together with the adsorption of OH^-. Although Pt and Pt-group metals offer the highest activity for the HER, they are limited by the first

stage of water dissociation. Alternatively, metal oxides are effective as catalysts for water dissociation. Combining the two materials by depositing metal oxides on metal substrates creates bi-functional systems which have optimised properties. Previous studies have found that $Ni(OH)_2$-Pt, $Co(OH)_2$-Pt(111) and $Co(OH)_2$-Au(111) surfaces enhance the activity for hydrogen evolution but additional research into the structures and sites that catalyse the activity is needed to further develop these catalysts [1-3].

In this chapter electrochemically deposited thin films of Co were transferred to alkaline electrolyte and CV, SXS and atomic force microscopy (AFM) techniques used to probe the resulting Co-modified Au(111) surface structure. Upon transfer to alkaline electrolyte electrodeposited Co islands on the Au(111) surface are oxidised to $Co(OH)_2$. The underlying Au(111) surface is also re-ordered by the presence of the Co islands forming a compressed hexagonal Au reconstruction. The Co-modified Au(111) surface was found to shift the potential of hydrogen evolution in alkaline electrolyte by at least + 0.1 V compared to clean Au(111).

7.2 Experimental Methods

The Au(111) crystal was prepared as described in Section 3.2 and transferred to the hanging meniscus cell contained 1mM$CoSO_4$ in supporting electrolyte 10mM K_2SO_4 + 1mM H_2SO_4 + 0.1mM KCl (pH ~ 4) for the deposition of Co on Au(111) surface. For some initial measurements a Pt wire counter electrode was used but, in later measurements, a Co wire counter was used to prevent the possibility of Pt deposition on the Au(111) surface. The Co deposition process will be discussed in detail in Section 7.3. Once the Co layers were formed the crystal was rinsed with ultrapure water and then transferred to the electrochemical 'thin-layer' x-ray cell with a drop of ultrapure water protecting the surface and immersed at open circuit potential into nitrogen purged alkaline electrolyte, 0.1 M KOH, in order to study the Co-modified Au(111) electrode. The outer chamber of the 'thin-layer' x-ray cell was

continuously purged with nitrogen to protect the surface from oxygen. The cyclic voltammetry measurements were performed in a hanging meniscus cell with the same sample preparation, nitrogen purged electrolytes and nitrogen atmosphere. The reference electrode used was leak free Ag/AgCl versus which all potentials are quoted and an Au wire counter electrode was used for all experiments in alkaline electrolyte. All Au and Pt wires were flame annealed in a butane flame and rinsed in ultrapure water before use and the Co wire counter electrode was prepared by etching in dilute nitric acid and rinsing in ultrapure water.

X-ray measurements were performed on beamline BM28 (XMaS), the UK-CRG beamline at the ESRF, Grenoble and on beamline I07, at the Diamond Light Source, Oxfordshire. Focused incident x-rays of energy 11 keV were used at beamline I07 and the electrochemical 'thin-layer' x-ray cell was mounted on the hexapod on the (2+3)-circle diffractometer with surface normal horizontal. In addition to standard surface diffraction measurements, resonant surface x-ray scattering (SXS) measurements were also performed, on beamline BM28, by scanning the incident x-ray energy through an atomic absorption edge whilst maintaining fixed diffraction conditions. Specifically energy dependant measurements were made by scanning ± 0.1 keV of the following energies; 7.709 keV (Co K edge), 11.564 keV (Pt L_{III} edge) and 11.919 keV (Au L_{III} edge). From these measurements it is possible to gain elemental specificity in the diffraction experiment whilst simultaneously measuring the fluorescence in the near edge x-ray absorption fine structure (NEXAFS) region. This will be discussed in detail in Sections 7.5 and 7.6. On beamline BM28 the electrochemical 'thin-layer' X-ray cell was mounted on the goniometer with the sample normal vertical and the Huber diffractometer was used in 4-circle mode.

7.3 Formation of Co Layer(s)

The deposition of Co from 1mM $CoSO_4$ + 10mM K_2SO_4 + 1mM H_2SO_4 + 0.1mM KCl electrolyte was discussed in section 6.3. Similar cyclic voltammetry (CV) to that

shown in Figure 6.2 is shown in Figure 7.1, however in Figure 7.1 the CV was performed over a smaller potential range to avoid bulk deposition of Co on the Au(111) surface. In Figure 7.1 the potential is cycled cathodically at a scan rate of 50 mV/s from 0 V to -0.84 V (vs Ag/AgCl), the latter being the potential for the deposition of the first Co bilayer with subsequent layer by layer growth of Co. The potential was then held at -0.84 V for a range of times from 0 s (seconds) to 500 s before cycling anodically. An anodic peak due to the dissolution of Co is shown in Figure 7.1, the potential of which is dependent on the deposition time. From the charge associated with the dissolution peak the number of Co monolayers deposited can be calculated (charge to thickness of 0.59 mC/cm^2 per monolayer of Co) [4]. The broad shoulder shown more positive than -0.8 V corresponds to H^+ reduction into H_2.

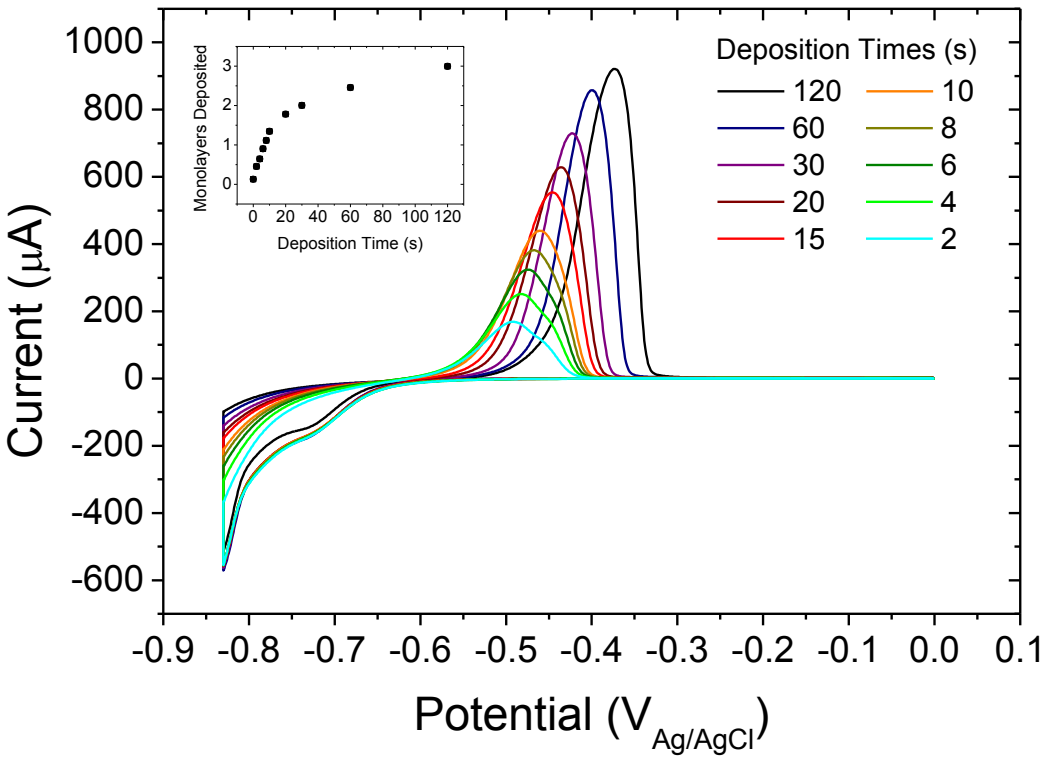

Figure 7.1 Cyclic Voltammetry of Au(111) in 1mM Co^{2+} solution at pH = 4 recorded at a sweep rate of 50 mV/s using Pt counter electrode (vs Ag/AgCl). The applied potential was held at -0.84 V for varying lengths of time from 0 to 120s resulting in a change in the quantity of Co deposited/stripped as indicated.

Initial measurements were performed using a Pt wire counter electrode, however due to later findings (see section 7.4) it was necessary to ensure that there was no contamination of the modified Au(111) electrode due to the presence of Pt ions in the electrolyte, i.e. dissolved from the counter electrode. After consideration of alternatives for electrochemical cleanliness and stability it was concluded that Co wire may be the most suitable option. Carbon and Au wire were also considered but Carbon is difficult to clean and the dissolution of Au would lead to the presence of Au ions in solution which would interfere with the Co deposition. Figure 7.2 shows the CV obtained using the Co wire counter electrode, all other experimental details remained the same. The profile is very similar except for the shoulder due to the reduction of H^+ which is less pronounced. The Co deposition rate was found to be the same for both counter electrodes, with a 200 s deposit corresponding to ~3 ML (monolayers with respect to Co(0001)).

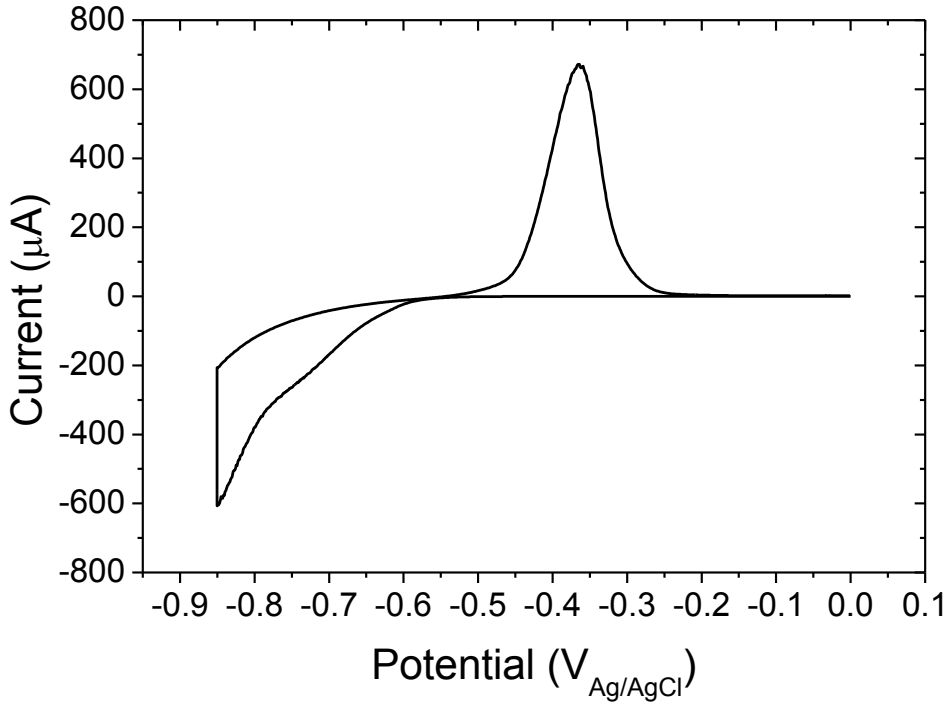

Figure 7.2 Cyclic Voltammetry of Au(111) in 1mM Co^{2+} solution at pH = 4 recorded at a sweep rate of 50 mV/s using a Co counter electrode (vs Ag/AgCl).

The next stage was to transfer the Co-modified Au(111) electrode into alkaline electrolyte. Initially 2 ML of Co were deposited in order to form Co films very similar to those investigated in Chapter 6, however such a thin deposit was found to be unstable upon transfer. To overcome this problem an alternative method for the Co film formation was developed for the experiments contained within this Chapter. First ~4 ML of Co were repeatedly (10 times) deposited and stripped by scanning the potential cathodically to - 0.84 V and holding at -0.84 V for 300 seconds before scanning anodically back to 0.0 V. Following the final deposition of ~4 ML of Co (at -0.84 V), the potential was scanning anodically back to ~-0.7 V, a potential negative of the Co stripping peak, and the contact with the electrolyte (meniscus) broken. The surface of the electrode was immediately covered with ultrapure water before transferring to alkaline electrolyte either in a hanging meniscus cell for CV measurements or in an electrochemical 'thin-layer' x-ray cell for x-ray diffraction.

7.4 Cyclic Voltammetry in Alkaline Electrolyte

The deposition method described in the previous section was followed prior to transfer of the Co-modified Au(111) electrode to a hanging meniscus cell containing nitrogen purged 0.1 M KOH in order to study the electrochemical behaviour using CV. Figure 7.3 show the CV for the Co-modified Au(111) surface together with that of clean Au(111) surface (black line) in 0.1 M KOH (vs Ag/AgCl with Au wire counter electrode as previously stated). The blue lines are from a Co-modified Au(111) surface with possible Pt contamination (Pt counter used in deposition of Co) and the red lines are from a Co-modified Au(111) surface without Pt contamination (Co counter used in deposition of Co). On the clean Au(111) surface the hydrogen evolution reaction (HER) occurs at potentials negative of -1.2 V as shown in Figure 7.3 (H1). For the Co-modified Au(111) electrode the potential for HER has been shifted > + 0.1 V as shown in Figure 7.3 (a) (H2). It would be expected that the presence of Pt would cause this effect, hence the experiment

was repeated without any possibility of Pt contamination, to see if Co catalyses hydrogen evolution, which it appears to do (H3). In a recent publication Sheng *et al.* found a correlation between the HER activity in 0.1 M KOH and the hydrogen binding energy on monometallic surfaces [5]. The HER for Co was found to be 0.2 V positive to that of Au. A similar shift in the potential for hydrogen evolution was found for Pd on Au(111) electrode in acid electrolyte [6].

The other features shown in the CV in Figure 7.3 for the Co modified Au(111) crystal are similar to those found in previous studies by Foelske *et al.* of Polycrystalline Co and Co(0 0 0 1) in 0.1 M NaOH [7, 8]. Figure 7.4 shows the CV for Polycrystalline Co in 0.1 M NaOH [7]. There are three potential regions indicated on the CV which correspond to different passive layers being formed/reduced on the Co surface. Hydrogen evolution occurs at potentials negative of -1.2 V vs SHE (-1.4 V vs Ag/AgCl). Oxidation peaks A1, A2 and A3 and reductions peak C1/2 and C3 are due to the transitions from metallic species Co(0) to oxidised species Co(II) and Co(III). For the sub-potential range of oxidation (SPR) (A1) a thin $Co(OH)_2$ film covers the surface. For the range of primary passivity, between A2 and A3, the passive layer consists of a pure $Co(OH)_2$, the thickness of which is dependent on potential and time. Positive of A3, the range of secondary passivity, Co(III) dominates due to Co_3O_4 and CoOOH formation. In-situ SXS data presented in this chapter was taken within or negative of the region of primary passivity. As a result it is expected that the Co present will be in the metallic or oxidised Co (II) state.

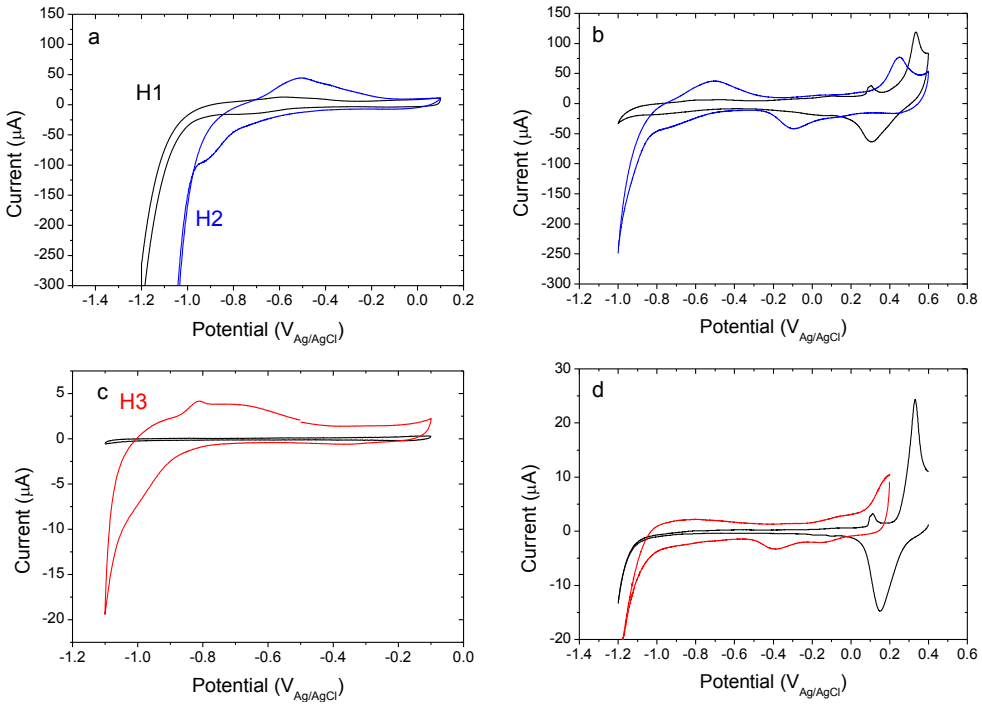

Figure 7.3 Cyclic Voltammetry of Au(111) (black lines) together with (a and b) Co-modified Au(111) with possible Pt contamination (blue lines) and (c and d) without Pt contamination (red lines) in 0.1 M KOH (vs Ag/AgCl). (a,b and c) were recorded at a sweep rate of 50mV/s and (d) at a sweep rate of 20mV/s.

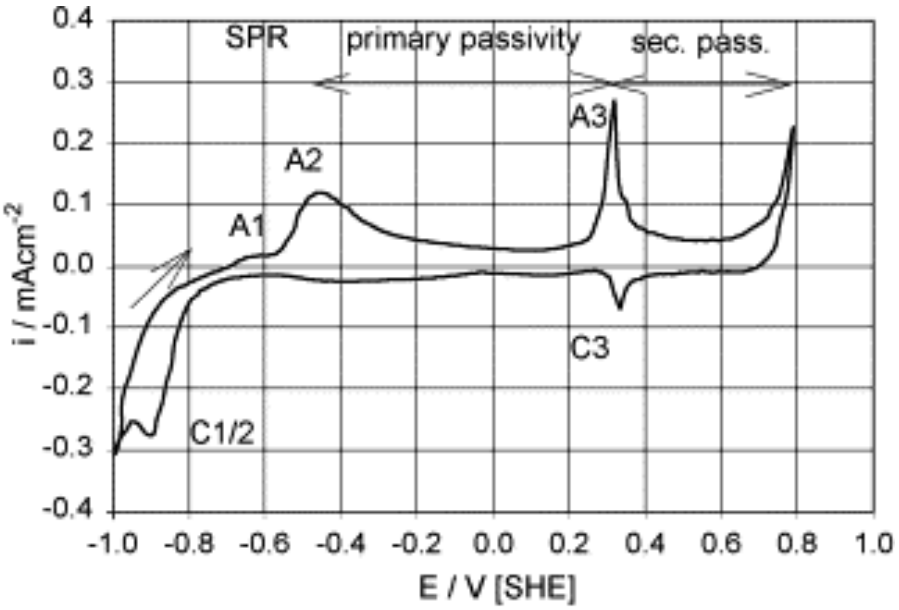

Figure 7.4 CV of polycrystalline Co in 0.1 M NaOH, scan rate 5mV/s. Reprinted from Surface Science, 554, Foelske A. et al., Initial stages of hydroxide formation and its reduction on Co(0 0 0 1) studied by in situ STM and XPS in 0.1 M NaOH, 10-24, Copyright (2004), with permission from Elsevier. [7]

7.5 Cobalt Structure

To study the structure of the cobalt on the Au(111) surface and the effect of immersion into alkaline electrolyte, atomic force microscope (AFM) images were performed ex-situ and SXS measurements were performed in situ to characterize the Co-modified Au surface.

7.5.1 AFM Images

Ex-situ AFM images were made in order to gain an understand of the size, height, location, shape and coverage of the Co structures that were present after the Co-modified Au(111) electrode was transferred to alkaline electrolyte. The deposition and transfer to alkaline electrolyte was performed as described in sections 7.2 and 7.3 following which the Co-modified Au(111) electrode was held at - 0.9 V for 30 minutes, removed from the electrolyte, rinsed with ultrapure water and dried using N_2 gas before imaging. By using this method it is possible to get a realistic image of the Co-modified Au(111) surface that would be present in the CV and SXS measurements. Figure 7.5 shows a typical AFM image of the Co-modified Au(111) surface (Pt free) performed in air. The AFM imaging reveals that islands of Co nucleate at the step edges of the Au(111) surface as shown in Figure 7.5 and Figure 7.6. Figure 7.6 also shows height profiles of the Co islands. The Co islands cover, on average, ~2.2% of the Au(111) surface. A range of Co islands are observed with an average diameter = 500 Å ± 200 Å and height = 185 Å ± 70 Å. Given that a nominally 4 ML thick Co film was deposited in the growth cycle, it is rather surprising that the Co islands are so large. This result, together with the fact that the island coverage is only ~2% implies that large Co islands are formed on top of the thin Co film during the deposition process. During transfer to alkaline electrolyte (during which potential contact is broken) it appears that the thin Co film strips from the surface and only the Co islands remain.

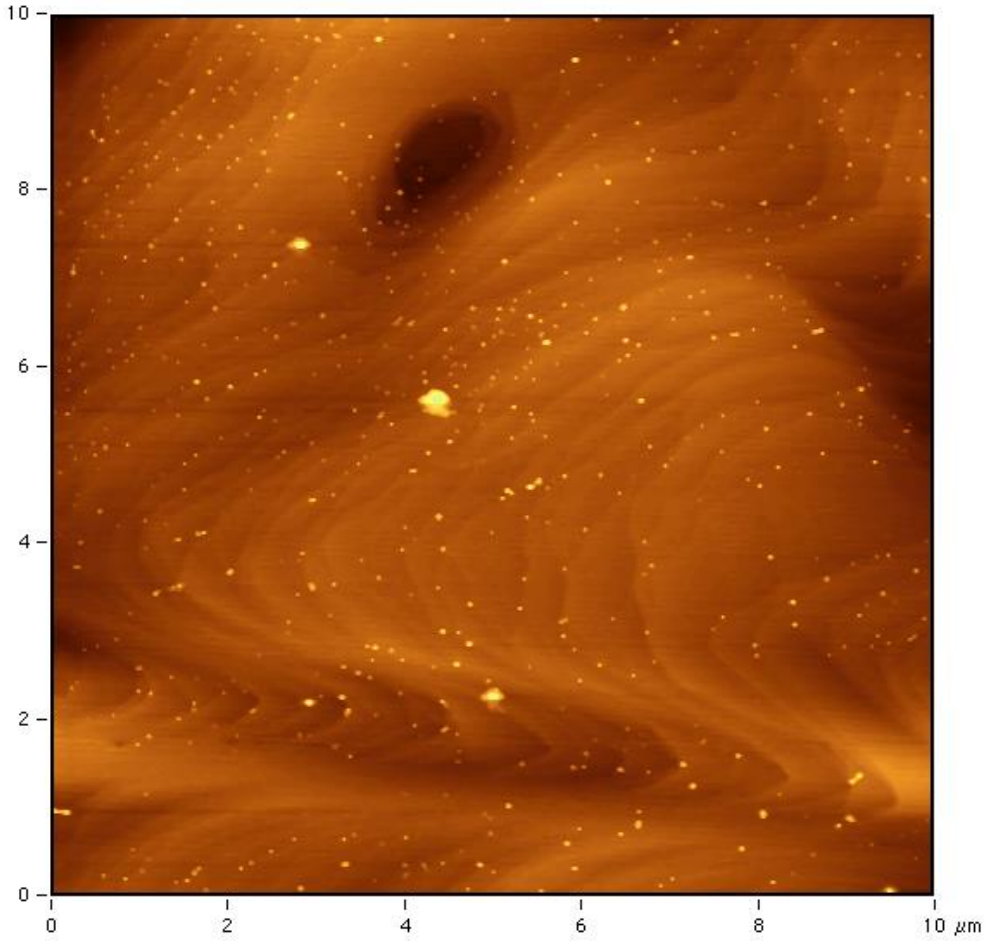

Figure 7.5 Typical 10 x 10 µm AFM image of Co-modified Au(111) surface. The Co islands nucleate at the step edges of the Au(111) surface.

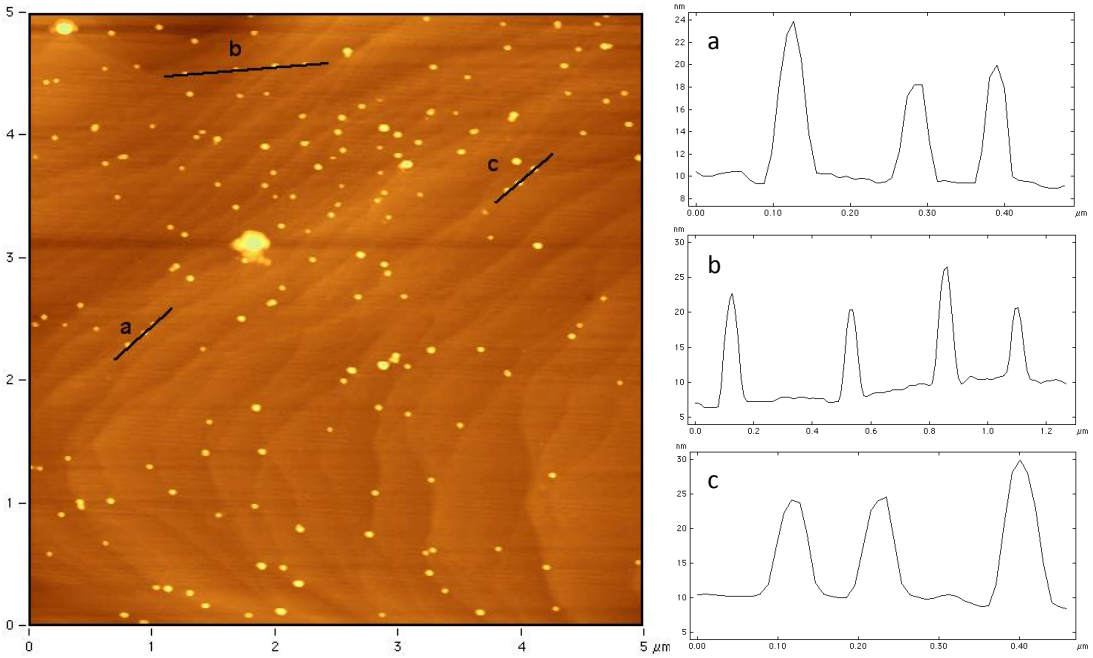

Figure 7.6 Typical 5 x 5 µm AFM image of Co-modified Au(111) surface together with height profiles (a, b and c) through Co islands as indicated on the image.

7.5.2 X-ray Diffraction

The Au(111) crystal was re-prepared, Co deposited on the surface and the sample transferred to a 'thin-layer' x-ray cell containing nitrogen purged 0.1 M KOH as described in sections 7.2 and 7.3. Changes to the Au surface structure that are caused by Co deposition will be discussed separately in Section 7.6. In addition to the fixed incident energy measurements (standard SXS) which have been used throughout this thesis, such as CTR and XRV, resonant surface x-ray scattering was also utilised to probe the elemental composition and charge state of both the Co and Au surface structures. The resonant SXS measurements are described in section 7.5.3. In this section fixed incident energy measurements, CTR and XRV, are discussed.

Figure 7.7 shows the specular (0, 0, L) CTR for the Co-modified Au(111) crystal in 0.1 M KOH measured at -0.6 V. Compared to the CTR measured from a clean

Au(111) surface (chapter 4) there is clearly additional scattered intensity in between the Bragg reflections which must be due to scattering from the Co deposit. Furthermore, there appears to be a weak oscillation (between L=1 and L=3) that would be consistent with a bilayer Co deposit. As the specular CTR is only sensitive to layering along the surface normal direction, the Co islands observed in the AFM measurement will make a contribution to the measured scattering and it is impossible to derive a unique structural model to describe this data.

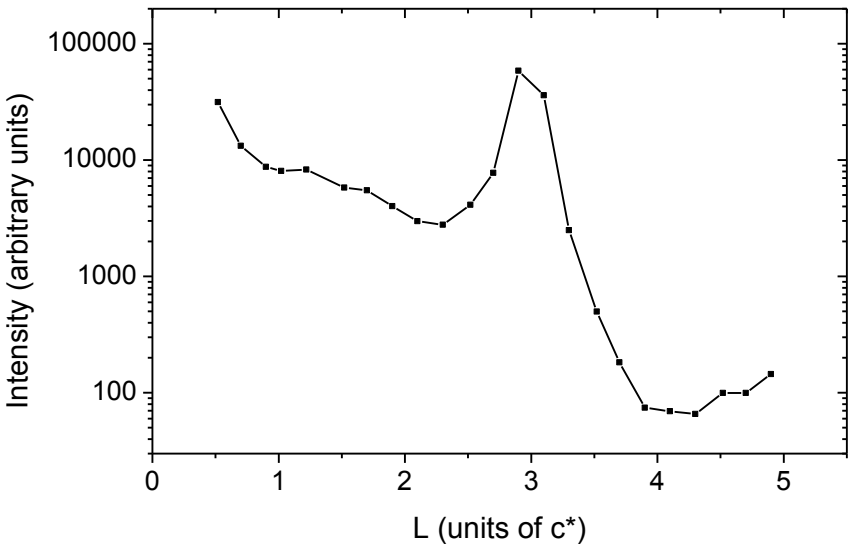

Figure 7.7 Specular CTR (0, 0, L) CTR for the Co-modified Au(111) crystal in 0.1 M KOH measured at -0.6 V (vs Ag/AgCl).

XRV measurements, made at positions along the (0, 0, L) CTR and at (1, -1, 0.2), are shown in Figure 7.8. The specular anti-Bragg position, (0, 0, 1.5) is sensitive to ordering in the electrode surface and electrolyte side of the interface. Interestingly the change in intensity seen here is opposite to that seen for clean Au(111) for which the scattering is reduced at positive potential due to the lifting of the Au surface reconstruction. The positions (0, 0, 2.7) and (0, 0, 3.3) are sensitive to surface relaxation. These two positions mirror each other, an increase in intensity at (0, 0, 2.7) (decrease in intensity at (0, 0, 3.3)) corresponds to an expansion of the surface. The potential response for surface expansion is very similar to that seen for a clean Au(111) electrode in 0.1 M KOH. This may be due to the fact that much

of the Au(111) surface is not covered by Co. The position (1, -1, 0.2) is close to a non-specular anti-Bragg position and is sensitive to interfacial atomic positions that are commensurate with the Au lattice. There is a small change here suggesting that the Au surface does not undergo significant restructuring as the potential is cycled.

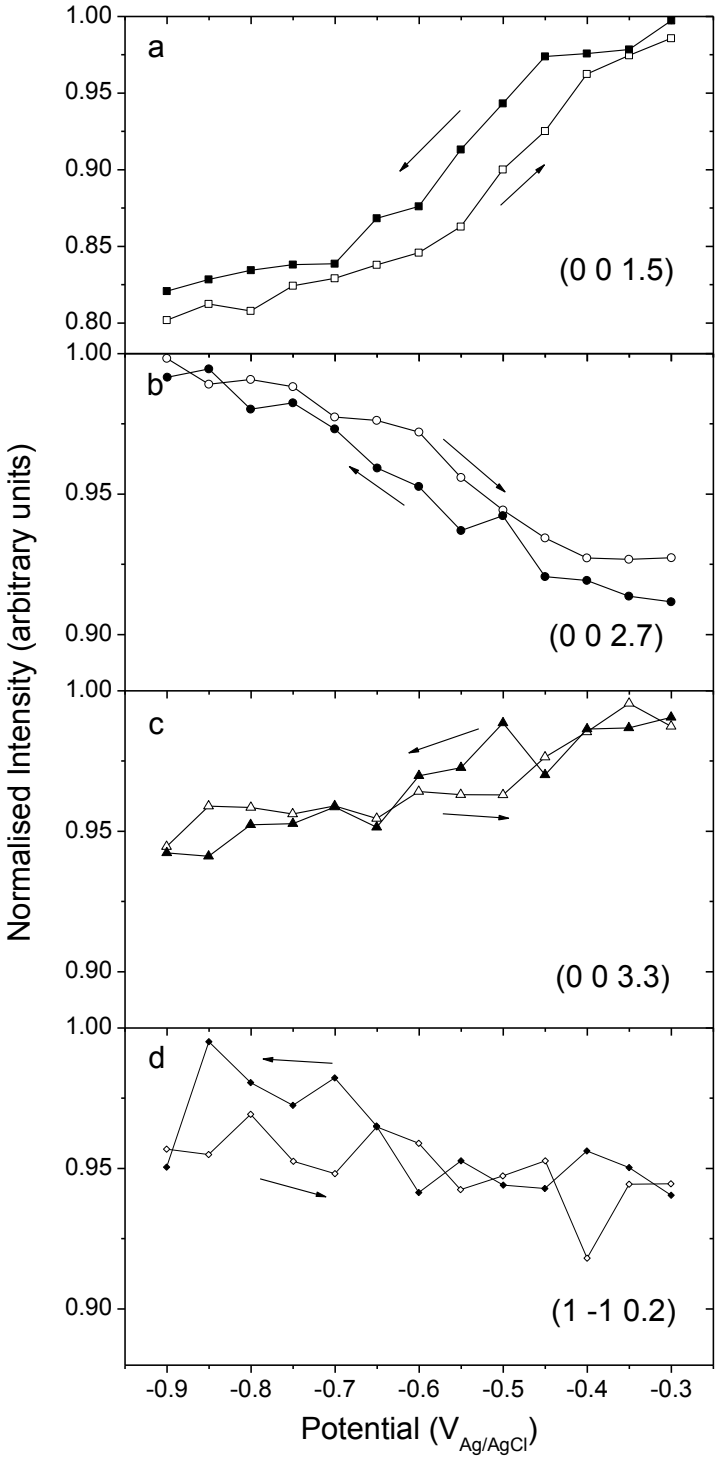

Figure 7.8 X-ray Voltammetry (XRV) for Co modified Au(111) in 0.1 M KOH at a sweep rate of 5 mV/s.

7.5.3 Resonant Surface X-ray Scattering

Once the CTR profile and potential dependence of the Co-modified Au(111) electrode had been established, resonant SXS measurements were performed by scanning the incident x-ray energy through an atomic absorption edge whilst maintaining fixed diffraction conditions. Resonant SXS allows element selective diffraction experiments, which can be useful in studying complex metallic surfaces [9]. Energy dependant measurements were made by scanning ± 0.1 keV of the Co K edge (7.709 keV) and Au L_{III} edge (11.919 keV). Resonant SXS (often called anomalous SXS) experiments involve scanning the incident x-ray energy through the absorption edge of an atom within the sample [10-13]. The atomic form factor of the particular atom being probed then needs to be corrected for the dispersion corrections, i.e.

$$f(\boldsymbol{q}, E) = f(\boldsymbol{q}) + f'(E) + \mathrm{i}\, f''(E) \qquad (7.1)$$

describes the corrected form factor $f(\boldsymbol{q}, E)$ which consists of 3 components; the atomic form factor $f(\boldsymbol{q})$ and the real and imaginary parts of the dispersion corrections $f'(E)$ and $\mathrm{i}\, f''(E)$.

In terms of physical measurements f'' is directly related to the absorption spectrum and can be obtained by measuring the fluorescent signal from the sample itself. In principle, f' can then be obtained by a Kramers-Kronig transformation [14]. Experimentally, a calibrated multi-channel analyser (MCA) detector is used to collect and separate the elastically scattered x-rays from the fluorescent background. By using a MCA both the elastic and fluorescent signals can be collected simultaneously during the same measurement. In general interpretation of resonant scattering data is rather complex and only a qualitative analysis of the data is presented here.

Resonance measurement were made at different L positions along the specular (0, 0, L) CTR. They are performed by picking an incident x-ray energy of one of the

binding energies of the atoms being investigated, for example the Co K-edge at 7.709 keV, and scanning the energy ± 0.1 keV of this energy. From the fluorescence signal information about the general chemical composition of the scattering atoms can be obtained, i.e. the equivalent of a NEXAFS experiment. The elastically scattered signal also contains spectroscopic information but the diffraction conditions mean that this is limited to the set of atoms that contribute to the diffracted signal.

Figure 7.9 shows measurements of the fluorescence from the Co-modified Au(111) electrode in 0.1 M KOH. Figure 7.9 (a) shows the change in fluorescence intensity as the energy is scanned through the Co K edge (measured at (0, 0, 0.52), note however that fluorescence is not a position sensitive measurement). The position of the absorption edge can be obtained by taking the 1^{st} derivative of the fluorescent signal. This produces a peak, the position of which corresponds to the binding energy of the atom emitting the fluorescence. Figure 7.9 (b) and (c) show the 1^{st} derivative of the fluorescent signal as a function of energy for the Co K edge and the Au L_{III} edge. The position of the Co K edge and the Au L_{III} edge are indicated by the dashed lines at 7.709 keV and 11.919 keV respectively. As is clear to see in Figure 7.9 (c) the Au L_{III} edge and peak in the 1^{st} derivative of the intensity coincide well (a Gaussian fit to this peak gives the centre of mass (COM) to be 11.917 keV ± 2 eV). This means that the Au is in an uncharged state as would be expected and the energy calibration is good. However in Figure 7.9 (b) the peak is positive of the Co K edge. A Gaussian fit to this peak gives a COM of 7.723 keV ± 2 eV which is 14 eV ± 2 eV positive of the Co K edge. This measurement is very sensitive to the charge state of the element present. The positive shift of the edge suggests that there is an increase in the oxidation state of the Co. The Co K-edge position is remarkably sensitive to its oxidation state as shown in previous studies of Co^{2+} and Co^{3+} [15, 16] and the fluorescent signal in Figure 7.9 is due to Co^{2+}. This is most likely present in the form of $Co(OH)_2$ [3] which is also suggested by the CV measurements described in section 7.4. Figure 7.9 (a) shows that as well as the

main fluorescence edge signal at 7.723 keV from $Co(OH)_2$ there is a small signal at the Co K edge (indicated by dashed line in the inset) suggesting that there is also Co present on the surface in its metallic form.

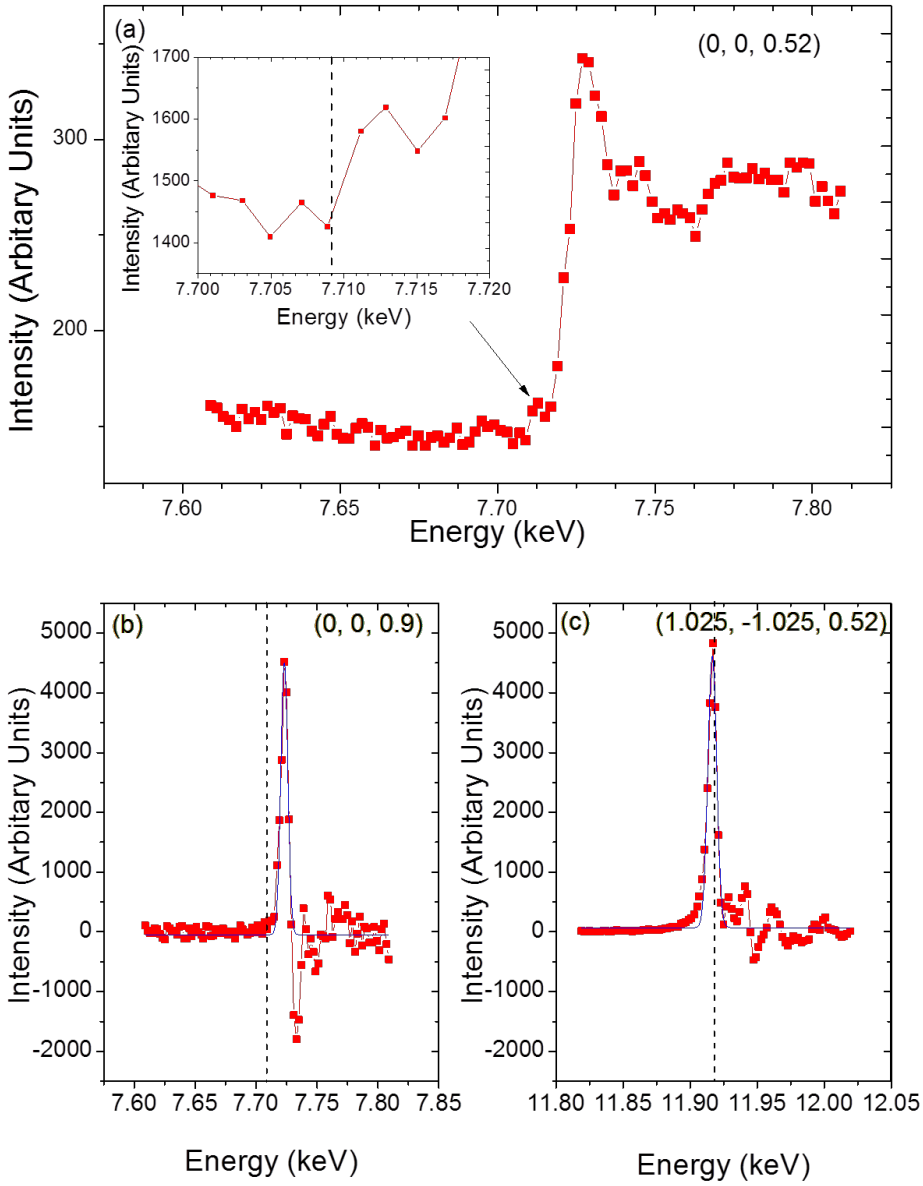

Figure 7.9 Measurement of the fluorescence intensity from Co-modified Au(111) electrode in 0.1 M KOH as a function of energy through the Co K-edge at (a) (0, 0, 0.52). 1st derivative of the fluorescence intensity as a function of energy through with inset showing a section in more detail (b) the Co K edge at (0, 0, 0.9) and (c) the Au L_{III} edge at (1.025, 1.025, 0.52). The dashed lines through (b) and (c) mark the Co K edge and Au L_{III} edge respectively.

Figure 7.10 shows the resonant surface x-ray scattering (the elastically scattered signal) measured at positions along the specular (0, 0, L) CTR. The background subtracted data shown in Figure 7.10 were obtained by subtracting two energy scans offset by ±2° from data measured at the specular position. The change in the intensity profile as a function of L suggests there is a change in phase of the scattering from the Co atoms relevant to the underlying Au substrate. This explains why the intensity increases at the edge at low L, but decreases at higher L values. At (0, 0, 1.52), however, the shape of the of the energy scan cannot be explained by a single resonance and indicates that there must be Co atoms in different oxidation states which gives rise to an interference pattern due to the relative shifts in the edge position. In combination with the fluorescent measurement shown in Figure 7.9 this implies that the Co atoms that are selected by the diffraction conditions may be present in both the metallic state and in hydroxide form.

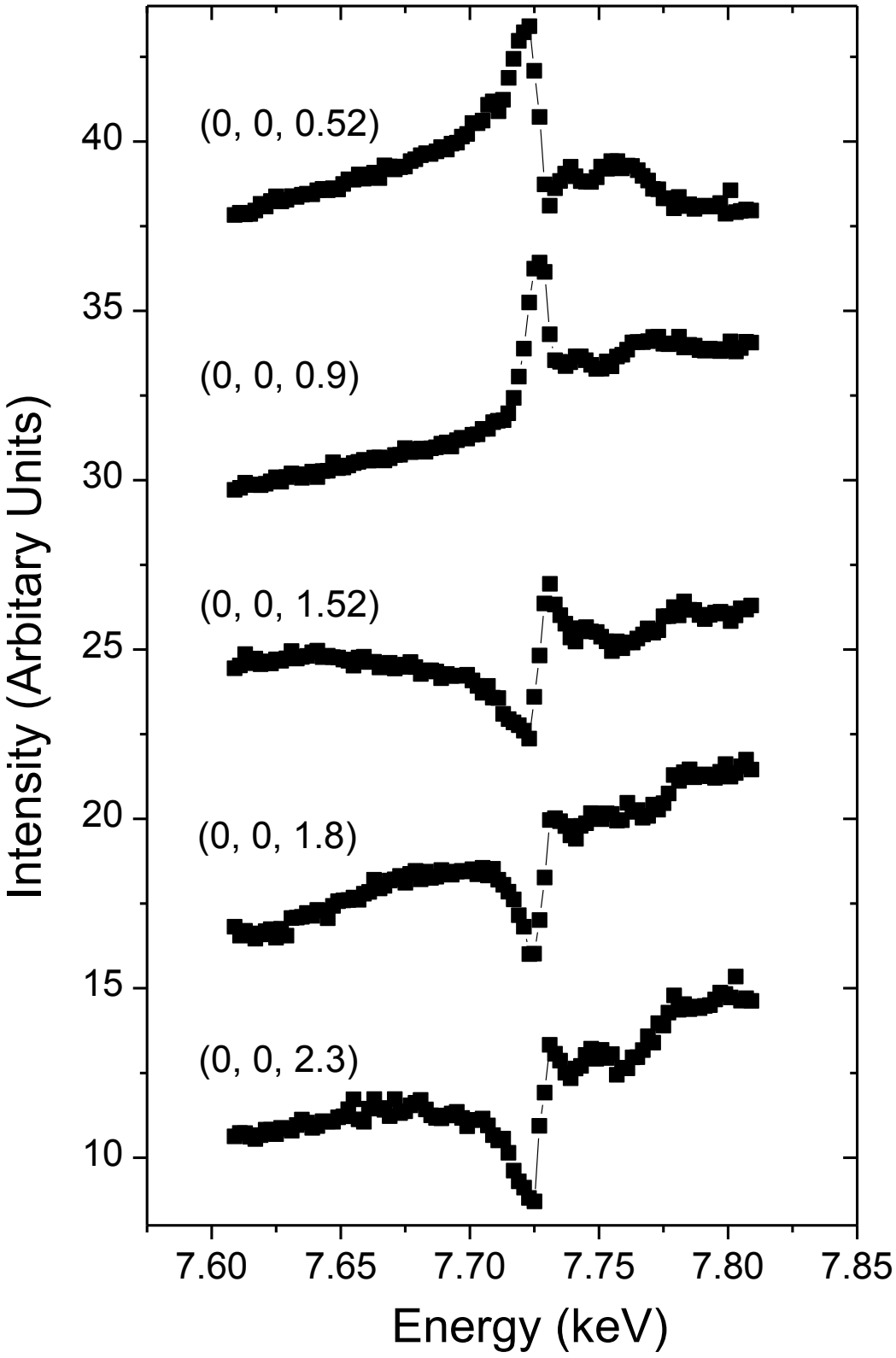

Figure 7.10 Resonant Surface X-ray Scattering as a function of energy at reciprocal space position along the (0, 0, L) CTR.

7.6 Modification of the Au Surface

During SXS studies of the Co-modified Au(111) crystal a peak at (1.025, -1.025, L) was observed. Figure 7.11 shows the preliminary measurements that were used to locate and understand the characteristics of this scattering feature. Figure 7.11 (a) and (b) shows hkscans (performed by scanning through the position in reciprocal space in the h and k direction noted here) in the [1 -1 0] and [0 1 0] directions through the (1 -1 0.2) and the (0 1 0.2) positions respectively. The sharp peak at 1 (h or k) is due to the CTR. Rocking scans, perpendicular to the scan direction in Figure 7.11 (a), were measured over both a narrow and extended range to probe the domain size and symmetry of the structure. The Gaussian fit to the data in Figure 7.11 (c) has a full width half maximum (FWHM) of 0.027 giving a domain size of 107 Å. Figure 7.11 (d) shows a wider scan in which the sample is rotated through 140° around the surface normal direction, the three peaks are separated by 60° and show that the structure has 60° symmetry. The peaks occur along each of the bulk in-plane hexagonal directions similar to those of the discommensuration fluid phase seen for Au(111) surface at temperatures greater than 880K in UHV [17]. Figure 7.11 (e) shows the intensity along the (1.025, -1.025, L) direction obtained by taking an rocking scans at each L position and then calculating the background-subtracted integrated intensity from this. The intensity as a function of L is essentially monotonic (the slope is due to the form factor decreasing with increasing L and changes in the beam footprint on the sample). This implies that the scattering is due to a single atomic layer. Finally Figure 7.11 (f) shows XRV at the (1.02, 0, 0.2) position and indicates that the structure that gives rise to this peak is unaffected by changes in the applied potential over the range -0.3 V to -0.9 V.

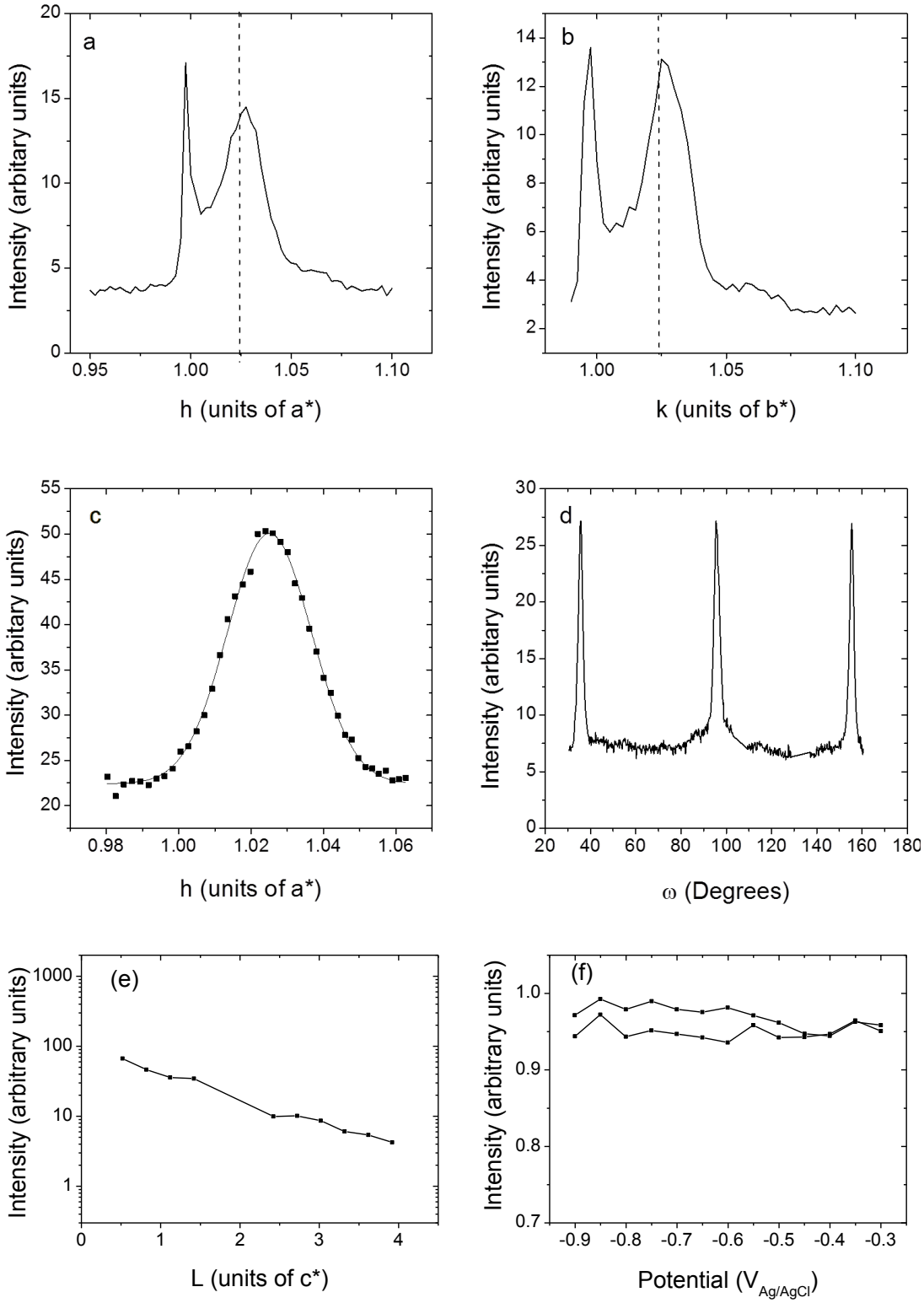

Figure 7.11 (a, b) hkscans in the [1 -1 0] and [0 1 0] directions through the (1, -1, 0.2) and the (0 1 0.2) positions respectively. (c) ω rocking scan through (1.025, -1.025, 0.2). (d) wide ω scan showing 60° symmetry. (e) Intensity along the (1.025, -1.025, L) direction. (f) XRV at (1.02, 0, 0.2).

Resonant SXS measurements were performed at (1.025, -1.025, 0.52) in order to probe the elemental composition of the structure that gives rise to the peak. Again these measurements were performed by scanning the incident energy through an atomic absorption edge whilst maintaining fixed diffraction conditions. Energy dependant measurements were made by scanning ± 0.1 keV of the Co K edge (7.709 keV) and Au L_{III} edge (11.919 keV). Figure 7.12 shows the background subtracted elastic signal (a) and (b) and the 1st derivative of the fluorescence (c) and (d) made at the (1.025, -1.025, 0.52) position. Figure 7.12 (a) and (c) are measurements ± 0.1 keV of the Au L_{III} edge and (b) and (d) are measurements ± 0.1 keV of the Co K edge. The fluorescence, which is just the scattering from all of the surface atoms, is completely consistent with the data shown in Figure 7.9. The elastic signal, however, is selecting the contributing atoms according to the diffraction conditions. Figure 7.12 (b) suggests there is no Co (in any charge state) contribution to the scattering at (1.025, -1.025, 0.52) whereas Figure 7.12 (a) shows that at the Au L_{III} edge a strong resonance is observed. Resonant and fluorescence measurements were also performed over the Pt L_{III} edge (11.564 keV) to check for a Pt contribution. There was evidence for Pt in the fluorescence measurements but not in the resonance measurements suggesting that, similarly to Co, Pt was present on surface but does not contribute to the scattering at (1.025, -1.025, 0.52). To summarise, the resonant SXS data show that the scattering at (1.025, -1.025, 0.52) is due only to Au and there is no contribution from Co or Pt. This information, together with the data in Figure 7.11, indicates that there is a compressed hexagonal Au surface reconstruction present when there are Co islands or partial coverage of Co on the Au(111) surface.

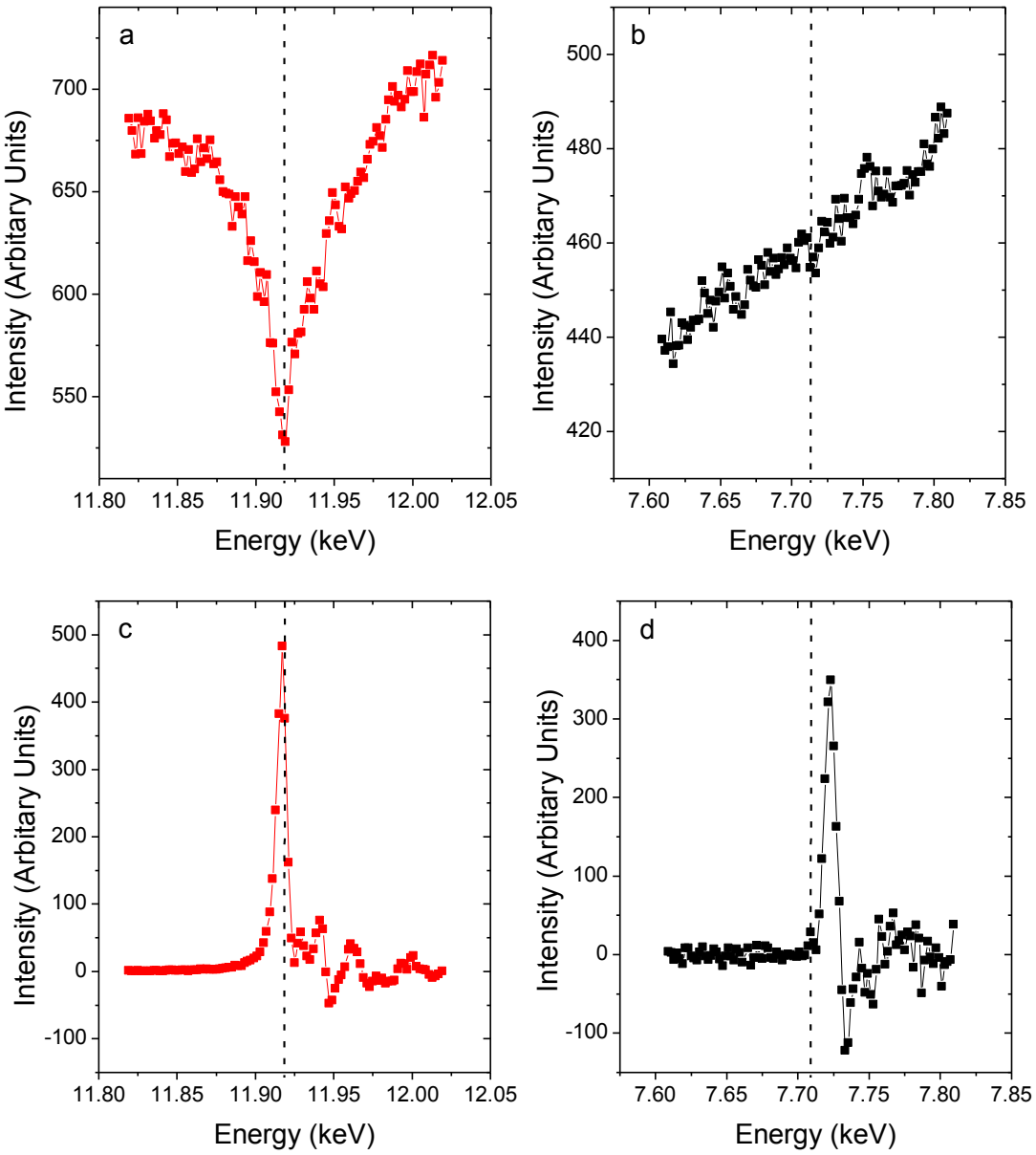

Figure 7.12 (a) and (b) are resonant surface x-ray scattering scans (the elastic signal) at the (1.025, -1.025, 0.52) reciprocal space position. (c) and (d) are 1st derivatives of fluorescence measured at the (1.025, -1.025, 0.52) reciprocal space position. (a) and (c) (in red) are through the Au L_{III} edge (indicated by dashed line) and (b) and (d) (in black) are through the Co K edge (indicated by dashed line).

7.7 Summary

Thin films of Co were deposited on a Au(111) electrode prior to transfer of the electrode to 0.1 M KOH. Ex-situ AFM imaging revealed that, after transfer to alkaline electrolyte, Co is present in the form of large islands which are located at the step edges of the Au(111) surface. These islands cover approximately 2.2% of the Au surface and contain Co in 2 different charge states. Their presence affects the underlying Au surface structure resulting in a modified reconstruction. Due to the complexity of the interface structure it is not possible to fit the CTR data and obtain a unique model as in previous chapters. However resonant SXS measurements, together with the other techniques used throughout this thesis, have enabled a good understanding of the surface properties. Fluorescence measurements indicate the presence of Co in a charged state, which is most likely $Co(OH)_2$, and also shows evidence of a small amount of metallic Co. Qualitative analysis of the resonant SXS (elastic signal) confirms the presence of Co in different charge states. There are two known structures of $Co(OH)_2$, β-$Co(OH)_2$ is most likely in a strong alkaline environment [18]. Considering all of the information a schematic of the Co islands is given in Figure 7.13 in which it is proposed that within the $Co(OH)_2$ islands there is ordered metallic Co.

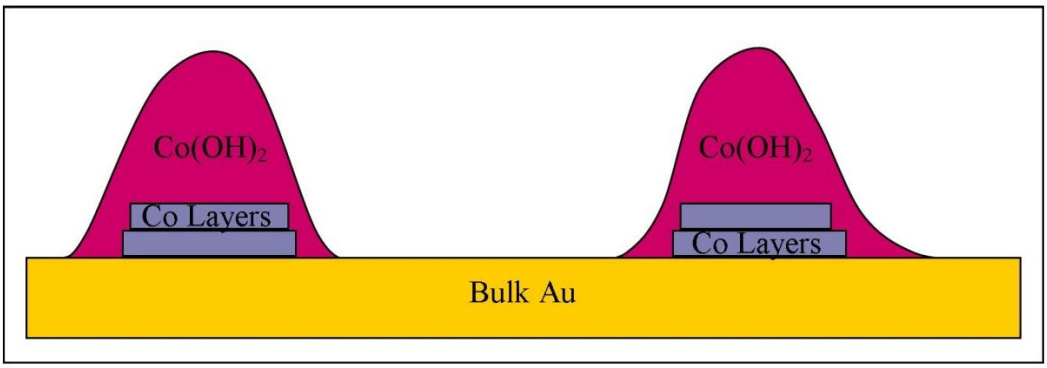

Figure 7.13 Schematic illustration of Co Layers with $Co(OH)_2$ islands on top.

During the diffraction measurements a peak at (1.025, -1.025, L) was seen. Initially this was thought to be due to the Co islands present on the surface, but further

resonant diffraction measurements showed that it is due to a surface Au reconstruction. It would appear that the presence of Co islands causes a modified reconstruction of the Au(111) surface, different to the Au(111) (23 x √3) reconstruction. The modified reconstruction showed no potential dependence in 0.1 M KOH over the range -0.3 V to -0.9 V (vs Ag/AgCl). The modified reconstruction was also present for a partially dissolved Co bilayer on the Au(111) surface in acid electrolyte. The results imply that the reconstruction consists of a compressed hexagonal Au structure induced by the presence of Co islands and/or partial coverage of Co on the Au(111) surface. A potential explanation for the formation of the modified reconstruction may be inferred from the lattice mismatch between Au(111) (a_{NN} = 2.88 Å) and hcp Co(0001) (a_{NN} = 2.51 Å). In Chapter 6, SXS measurements revealed that a 2ML Co film on Au(111) is strained by ~2.5% to 2.57 Å. It is reasonable to propose that the Au(111) surface also compensates for the lattice mismatch by undergoing a compression and that, upon removal of the deposited Co layers, the remaining Co islands pin the compressed reconstruction in place.

Remarkably, although Co only covers ~2.2% of the Au(111) surface, its presence lowers the overpotential for the HER. CV measurements revealed that the potential for hydrogen evolution is shifted positively by ~0.1 V on the Co island-modified surface compared to clean Au(111). Schafer et al. found a similar shift in the electrocatalytic activity for the HER for incorporated Pd into the Au(111) surface in 0.1 M H_2SO_4 with Pd coverage as low as 0.006ML [6]. They suggest that enhancement of the catalytic activity for the HER might be related to the presence of mixed Au/Pd sites, where the hydrogen binding is not too strong or too weak for the overall HER [6]. Sheng *et al.* performed electrochemical measurements for a range of monometallic surfaces on the HER in 0.1 KOH. They found the HER for Co to be ~0.2 V positive to that of Au and slightly negative of that for Pd [5]. It is therefore feasible that mixed Au/Co sites on the Au(111) surface, formed due to the repeated deposition/stripping of Co on the Au(111) surface prior to transferring

the electrode to the alkaline electrolyte, are responsible for the enhancement of the HER.

7.8 References

[1] L.A. Kibler, Chemphyschem, 7 (2006) 985-991.
[2] R. Subbaraman, D. Tripkovic, D. Strmcnik, K.C. Chang, M. Uchimura, A.P. Paulikas, V. Stamenkovic, N.M. Markovic, Science, 334 (2011) 1256-1260.
[3] R. Subbaraman, D. Tripkovic, K.C. Chang, D. Strmcnik, A.P. Paulikas, P. Hirunsit, M. Chan, J. Greeley, V. Stamenkovic, N.M. Markovic, Nat Mater, 11 (2012) 550-557.
[4] P. Allongue, L. Cagnon, C. Gomes, A. Gundel, V. Costa, Surf Sci, 557 (2004) 41-56.
[5] W.C. Sheng, M. Myint, J.G.G. Chen, Y.S. Yan, Energ Environ Sci, 6 (2013) 1509-1512.
[6] P.J. Schafer, L.A. Kibler, Phys Chem Chem Phys, 12 (2010) 15225-15230.
[7] A. Foelske, J. Kunze, H.H. Strehblow, Surf Sci, 554 (2004) 10-24.
[8] A. Foelske, H.H. Strehblow, Surf Interface Anal, 34 (2002) 125-129.
[9] B. Fowler, C.A. Lucas, A. Omer, G. Wang, V.R. Stamenkovic, N.M. Markovic, Electrochim Acta, 53 (2008) 6076-6080.
[10] A. Menzel, K.C. Chang, V. Komanicky, H. You, Y.S. Chu, Y.V. Tolmachev, J.J. Rehr, Radiat Phys Chem, 75 (2006) 1651-1660.
[11] E.D. Specht, F.J. Walker, Phys Rev B, 47 (1993) 13743-13751.
[12] Y.S. Chu, H. You, J.A. Tanzer, T.E. Lister, Z. Nagy, Phys Rev Lett, 83 (1999) 552-555.
[13] J.L. Hodeau, V. Favre-Nicolin, S. Bos, H. Renevier, E. Lorenzo, J.F. Berar, Chem Rev, 101 (2001) 1843-1867.
[14] J. Als-Nielsen, Elements of Modern X-Ray Physics, Wiley, New York, (2001).
[15] D. Totir, Y. Mo, S. Kim, M.R. Antonio, D.A. Schersona, J Electrochem Soc, 147 (2000) 4594-4597.
[16] E. Fujita, L.R. Furenlid, M.W. Renner, J Am Chem Soc, 119 (1997) 4549-4550.
[17] A.R. Sandy, S.G.J. Mochrie, D.M. Zehner, K.G. Huang, D. Gibbs, Phys Rev B, 43 (1991) 4667-4687.
[18] G.S. Cao, X.J. Zhang, L. Su, B Mater Sci, 34 (2011) 973-977.

Chapter 8:

Conclusions

For the work contained within this thesis electrochemical methods have been used to form and study supported metal multilayers. Techniques including SXS, STM and AFM have been used to characterise the structural and chemical properties of Ag and Co monolayer(s) on Au(111) electrode. The nature of the new surface results in different ordering and properties of the surface Au atoms, deposited metal atoms and electrochemical double layer. To fully analyse the CTR data, measured at fixed potentials, parameters for the electrochemical double layer were included in the models. Understanding the double layer structure is useful to the development of fundamental electrochemistry. It has been shown that by forming supported metal multilayers, the properties of the new surface are different from the clean surface and this leads to enhancement for certain reactions, such as the HER for Co modified Au(111) described in Chapter 7, or of other material properties such as PMA as shown in Chapter 6.

In Chapter 5 the structure and electrochemical behaviour of UPD Ag monolayer and bilayer on Au(111) was studied using SXS and CV. On transfer to 0.1 M KOH the Ag bilayer on Au(111) is stable, conversely the Ag monolayer re-orders to a partial bilayer structure. This is due to the replacement of adsorbed sulphate anions,

which stabilise the monolayer, with OH^-. The CV for the Ag-modified Au(111) electrode shows OH^- adsorption behaviour similar to that of Ag single crystals with the bilayer behaving as Ag(111). The potential for OH^- adsorption for the partial bilayer suggests that Ag (100) and (110) steps are present. Detailed modelling of the CTRs required an OH^- layer in the electrolyte side of the interface. The coverage of the OH^- layer was found to be 0.45 ML for the complete bilayer and 0.2 ML for the partial bilayer. The presence of subsurface OH was indicated in the CV and the CTR measurements. The work contained within this Chapter is in being prepared for publication.

In Chapter 6 the motivation for studying Co thin films electrodeposited onto Au(111) was to link the atomic structure in the Co thin films electrodeposited onto Au(111) with the magnetic properties, particularly with relation to the CO-induced change in magnetization in films which are thicker than one Co monolayer. SXS results show that the in-plane strain for a 2 ML thick Co film is ~2.5% ($a = 2.572$ Å) compared to bulk Co ($a = 2.51$ Å). Detailed characterization of the thin film structure, performed by analysis of the specular CTR which probes the surface normal structure across the Au(111) electrolyte interface, revealed a small outward expansion in the Co film by ~2% of the Au(111) lattice spacing which may be caused by the presence of adsorbed hydrogen on the Co surface. Following CO adsorption on the Co films the SXS results indicate that there are only very small changes in the atomic structure at the surface of the Co film. In particular the adsorption of CO has no effect at all on the in-plane lattice strain of the Co film, which is entirely due to the lattice mismatch with the underlying Au substrate. There is some evidence that there is a slight reduction in the outward expansion of the surface Co layer and this may be due to the partial replacement of adsorbed hydrogen with CO. No potential dependence was found at any position where the scattering was uniquely due to the Co film. The measurements certainly indicate that the changes in the magnetic behaviour are driven by a surface process associated with the surface

charge and not by any structural rearrangement in the Co film. The work contained within this Chapter is in being prepared for publication.

In Chapter 7 thin films of Co were deposited on an Au(111) electrode prior to transfer of the electrode to 0.1 M KOH. Ex-situ AFM imaging revealed that, after transfer to alkaline electrolyte, Co is present in the form of large islands which are located at the step edges of the Au(111) surface. These islands cover approximately 2.2% of the Au surface and contain Co in 2 different charge states. Fluorescence measurements indicate the presence of Co in a charged state, which is most likely $Co(OH)_2$, and also shows evidence of a small amount of metallic Co. Qualitative analysis of resonant SXS measurements confirms the presence of Co in different charge states. It is proposed that within the $Co(OH)_2$ islands there is ordered metallic Co. The presence of the $Co(OH)_2$ islands affects the underlying Au surface structure resulting in a modified reconstruction, different to the Au(111) (23 x √3) reconstruction. The modified reconstruction was also present for a partially dissolved Co bilayer on the Au(111) surface in acid electrolyte. The results imply that the reconstruction consists of a compressed hexagonal Au structure induced by the presence of Co islands and/or partial coverage of Co on the Au(111) surface. It is suggested that the modified reconstruction occurs because the Au(111) surface compensates for the lattice mismatch by undergoing a compression and that, upon removal of the deposited Co layers, the remaining Co islands pins into place. Remarkably, although Co only covers ~2.2% of the Au(111) surface, its presence lowers the overpotential for the HER. CV measurements revealed that the potential for hydrogen evolution is shifted positively by ~0.1 V on the Co island-modified surface compared to clean Au(111). It is therefore feasible that mixed Au/Co sites on the Au(111) surface, formed due to the repeated deposition/stripping of Co on the Au(111) surface prior to transferring the electrode to the alkaline electrolyte, are responsible for the enhancement of the HER.

In-situ SXS has been shown to be a very useful technique, as it gives structural information under realistic conditions and from resonant SXS chemical information

can be obtained too. The first stage for future work involving the supported metal multilayers studied within this Thesis would be, to fully categorise the catalytic properties of the surfaces. Next the stability of the supported metal multilayers as catalysts should be tested. If these experiments prove fruitful, development of nanoparticles based on these materials would be useful, such as core-shell nanoparticles, as they can allow mass production of high quality well defined surface structures. Finally experiments in realistic catalytic conditions such as fuel cells should be performed. Another avenue for future work is further development of the experiments in Chapter 5 in order to study the silver oxide surface. There are still countless supported metal multilayer systems to be studied and understood. Batch testing of new materials already occurs but understanding the properties at the atomic scale can be very instructive in the targeted development of new materials and as such in-situ SXS combined with imaging techniques such as STM provide the perfect tools to explore these properties. Parallel to the direct development of these new surfaces, advancements to fundamental knowledge, such as fully understanding the structure of the electrochemical double layer, are still to be made.

Publications

- The Structure and Stability of Ag on Au(111) in Alkaline Electrolyte

  N. Sisson, D. Hesp, E. Hynes, M. Darlington, P. Thompson, Y. Gründer and C. A. Lucas

  (To be submitted)

- Growth, Structure and Magnetism of Thin Cobalt Films Electrodeposited onto Au(111)

  N. Sisson, F. Maroun, P. Allongue, R. Cortès, P. Thompson, and C. A. Lucas

  (To be submitted)

- Electroreduction of oxygen on gold-supported nanostructured palladium films in acid solutions

  A. Sarapuu, A. Kasikov, N. Wong, C. A. Lucas, G. Sedghi, R. J. Nichols, K. Tammeveski

  Electrochimica Acta, 55 (2010) 6768-6774

- NO adsorption on Pt (111)/Bi surfaces

  M. C. Figueiredo, N. Sisson, R. J. Nichols, C. A. Lucas, V. Climent, J. M. Feliu

  Electrochemistry Communications, 34 (2013) 37-40

- The Relationship between Atomic Structure and Enhanced Activity in Gold Electrocatalysis

  G. Harlow, Y. Gründer, N. Sisson, P. Thompson, E. Cocklin and C. A. Lucas

  (To be submitted)

Presentations

- 13th International Conference on Electrified Interfaces (2013)
  Poster Presentation
  The Structure and Stability of Ag on Au(111) in Alkaline Electrolyte

  N. Sisson, D. Hesp, E. Hynes, M. Darlington, P. Thompson, Y. Gründer and C. A. Lucas

- 28th European Conference on Surface Science (2011)
  Oral Presentation
  In Situ X-ray Scattering Studies of the Atomic Structure at the Electrochemical Interface

  N. Sisson, D. Hesp, E. Hynes, M. Darlington, A. Brownrigg, P. Thompson, Y. Gründer and C. A. Lucas